Time-resolved spectroscopy of quantum dot single-photon sources

Lund-Hansen, Toke

Publication date:
2009

Document Version
Publisher's PDF, also known as Version of record

Time-Resolved Spectroscopy of Quantum Dot Single-Photon Sources

Toke Lund-Hansen

Ph.D. Thesis
May 2009

DTU Fotonik
Technical University of Denmark
Kgs Lyngby, Denmark

Abstract

This thesis investigates efficient single-photon sources based on quantum dots using time-resolved photoluminescence spectroscopy.

First micropillar cavities with quantum dots are investigated by measurements of the spectra and decay rates of the quantum dots as a function of detuning to the cavity mode. An enhancement of the decay rate of 10 is seen when tuning a quantum dot into resonance with the cavity mode. To understand these data a model of the interaction of a quantum dot to the electromagnetic field of the cavity is derived where dephasing of the emitter is included. The model is used to interpret the measurements and a consistent understanding of the interaction is achieved and limits on the dephasing rate are extracted.

The single-photon emission properties of the micropillar cavities are then investigated by measuring the single-photon statistics and a multi-photon contribution of only 13% is found. This residual emission is investigated for various detunings and pump powers. The photon indistinguishability is also measured as a function of the detuning and a degree of indistinguishability of 61% on resonance is measured. These data are compared to the model and the comparison of the theoretical model with the complete set of data from measurements of the spectra, decay rates, single-photon emission, and indistinguishability gives for the first time a consistent picture of the interaction and single-photon emission of quantum dots in micropillar cavities.

Then a photonic crystal waveguide with embedded quantum dots are examined. These are promising nanostructures for an efficient single-photon

source due to the slow down of light in the waveguide facilitating an efficient coupling of the quantum dots directly to the propagating mode of the waveguide. This coupling of quantum dots to the photonic crystal waveguide is experimentally demonstrated for the first time. The coupling is found to be very efficient with a β factor of up to 0.89 and even more intriguing the coupling is seen to be broadband with a bandwidth of 2% corresponding to 20 nm, which is large compared to single-photon sources based on cavities. The frequency dependence of the coupling is calculated and found to be in excellent agrement with the measured frequency dependence.

Resumé

Tidsopløst spektroskopi af kvantepunktsbaserede enkelt-foton-kilder

I denne afhandling undersøges effektive enkelt-foton-kilder baseret på kvantepunkter ved brug af tidsopløst spektroskopi.

Først undersøges en mikrosøjlekavitet med indlejrede kvantepunkter ved at måle fotoluminescensspektre og henfaldsrater af kvantepunkterne som en funktion af forskellen imellem kvantepunktet og kavitetens resonansbølgelængder. En forstærkning af henfaldsraten med en faktor 10 observeres, når kvantepunktet er på resonans med kaviteten. En model for koblingen mellem kaviteten og kvantepunktet, hvor dephasing er medtaget, er udviklet og modellen giver en konsistent forståelse af målinger og en øvre grænse for dephasingraterne udledes.

Dernæst er enkelt-foton egenskaberne af mikrosøjlekaviteterne undersøgt ved at måle enkelt-foton statistikken af det udsendte lys og et multi-foton bidrag på 13% er målt. Dette multi-foton bidrag er undersøgt for forskellige intensiteter af pumpelyset og emissionsbølgelængder af kvantepunktet. Uadskilleligheden af de udsendte fotonerne er målt med en maksimal uadskilleligheds grad på 61%, når kvantepunktet er på resonans med kaviteten. Disse målinger sammenlignes med modellen og en konsistent forståelse af koblingen mellem et kvantepunkt og en mikrosøjlekavitet for både spektre, henfaldsrater, enkelt-foton statistik og uadskilleligheden af fotonerne opnås for første gang.

En anden enkelt-foton-kilde baseret på kvantepunkter i en fotonisk krystal-bølgeleder bliver også undersøgt. Disse er lovende enkelt-foton-kilder på grund af den langsomme udbredelse af lys i bølgelederen som medfører en effektiv kobling af kvantepunktet til lyset i bølgelederen. Koblingen af kvantepunkter til en fotonisk krystal-bølgeleder bliver eksperimentelt demonstreret for første gang og en effektiv kobling på op til 89% er målt. Desuden udregnes frekvensafhængigheden af koblingen og findes i god overensstemmelse med de målte data. Endnu mere interessant er det at båndbredden af koblingen er 2%, hvilket svarer til 20 nm og er meget bredere end for enkelt-foton-kilder baseret på kaviteter.

Preface

The research presented in this thesis has been carried out in the Quantum Photonics Group, DTU Fotonik at the Technical University of Denmark from February 2006 to February 2009 while I was enrolled as a ph.d. student. The work has been carried out under the supervision of associate professor Peter Lodahl and professor Jørn M. Hvam.

First of all I would like to thank my main supervisor Peter Lodahl for guidance and directing my research in interesting directions. I would also like to thank Jørn Hvam for creating a group with unique and broad set of competences in fabrication, optics and theory that has been crucial for doing the research presented here.

A lot of people has contributed to the work presented here. First of all nothing would have been possible without the samples which have been supplied by collaborators both in-house and externally. I would like to thank Søren Stobbe for the good collaboration especially on the waveguide samples where he was in charge of the fabrication. I would also like to thank Stephan Reitzenstein from the University of Würburg for supplying micropillar cavities.

I am also grateful to Jeppe Johansen for introduced me to the laboratory and Brian Julsgaard for a lot of help and teaching me many tricks in the laboratory. Furthermore I would like to thank Henri Nielsen for help in the laboratory, Lars Frandsen for help with the simulations of the photonic crystal waveguides and Niels Gregersen for calculations and discussion about the micropillar cavities.

A special thank goes to Jeppe and the people in the office: Søren, Mads

and Per for good discussions and fun, making my time at DTU Fotonik enjoyable even when nothing works in the laboratory. I would also like to thank the rest of the people in the nanophotonics cluster and especially Philip, Stephan, Henri and Martin for making it a pleasant place to be.

Finally I would like to thank my family and friends for support and especially Stine, Uffe, Annette, Torben and Solveig.

Publications

The following publications have been authored or coauthored during the course of the Ph.d. project:

Journal publications

- T. Lund-Hansen, S. Stobbe, B. Julsgaard, H. Thyrrestrup, T. Sünner, M. Kamp, A. Forchel og P. Lodahl, Experimental realization of highly-efficient broadband coupling of single quantum dots to a photonic crystal waveguide. Physical Review Letters 101, 113903 (2008)

- J. Johansen, S. Stobbe, I. Nikolaev, T. Lund-Hansen, P. T. Kristensen, J. M. Hvam, W. L. Vos og P. Lodahl, Size dependence of the wavefunction of self-assembled InAs quantum dots from time-resolved optical measurements. Physical Review B 77, 073303 (2007)

Conference proceedings

- T. Lund-Hansen, S. Stobbe, B. Julsgaard, T. Sünner, M. Kamp, A. Forchel og P. Lodahl, Efficient radiative coupling of single quantum dots to a photonic crystal waveguide. CLEO/QELS, San Jose, CA, USA, 2008

- T. Lund-Hansen, S. Stobbe, B. Julsgaard, P. Lodahl, Coupling of single quantum dots to a photonic crystal waveguide. Annual meeting of the Danish Physical Society, Nyborg, Denmark, 2008

- T. Lund-Hansen, J. Johansen, S. Stobbe, J. M. Hvam, P. Lodahl, Detailed investigation of spontaneous emission decay rates of self-assembled InAs quantum dots. European Conference on Integrated Optics. Lyngby, Denmark, 2007

- T. Lund-Hansen, J. Johansen, S. Stobbe, J. M. Hvam, P. Lodahl, Measuring dipole moment and quantum efficiency of self-assembled InAs/GaAs quantum dots using a modified electromagnetic vacuum. Dansk Fysisk Selskabs Årsmøde. Nyborg, Denmark, 2007

- T. Lund-Hansen, J. Johansen, J. M. Hvam, P. Lodahl, T. van Lippen, R. Nötzel, Time- and energy-resolved measurements of spontaneous emission from ordered quantum dots. 1st European Topical Meeting on Nanophotonics and Metamaterials. Seefeld, Tirol. Austria, 2007

- J. Johansen, S. Stobbe, I. S. Nikolaev, T. Lund-Hansen, P. T. Kristensen, J. M. Hvam, W. L. Vos og P. Lodahl, Quantum efficiency of self-assembled quantum dots determined by a modified optical local density of states. CLEO/QELS, Baltimore, USA, 2007

- H. Thyrrestrup, T. Lund-Hansen, B. Julsgaard og P. Lodahl, Dynamic and spontaneous emission from quantum dots coupled to a photonic crystal nano-cavity. Annual meeting of the Danish Physical Society, Nyborg, Denmark, 2007

- S. Stobbe, J. Johansen, I. S. Nikolaev, T. Lund-Hansen, P. T. Kristensen, J. M. Hvam, W. L. Vos og P. Lodahl, Accurate measurement of the transition dipole moment of self-assembled quantum dots. CLEO/Europe-IQEC. Munich, Germany, 2007

- J. Johansen, T. Lund-Hansen, J. M. Hvam, P. Lodahl, Highly Efficient Spontaneous Emission from Self-Assembled Quantum Dots, Proc. EOS Topical Meeting on Nanophotonics, Metamaterials and Optical Microcavities. Paris, France, 2006

Contents

1 Introduction **1**

2 Quantum dot single-photon sources **5**
2.1 Self-assembled InAs quantum dots as single-photon emitters 6
2.1.1 Energy states and excitons in quantum dots 6
2.1.2 Formation of self-assembled quantum dots 8
2.1.3 Optical properties 8
2.2 Interaction of quantum dots with light 11
2.2.1 Spontaneous emission 13
2.2.2 Photonic crystals 18
2.2.3 β-factors 19
2.3 Spontaneous emission of a quantum dot in a high-Q cavity . 20
2.3.1 Decay dynamics with the inclusion of dephasing . . . 28
2.3.2 Emission spectra 31
2.4 Single-photon statistics and the Hanbury-Brown and Twiss experiment 34
2.4.1 Second order coherence measurements with a background contribution 37
2.5 Photon indistinguishability 38
2.5.1 Dephasing 40

3 Experimental setup for time-resolved photoluminescence of single quantum dots **43**

3.1 Cryostat and sample mounting 44
3.2 Excitation 45
3.3 Microscope 46
3.3.1 Microscope objectives 47
3.3.2 Coupling efficiency of the fiber 49
3.3.3 Low angle excitation 50
3.4 Detection 50
3.4.1 Time correlated single-photon counting 53
3.4.2 Hanbury-Brown and Twiss setup 54
3.4.3 Hong-Ou-Mandel interferometer 54

4 Coupling of quantum dots to micropillar cavities 57
4.1 Micropillar cavities 58
4.2 Samples 60
4.2.1 Choosing a pillar diameter 62
4.3 Photoluminescence measurements 63
4.3.1 Temperature tuning 65
4.3.2 Measuring cavity Q factors 67
4.3.3 Photoluminescence excitation spectroscopy and excited state excitation 68
4.3.4 Excitation intensity 72
4.3.5 Photoluminescence spectra of a quantum dot tuned to the cavity mode 74
4.4 Time-resolved measurements 78
4.4.1 Detuning dependence of the decay rate 80
4.4.2 Comparison between measured and calculated spectra 86
4.4.3 β-factor 89
4.5 Time-resolved measurements with non-resonant pumping . . 89
4.6 Conclusion 92

5 Single-photon emission from quantum dots in micropillar cavities 95
5.1 Single-photon emission 95
5.1.1 Hanbury-Brown and Twiss measurements 97

5.1.2 Power dependence on the single photon emission . . 100
5.1.3 Influence of detuning on the single-photon emission . 102
5.2 Photon indistinguishability and Hong-Ou-Mandel interferometry 104
5.2.1 Photon indistinguishability measurements 108
5.2.2 Temperature and detuning dependence on the photon indistinguishability 114
5.3 Conclusion 116

6 Coupling of single quantum dots to a photonic crystal waveguide 119
6.1 Photonic crystal waveguide samples 120
6.2 Calculating the waveguide modes 121
6.3 Demonstration of coupling of quantum dots to a photonic crystal waveguide 124
6.3.1 Photoluminescence spectra 126
6.3.2 Time-resolved measurements 129
6.3.3 Decay rate as a function of emission frequency . . . 131
6.3.4 Coupling efficiency 135
6.4 Conclusion and outlook 139

7 Conclusion 141

Chapter 1

Introduction

Development of an efficient single-photon source is of fundamental interest due to the quantum nature of the emitted single-photon state as it provides functionalities not available with classical light. A highly efficient single-photon source is the key component required in many quantum communication protocols [1] and will allow implementing linear optics quantum computing [2]. One of the first application of single-photon sources is quantum key distribution, which enables two parties to securely share a random key which can then be used for encryption [3]. Quantum key distribution can also be implemented with attenuated laser pulses but single-photon sources will significantly improve the performance [4]. In general efficient and high quality single-photon sources will provide access to a new quantum light source which is fundamentally different from classical sources and might find applications in other research areas such as metrology [5] and fields yet to be identified.

This thesis investigates single-photon sources based on quantum dots in nanophotonic structures. Quantum dots have gained a lot of attention as solid-state single-photon sources and have been demonstrated to be good single-photon emitters [6, 7, 8]. As the quantum dots are solid-state single-photon sources they have several advantages compared to sources based on atoms or parametric down conversion: The position of the emitter is

fixed and it therefore emits into the same modes for every excitation. They can also be integrated with semiconductor nanofabrication technology to integrate them with devices such as nanocavities and waveguides which are investigated here and the technology is scalable such that a large number of sources can be fabricated and integrated. The stability of the source is also good and the efficiency can be very high [9].

To enhance the single-photon emission efficiency of quantum dots they can be embedded in nanophotonic structures with an enhanced optical mode to which the emission can be efficiently coupled. One successful approach has been to use different types of micro- and nanocavities [10, 11, 12, 13]. A single-photon source based on a quantum dot in a micropillar cavity is investigated in this thesis. Another approach is to couple quantum dots to a photonic crystal waveguide, which is favorable since the photon is emitted to a propagating mode and therefore can be employed directly. The first experimental demonstration of the efficient coupling of a single quantum dot to a photonic crystal waveguide is presented here.

One of the central parts of this thesis is to understand the possibilities and limitations of quantum dot single-photon sources and especially the coupling of quantum dots to the optical modes of photonic nanostructures. In chapter 2 the theory of the light-matter interaction of quantum dots are investigated and a model for the interaction in high-Q cavities is derived. A major challenge with solid-state photon sources is the strong interaction with the environment resulting in large dephasing rates compared to e.g. atoms in dilute gasses. To understand the influence of dephasing on the coupling it is included in the model derived in chapter 2.

The main experimental method used in this thesis is time-resolved photoluminescence spectroscopy and a setup to do these measurements has been established and is described in chapter 3. It can also be used to measure the single-photon statistics using a Hanbury-Brown Twiss setup and includes a Hong-Ou-Mandel interferometer for measuring the indistinguishability of the emitted photons. The setup facilitates easy switching between the different types of measurements making it possible to extract different aspects of the photon emission of a single-photon source.

The coupling of of quantum dots to micropillar cavities has been mea-

sured in chapter 4 and the results are compared to the theory developed in chapter 2. The emission spectra and decay rate of a quantum dot coupled to the cavity mode are measured and the theoretical model is used to extract relevant parameters of the coupling, including dephasing. The micropillar cavities are further investigated in chapter 5 where the single-photon emission properties are investigated by measuring the suppression of multi-photon emission and the indistinguishability of the emitted photons. These are measured for different values of the detuning to the micropillar and the results are interpreted using the theory of chapter 2. In this way a consistent understanding of the interactions of the quantum dot with the micropillar cavity is obtained.

Recent proposals show that a very efficient single-photon source can be realized by using photonic crystal waveguides [14, 15, 16, 17]. In these structures the emission is enhanced into the waveguide due to the slow down of light in the waveguide. This is investigated in chapter 6 where it is experimentally demonstrated that single quantum dots can be efficiently coupled to a photonic crystal waveguide.

Chapter 2

Quantum dot single-photon sources

The most important and defining property of a single-photon source is that for each trigger of the source one and only one photon is emitted. This is very different from e.g. laser sources where the photon number distribution is Poissonian. Single-photon emission may be achieved by using the emission from a quantum system with discrete energy levels as the energy levels cannot be reexcited before it has decayed due to the Pauli exclusion principle. The requirement of the emission of a photon for every excitation can in some applications such as quantum key distribution be relaxed to allow zero or one photon being emitted per excitation [4].

The other important property is that the emitted photons should be in a specific quantum state. This means that the emission frequency should be well defined and the spatial mode and the polarization of emitted light should be controlled. This is especially important for applications in quantum information processing such as linear quantum computing [2], where all of the photons used should be indistinguishable. This means that the photons should have the same wavelength and polarization but also that the optical phase should not change. Interactions of the emitter with the environment can result in changes of the emission wavelength of the emitter

while decaying and thereby the phase. This will result in distinguishable photons being emitted. For this reason the interactions with the environment of the single photon emitter should be limited to timescales longer than the decay time.

Single photons can be efficiently harvested when the emitter is coupled efficiently to an enhanced optical mode. This can be achieved by embedding the quantum dots in nanophotonic structures. One successful approach has been to use nanocavities [10, 11, 12, 13]. Another approach is to couple the quantum dots to a waveguide where the confinement is only in two dimensions. This new approach is investigated in chapter 6. A similar approach using a nanowire has also been demonstrated very recently [18].

To understand the single-photon sources the basic understanding of the single-photon emitters and the interaction of these with light in the nanostructures are needed. In this chapter the quantum dots used as single-photon emitters will be described first and the optical properties presented. The basic theory of the interaction of quantum dots with light in nanophotonic structures will then be discussed. At the end the theory of measuring the single-photon statistics and the photon indistinguishability is presented.

2.1 Self-assembled InAs quantum dots as single-photon emitters

The single-photon emitters used in this thesis are self-assembled InAs quantum dots. These are nanoscale clusters of InAs embedded in a host material of GaAs. Such quantum dots have been used to demonstrate excellent single-photon emission [6, 7] including the emission of highly indistinguishable photons [8].

2.1.1 Energy states and excitons in quantum dots

InAs and GaAs are direct bandgap semiconductors which means that the minimum of the conduction band is coinciding with the maximum of the valence band at $\boldsymbol{k} = 0$. At this point in reciprocal space the conduction

band can be approximated by a parabolic potential and electrons occupying energy states in the bottom of the conduction band can be described as free particles with an effective mass. When an electron is excited into the conduction band it leaves a hole in the valence band which can be seen as a positively charged particle with a different effective mass due to the difference in the conduction band and valence band curvatures. As the photon momentum is much smaller than the momentum of the electron the direct bandgap also makes the semiconductor optically active as momentum conservation is fulfilled when the electron and hole recombines by emitting a photon.

The bandgap of InAs is smaller than GaAs which results in a confining potential for electrons and holes in the quantum dot. Due to the small size of the quantum dot this confinement results in discrete quantized energy states of the electron and holes. This means that direct bandgap semiconductor quantum dots have discrete optically active states which is exactly what is needed for a single-photon source. The bound state of an electron and hole to a quantum dot is called an exciton (X) which can decay by emitting a single photon.

Depending on the size of the quantum dots they will have a ground state and one or more excited states. The excited states of a quantum dot are also sometimes, in analogy with atomic physics, called the p-shell, d-shell and so on. The excited states are not seen in the emission for low excitations of a quantum dot as the excitons in the excited states decays to the ground state much faster than the radiative decay rate of the states. However, if the ground state is filled excitons can decay from the excited states. The decay of the ground state exciton is between the conduction band with an angular momentum $J = 1/2$ and the heavy hole band with $J = 3/2$ both with a degeneracy of two due to the electron spin. The total angular momentum of the exciton can then be either ± 1 or ± 2. As the angular momentum of photons are ± 1 only excitons with this angular momentum can decay radiatively. These corresponds to the electron and hole having opposite spins and are called bright excitons while excitons where the spins are the same are called dark excitons and will only decay non-radiatively or through a spin flip to a bright state [19]. If both spins states are occupied

this is called a biexciton (X_2) which has an energy shift of a few meV due to the interaction of the two excitons [20].

In this thesis the focus will primarily be on the ground state exciton which for most purposes can be regarded as a two-level system where the ground state is the unoccupied quantum dot and the excited state is the ground state exciton.

2.1.2 Formation of self-assembled quantum dots

The quantum dots are formed by strain-induced self-assembly. This is done by depositing InAs on a surface of GaAs. InAs has a larger lattice constant than GaAs and when InAs is deposited on the GaAs surface the strain will increase as the layer of InAs increases. At some point the induced strain will favor the formation of small islands of InAs which then forms the quantum dots. The result is quantum dots randomly distributed on the surface on top of a thin quantum well which is called the wetting layer. An atomic force micrograph of InAs quantum dots is shown in the left part of figure 2.1. This clearly shows the random nature of the quantum dot growth. To make the quantum dots optically active they must be completely embedded in GaAs by capping them with a with a layer of GaAs.

Depending on the temperature, deposition rate, interrupt in the growth etc. the size and density of the quantum dots can be engineered. In the growth direction the position of the quantum dots are controlled very precisely down to a few lattice constants. Due to the random nature of the formation the position in the other two dimensions is random. However, recently significant developments has been done to control the position perpendicular to the growth direction [21, 22].

2.1.3 Optical properties

A simplified picture of the energy states of a quantum dot as a function of the growth direction is shown in the right part of figure 2.1. The figure illustrates the confinement potential of a quantum dot giving rise to the discrete energy states. The wetting layer below the quantum dot is also

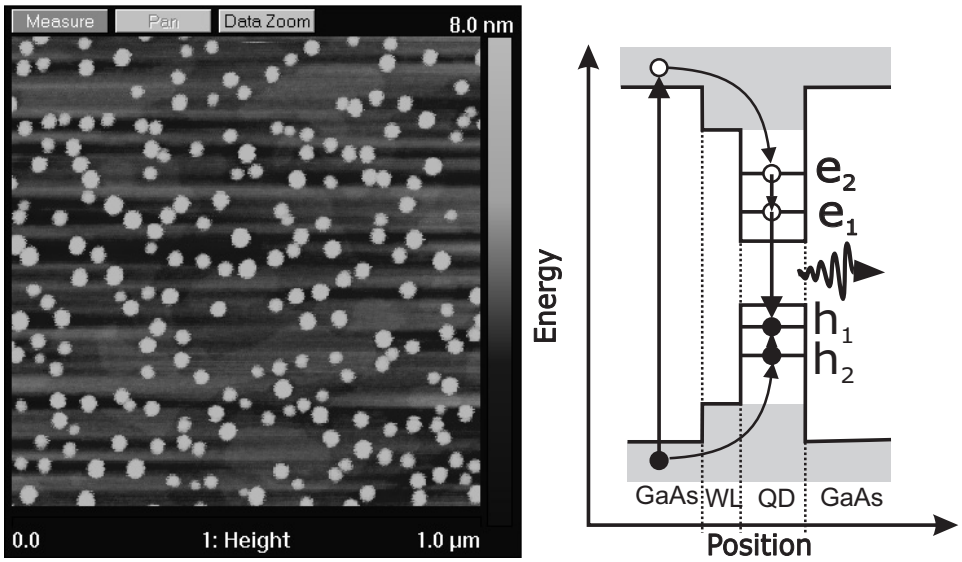

Figure 2.1: Left: Atomic force microscopy image of InAs quantum dots. Right: A simplified band diagram of a quantum dot in the growth direction. The position of the bulk GaAs, the wetting layer (WL) and the quantum dot (QD) is marked at the position axis. The grey area in the continuum of states above the GaAs bandgap and in the wetting layer. The arrows shows the process of the excitation of the quantum dot above the GaAs bandgap and the relaxation of the electron and hole into the quantum dot ground state to form an exciton which decays by emitting a single photon.

illustrated and the continuum of states in the wetting layer and the bulk GaAs surrounding the quantum dot is shown by the grey area. The figure illustrates the process of of excitation of the quantum dot with an energy above the GaAs bandgap. This creates an electron-hole pair which then relaxes into the ground state mediated by phonons. Excitation above the GaAs is very efficient as the electronic density of states is high and there is a lot of material to absorb the light. However excitation in the wetting layer or in the excited states can be favorable for single photon sources as will be shown in chapter 4. The ground state exciton then decays with a typical decay rate of 1 ns^{-1} by emitting a photon or with a small probability by a non-radiative decay [23].

The ground state emission wavelength of InAs quantum dots in GaAs is typically between 900 nm and 1300 nm depending on the size and the amount of Ga in the quantum dot and by controlling these parameters the emission wavelength can be engineered. However, the random nature of the formation also results in a distribution of quantum dot sizes and thereby the emission wavelength with the result that the emission of an ensemble of quantum dots is inhomogenously broadened. Depending on the growth conditions this can be between 1% and 10% of the emission wavelength.

An advantage of quantum dots compared to atoms is the large dipole moment of the ground state exciton. Typical measured values are $10 \cdot 10^{29}$ Cm [24, 23] which is an order of magnitude larger than for atomic transitions. This gives a higher coupling to the electromagnetic field which is important for generating efficient single-photon sources as will be discussed below.

Dephasing rates of quantum dots

One of the major challenges of using quantum dots as single-photon sources is the strong interaction with the environment. For this reason experiments are done at low temperatures.

The interaction results in small changes of the energy levels of the quantum dot which gives a dephasing of the exciton and thereby the emitted photon. For low temperatures (< 60 K) the dephasing rate has been found to depend linearly on the temperature due to scattering with acoustic phonons

while at higher temperatures the optical phonons start to contribute. From four-wave mixing experiments a linear dependence of the dephasing rate of 0.22 ± 0.02 μeV/K has been found [25] and from measurements of the linewidth of single quantum dots a linear dependence from 0.05 μeV/K to 2 μeV/K has been found [26, 27, 28]. These measurements are done with p-shell excitation. Using an excitation energy above the GaAs bandgap a larger value of at least 15 μeV at 2 K is found [26].

Collection efficiency of single-photons from quantum dots in bulk material

To motivate the use of nanophotonic structures for single-photon sources the collection efficiency of the emission from quantum dots in a bulk sample is calculated.

For a uniform angular distribution of the emission the light collected by a lens with a numerical aperture of NA is given by $\mathrm{NA}^2/4$. Due to the refraction on the surface of the sample the effective numerical aperture is reduced to $\mathrm{NA}' = \mathrm{NA}/n$. Using the refractive index (n) of GaAs of 3.5 and a large NA of 0.8 the collection efficiency is given by 1.4%.The large refractive index of the GaAs also results in a large reflection from the surface. For light exiting the sample perpendicular to the surface the transmission is 69%. This shows that using semiconductor quantum dots in bulk material as single-photon sources are very inefficient as reaching a collection efficiency higher than 1% is difficult and shows that a different strategy is needed to design an efficient single-photon source.

2.2 Interaction of quantum dots with light

The central part of designing and understanding single-photon sources and other nanophotonic structures is to understand the basic interaction of the quantum dot with the electromagnetic field. The quantum dots investigated in this work are very similar, however the nanostructures are fundamentally different and offer different advantages and disadvantages. To compare the different structures and interpret the measured characteristics of the structures this section describes the interaction of light with quantum dots in

the different regimes and structures explored in this thesis.

The quantum dots will be described as a two-level system with the ground state exciton (X) as the excited state ($|e\rangle$) and the non-excited state as the ground state ($|g\rangle$). The interaction is given by the transition operators $\hat{\sigma}_+ = |e\rangle\langle g|$ and $\hat{\sigma}_- = |g\rangle\langle e|$. In general the energy states of the quantum dots are more complicated as described in section 2.1. However, for the bright ground state of the quantum dots used in this work this is a good approximation as it is a discrete energy state well-separated from the excited states of the quantum dot.

The electric field of a single mode in the Schrödinger picture is described in terms of the creation ($\hat{a}^\dagger$) and annihilation ($\hat{a}$) operators of the field:

$$\hat{\boldsymbol{E}}(t)(\boldsymbol{r},t) = iE_0\left(\boldsymbol{f}(\boldsymbol{r})\hat{a}(t) - \boldsymbol{f}^*(\boldsymbol{r})\hat{a}^\dagger(t)\right), \tag{2.1}$$

where $\boldsymbol{f}$ is the relative field amplitude and polarization. This can also be written explicitly in terms of the polarization ($\boldsymbol{\epsilon}(\boldsymbol{r})$) and amplitude ($f(\boldsymbol{r})$) as $\boldsymbol{f}(\boldsymbol{r}) = \boldsymbol{\epsilon}(\boldsymbol{r})f(\boldsymbol{r})$. The normalized field amplitude $f(\boldsymbol{r})$ is normalized to unity at the maximum field amplitude ($|f|_{\max} = 1$). An example is a plane wave where $f(\boldsymbol{r}) \sim e^{i\boldsymbol{k}\cdot\boldsymbol{r}}$.

The normalization parameter (E_0) can be found from the energy of the electric field with N photons:

$$\begin{aligned}
\hbar\omega(N+\tfrac{1}{2}) &= \langle N|\int n(\boldsymbol{r})^2\epsilon_0|\boldsymbol{E}|^2 d^3\boldsymbol{r}|N\rangle \\
&= \epsilon_0 n^2 E_0^2 V(2N+1),\ V = \frac{1}{n^2}\int n(\boldsymbol{r})^2|\boldsymbol{f}(\boldsymbol{r})|^2 d\boldsymbol{r} \quad (2.2)\\
\Rightarrow E_0 &= \sqrt{\hbar\omega/2n^2\epsilon_0 V}, \quad (2.3)
\end{aligned}$$

where n is the refractive index of the material and V is the effective mode volume. This is an important parameter for confined fields such as in cavities where it describes how efficiently the mode is confined as will be described below.

The unperturbed Hamiltonian for the two-level atom and the electro-

magnetic field is given by

$$H_0 = \sum_{\boldsymbol{k}} \hbar\omega_k \hat{a}^\dagger_{\boldsymbol{k}} \hat{a}_{\boldsymbol{k}} + \hbar\omega_0 \hat{\sigma}_+ \hat{\sigma}_-, \tag{2.4}$$

where the zero photon state has been offet to an energy of 0, ω_k is the frequency of the electromagnetic mode, and ω_0 is the transition frequency of the emitter. The interaction of the field with the two-level system in the dipole approximation ($\boldsymbol{k}\cdot\boldsymbol{r} \ll 1$) is given by $\hat{H}_1 = -\hat{\boldsymbol{d}}\cdot\hat{\boldsymbol{E}}$ [29], where $\hat{\boldsymbol{d}}$ is the dipole moment of the emitter and $\hat{\boldsymbol{E}}$ is the electric field. This approximation is valid for the quantum dots investigated here as the size of the dots are in general a factor of 10 smaller than the emission wavelength. For quantum dots with large dimension this may not be the case [30, 31].

Inserting the electric field from eq. 2.1, applying the rotating wave approximation, and moving to the interaction picture the resulting interaction Hamiltonian is

$$\hat{H}_I = -\sum_{\boldsymbol{k}} iE_{0,k}\boldsymbol{d}\cdot\left(\boldsymbol{f}_{\boldsymbol{k}}(\boldsymbol{r})\hat{\sigma}_+\hat{a}_{\boldsymbol{k}}e^{i\Delta_k t} - \boldsymbol{f}^*_{\boldsymbol{k}}(\boldsymbol{r})\hat{\sigma}_-\hat{a}^\dagger_{\boldsymbol{k}}e^{-i\Delta_k t}\right), \tag{2.5}$$

where $\Delta_k = \omega_0 - \omega_k$ is the detuning of the two-level transition to the mode. This is the general Hamiltonian used for calculating the interaction of a quantum dot with light.

2.2.1 Spontaneous emission

The interaction studied in this thesis is the spontaneous emission decay of quantum dots. To calculate the spontaneous emission the quantum dot will initially be in the excited state and then decay to the ground state emitting a photon in one of the available optical modes. The quantum state for the system can then be written as a superposition of the states involved in the process:

$$|\psi\rangle = c_e(t)|e,0\rangle + \sum_{\boldsymbol{k}} c_{g,\boldsymbol{k}}|g,1_{\boldsymbol{k}}\rangle, \tag{2.6}$$

where the sum is over all the available optical modes (including polarizations). This wavefunction can be inserted in the Schrödinger equation with

the interaction Hamiltonian (eq. 2.5) resulting in a set of equations of motion for the state

$$\dot{c}_e(t) = \frac{1}{\hbar}\sum_{\boldsymbol{k}} E_{0,\boldsymbol{k}}\boldsymbol{d}\cdot\boldsymbol{f_k}(\boldsymbol{r})e^{i\Delta_{\boldsymbol{k}}t}c_{g\boldsymbol{k}}(t) \tag{2.7}$$

$$\dot{c}_{g,\boldsymbol{k}}(t) = -\frac{1}{\hbar}E_{0,\boldsymbol{k}}\boldsymbol{d}\cdot f^*_{\boldsymbol{k}}(\boldsymbol{r})e^{-i\Delta_{\boldsymbol{k}}t}c_e(t). \tag{2.8}$$

To solve the equation for $c_e(t)$ the equation for $c_{g,\boldsymbol{k}}$ can be integrated and inserted in the equation for $c_e(t)$

$$\dot{c}_e(t) = -\frac{1}{\hbar^2}\sum_{\boldsymbol{k}} |E_{0,\boldsymbol{k}}\boldsymbol{d}\cdot\boldsymbol{f}(\boldsymbol{r})_{\boldsymbol{k}}|^2\int_0^t e^{-i\Delta(t-t')}c_e(t')dt' \tag{2.9}$$

By assuming that the modes of the field is closely spaced, the sum over $\boldsymbol{k}$ can be replaced by an integral over the density of optical states $\rho(\omega)$:

$$\dot{c}_e(t) = -\frac{1}{\hbar^2}\int_0^\infty E^2_{0,\omega}|\boldsymbol{d}\cdot\boldsymbol{f}(\boldsymbol{r})|^2\rho(\omega)d\omega\int_0^t e^{-i\Delta(t-t')}c_e(t')dt' \tag{2.10}$$

If it is further assumed that the optical density of states and the field varies little around ω_0, where the emission is centered the density of optical states and E_0 can be taken outside the integral.

$$\begin{aligned}
\dot{c}_e(t) &= -\frac{1}{\hbar^2}E^2_{0,\omega_0}\langle|\boldsymbol{d}\cdot f(\boldsymbol{r})|^2\rangle\rho(\omega_0)\int_{-\infty}^{\infty}d\omega\int_0^t e^{-i\Delta(t-t')}c_e(t')dt' \\
&= -\frac{1}{\hbar^2}E^2_{0,\omega_0}\langle|\boldsymbol{d}\cdot f(\boldsymbol{r})|^2\rangle\rho(\omega_0)\int_0^t \pi\delta(t-t')c_e(t')dt' \\
&= -\frac{1}{\hbar^2}E^2_{0,\omega_0}\langle|\boldsymbol{d}\cdot f(\boldsymbol{r})|^2\rangle\rho(\omega_0)\pi c_e(t) = -\frac{\Gamma}{2}c_e(t).
\end{aligned} \tag{2.11}$$

This is the Wigner-Weisskopf approximations and from the resulting equation (2.11) it can be seen that the dipole emitter decays exponentially with a rate

$$\Gamma = \frac{2\pi}{\hbar^2}E^2_{0,\omega_0}\langle|\boldsymbol{d}\cdot\boldsymbol{f}(\boldsymbol{r})|^2\rangle\rho(\omega_0). \tag{2.12}$$

This is a version of Fermi's golden rule for an electric dipole and can be used to calculate the decay rate of quantum dots in different photonic structures where the density of states is slowly varying. The only thing that needs to be calculated is then the density of states which will be done below for three examples of interest with different dimensionality: a homogenous medium (3 D), a cavity (0 D) and a waveguide (1 D).

Decay rate in a homogeneous medium

The simplest case is a homogenous medium where the density of states is given by

$$\rho(k)dk = \frac{k^2 V}{\pi^2}dk \Rightarrow \rho(\omega)d\omega = \frac{\omega^2 n^3}{\pi^2 c^3}Vd\omega. \tag{2.13}$$

As the optical frequency is large compared to the linewidth of the emitter the frequency varies slowly across the emitetr linewidth and the Wigner-Weisskopf approximation is accordingly very good. Inserting this expression in eq. 2.12 the decay rate is found:

$$\Gamma_0 = \frac{\omega^3 n|\boldsymbol{d}|^2}{3\pi\epsilon_0\hbar c^3}, \tag{2.14}$$

where the averaging of the field modes to the fixed orientation of the dipole gives a factor of 1/3. This expression is important as it is the reference for other structures when evaluating the achievable enhancement or inhibition of the spontaneous emission.

Decay rate in a cavity and the Purcell effect

In a cavity the field is confined in all dimensions and the field can therefore build up in the cavity resulting in a stronger coupling to an emitter inside. As a cavity is never perfect it will decay exponentially due to the losses with a rate κ. For a single mode cavity this results in an optical density of states given by a normalized Lorentzian distribution:

$$\rho_{cav}(\omega) = \frac{1}{\pi}\frac{\delta\omega/2}{(\omega_c - \omega)^2 + (\delta\omega/2)^2}, \tag{2.15}$$

where ω_c is the resonance frequency and $\delta\omega$ is the full width at half max (FWHM) of the resonance given by κ. The decay rate of the emitter is then given by

$$\Gamma_{cav} = \frac{2\pi}{\hbar^2} E_{0,\omega}^2 |\boldsymbol{d} \cdot \boldsymbol{f}(\boldsymbol{r})|^2 \frac{1}{\pi} \frac{\delta\omega/2}{(\omega_c - \omega)^2 + (\delta\omega/2)^2}. \tag{2.16}$$

Comparing this decay rate with the decay rate in a homogeneous medium from eq. 2.14 when the emitter is on resonance with the cavity ($\omega = \omega_c$) and the dipole perfectly aligned to the cavity mode gives

$$F_P = \frac{\Gamma_{cav}}{\Gamma_0} = \frac{3Q}{4\pi^2 V} \left(\frac{\lambda_c}{n}\right)^3, \tag{2.17}$$

where λ_c is the vacuum wavelength of the cavity resonance, $Q = \omega_c/\delta\omega$ is the Q factor of the cavity, and V is the mode volume of the cavity as given by eq. 2.2. The physical interpretation of the mode volume of a waveguide (V) is that the maximum of the field per photon at the antinode is the same as that for a cubic cavity with periodic boundary conditions and real volume V.

Eq. 2.17 gives the enhancement of the decay rate of an emitter in a cavity as first discovered by Purcell [32]. The expression shows that to maximize the Purcell factor the Q factor should be high, meaning low losses, and the mode volume should be small. For this reason microcavities are very interesting candidates for single-photon sources as very small mode volumes and high Q factors can be achieved [33].

Purcell effect in a waveguide

Another interesting structure to investigate is the waveguide. In a waveguide the field is confined in two dimensions thereby resulting in a quasi one-dimensional structure. For a single-mode waveguide the field of the fundamental mode has contributions only perpendicular to the waveguide. The optical density of states is calculated by applying periodic boundary conditions along the waveguide with period a: $ka = 2\pi m$ [34], where k is the wavevector.and m is an integer. There is furthermore a two-fold degeneracy due to positive and negative m. The resulting density of states for the

fundamental mode of a waveguide with only one polarization is

$$\rho(k)\mathrm{d}k = \frac{\mathrm{d}m}{\mathrm{d}k}\frac{\mathrm{d}k}{\mathrm{d}\omega}\mathrm{d}\omega \rightarrow \rho(\omega) = 2\frac{\mathrm{d}m}{\mathrm{d}k}\frac{\mathrm{d}k}{\mathrm{d}\omega} = 2\frac{a}{2\pi}\frac{1}{v_g} \tag{2.18}$$

From this expression and the decay rate in a homogenous medium (eq. 2.14) the Purcell factor of a waveguide can then be calculated as

$$F_P^{\mathrm{wg}} = \frac{\Gamma_{\mathrm{wg}}}{\Gamma_0} = \frac{3\pi c^3}{\omega^2 n^3 v_g A_{\mathrm{eff}}},\ A_{\mathrm{eff}} = \frac{V}{a}, \tag{2.19}$$

where A_{eff} is an effective mode area. In this expression it is assumed that the dipole is oriented perpendicular to the waveguide and positioned at an antinode of the field. This expression is the same as calculated by a different method by Manga Rao and Hughes for a photonic crystal waveguide [14, 15], which is exactly a waveguide with periodic boundary conditions along the waveguide. The interesting thing to notice in this expression is that the Purcell factor scales inversely with the mode area (A_{eff}) and the group velocity (v_g). To achieve a large Purcell factor it is therefore necessary to design a waveguide with a small mode area and a dispersion relation with a large slow down factor below the light line where the mode in confined. This can be achieved in a photonic crystal waveguide, which will be discussed further in chapter 6 where the coupling of quantum dots to photonic crystal waveguides is investigated.

To calculate the Purcell factor of a waveguide the electric field of the waveguide mode and the dispersion relation must be calculated to extract the effective mode area and to calculate the group velocity. In general this is complicated and must be done numerically for structures such as photonic crystal waveguides. However, a simple example of a perfectly conducting waveguide illustrates the frequency dependence of the Purcell factor of a waveguide. The dispersion relation for a waveguide with a cut-off wavelength ω_{co} and the resulting group velocity is given by

$$k = \frac{2\pi}{c}\sqrt{\omega^2 - \omega_{co}^2} \Rightarrow v_g = \frac{\mathrm{d}\omega}{\mathrm{d}k} = \frac{c}{2\pi}\frac{\sqrt{\omega^2 - \omega_{co}^2}}{\omega}. \tag{2.20}$$

This expression shows that the group velocity reach zero at the cut-off frequency and the Purcell factor therefore diverges. In a real physical system this will not be the case and the divergence will be removed by imperfections and the finite size of the waveguide [35]. However, it illustrates that even though the light is only confined in two dimensions a strong enhancement of the emission can still be achieved. Furthermore the light is emitted in a single propagating mode of the waveguide which is very useful for a single photon source as will be further discussed in chapter 6.

2.2.2 Photonic crystals

Instead of increasing the decay rate of the emitter by a structure with a high optical density of states the decay rate can also be lowered by minimizing the density of states. This can be especially useful by minimizing or completely eliminating the density of states into specific modes to suppress emission into these unwanted modes.

An efficient structure do this is a photonic crystal [36]. These are periodic dielectric structures where the refractive index changes on the scale of the wavelength of light. The periodicity of the structures result in Bragg reflection that can prevent light from propagating in the structure.

The simplest example of a photonic crystal is in 1D where it consists of alternating layers of material with different refractive indices. If the optical thickness of the layers are a quarter wavelength the reflections from the interfaces add and by adding enough layers with of high optical quality a very high reflectivity can be reached. This opens a frequency band in the dispersion relation where no optical states are allowed. In 1D this is also called a Bragg mirror but the principle can be extended to a periodic structure in 3D such that no propagating modes are allowed in a certain energy band in any direction [37]. This means that the density of states is zero. This effect is called a photonic band gap as it is similar to the electronic band gap of periodic crystals, where no electrons are allowed to propagate. An interesting effect of a complete photonic bandgap is that an emitter in such a material with an emission frequency in the bandgap will not decay. Complete bandgaps are possible in several structures such as inverse opal

structures [38], wood pile structures [39], and stacks of 2D photonic crystal slabs [40].

A simpler structure to fabricate is two-dimensional photonic crystals. These are dielectric slaps or membranes with a regular grid of a material with different refractive index, typically air holes. In this case no photonic bandgap is present but a significant reduction in the density of states is still possible. However, a complete inhibition of the emission in the plane of the slab can be achieved, which is often called a 2D bandgap. Photonic crystal membranes can be fabricated in semiconductor material using nanoscale lithography. This also makes them the most widely used photonic crystal structures.

The ability to control light-matter dynamics using photonic crystals has been demonstrated experimentally within the last few years [11, 12, 13, 33, 41].

2.2.3 β-factors

An important parameter for single-photon sources is the efficiency of which the photons are emitted into the desired mode. This is characterized by the β-factor which is given by the fraction of photons emitted into the mode and can be expressed from the decay rate into the mode (Γ_m) and the total decay rate of the emitter (Γ_{tot})

$$\beta = \frac{\Gamma_m}{\Gamma_{\text{tot}}} = \frac{\Gamma_m}{\Gamma_m + \gamma}, \tag{2.21}$$

where the total decay rate is given by $\Gamma_m + \gamma$ and γ is the decay rate into other modes. This expression can also be written in terms of the Purcell factor (F_P) of the mode (eq. 2.17) as

$$\beta = \frac{F_P \Gamma_0}{F_P \Gamma_0 + \gamma}. \tag{2.22}$$

From this expression it is seen that there are two routes to a high β-factor. One is to have a high Purcell factor by enhancing the emission of the desired mode. As discussed in section 2.2.1 above the strategy of reaching high

Purcell factors can be achieved in both cavities and waveguides. The other solution is to suppress the emission into other modes thereby reducing γ. One appealing solution is to use photonic crystals as these can result in large inhibition factors of the emission. Structures based on photonic crystals such as cavities and waveguides thereby offer a promising solution for efficient single-photon sources.

2.3 Spontaneous emission of a quantum dot in a high-Q cavity

The decay rates in section 2.2.1 above were calculated using the Wigner-Weisskopf approximation where it is assumed that the optical density of states vary slowly around the emission frequency. For a homogenous medium this is a good approximation, however, in the case of a cavity with a linewidth (Q factor) that is comparable to the linewidth of the emitter this is not the case as the density of states will change strongly with frequency. In the Wigner-Weisskopf approximation the field of the emitted photon do not couple back to the dipole. To investigate a system where a single mode couples strongly to the emitter a model where the cavity mode is explicitly taken into account and the other modes are modeled by an exponential decay of the emitter is needed. The resulting system is illustrated in figure 2.2 and consists of a dipole emitter inside a cavity with a radiative decay into the non-cavity modes of γ. The decay rate of the cavity mode (κ) is given by the Q factor of the cavity: $\kappa = \delta\omega = \omega/Q$. The state vector of the system is given by the state of the emitter and the number of photons in the field. The calculation is done for weak excitation where the quantum dot is excited with a single exciton and the system is allowed to relax to a state where the emitter has decayed and there is no photons in the cavity. The system can then be described by the three following states: The emitter is excited with no photons in the cavity ($|e,0\rangle$), the emitter is in the ground state with one photon in the cavity ($|g,1\rangle$), and the final state where the emitter has decayed to the ground state and there is no photon in the cavity ($|g,0\rangle$). The state vector for the system is then given by $c_1|0,e\rangle + c_2|1,g\rangle + c_3|0,g\rangle$.

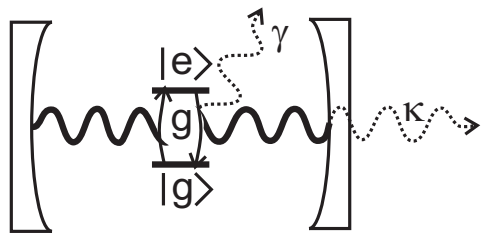

Figure 2.2: The two-level emitter and cavity system considered in the density matrix model. The cavity mode decays with a rate κ and the emitter decays to other modes not in the cavity with a rate γ.

The Hamiltonian in the interaction picture is the Hamiltonian from eq. 2.5 but only interacting with the single cavity mode:

$$\hat{H}_I = -i\hbar\left(g\hat{\sigma}_+\hat{a}e^{i\Delta t} - g^*\hat{\sigma}_-\hat{a}^\dagger e^{-i\Delta t}\right),\ g = E_0\boldsymbol{d}\cdot\boldsymbol{f}(\boldsymbol{r})/\hbar, \tag{2.23}$$

where $\Delta = \omega_0 - \omega_c$ is the detuning of the two-level transition to the cavity mode and g is the coupling constant given by the amplitude of the normalized field (E_0), the dipole moment ($\boldsymbol{d}$), and the normalized field $\boldsymbol{f}(\boldsymbol{r})$.

To calculate the dynamics of the system density matrices will be used. The density matrix equation of motion is given by [29]:

$$\dot{\rho} = -\frac{1}{i\hbar}[H_I,\rho] - \frac{1}{2}\{\Gamma,\rho\},\ H_I = i\hbar\begin{bmatrix} 0 & -ge^{i\Delta t} & 0 \\ g^*e^{-i\Delta t} & 0 & 0 \\ 0 & 0 & 0 \end{bmatrix}, \Gamma = \begin{bmatrix} \gamma & 0 & 0 \\ 0 & \kappa & 0 \\ 0 & 0 & 0 \end{bmatrix}, \tag{2.24}$$

where Γ is the decay matrix with the decay rates of the emitter and the field. The i,j matrix element of the commutator ($[X,\rho] = X\rho - \rho X$) and anticommutator ($\{X,\rho\} = X\rho + \rho X$) is given by $\sum_k(X_{ik}\rho_{kj} - \rho_{ik}X_{kj})$ and $\sum_k(X_{ik}\rho_{kj} + \rho_{ik}X_{kj})$.

To more explicitly relate the equation of motion to the number of photons in the cavity ($\langle\hat{a}^\dagger\hat{a}\rangle$) and the excitation of the emitter ($\langle\hat{\sigma}_+\hat{\sigma}_-\rangle$) it can

be written in term of these expectation values using:

$$\begin{aligned}
\langle\hat{\sigma}_+\hat{\sigma}_-\rangle &= \langle\psi|\hat{\sigma}_+\hat{\sigma}_-|\psi\rangle = |c_1|^2 = \rho_{11} && (2.25)\\
\langle\hat{a}^\dagger\hat{\sigma}_-\rangle &= \langle\psi|\hat{a}^\dagger\hat{\sigma}_-|\psi\rangle = c_1c_2^* = \rho_{12} && (2.26)\\
\langle\hat{a}\hat{\sigma}_+\rangle &= \langle\psi|\hat{\sigma}_+\hat{a}|\psi\rangle = c_2c_1^* = \rho_{21} && (2.27)\\
\langle\hat{a}^\dagger\hat{a}\rangle &= \langle\psi|\hat{a}^\dagger\hat{a}|\psi\rangle = |c_2|^2 = \rho_{22} && (2.28)\\
\langle\hat{\sigma}_-\rangle &= \langle\psi|\hat{\sigma}_-|\psi\rangle = c_3^*c_1 = \rho_{13} && (2.29)\\
\langle\hat{a}\rangle &= \langle\psi|\hat{a}|\psi\rangle = c_3^*c_2 = \rho_{23} && (2.30)
\end{aligned}$$

As $\langle\hat{a}^\dagger\hat{\sigma}_-\rangle = \langle\hat{\sigma}_+\hat{a}\rangle^*$ only the equations for $\langle\hat{a}^\dagger\hat{\sigma}_-\rangle$ will be explicitly written below. The resulting equations of motion for the elements (2.25) to (2.28) are

$$\begin{aligned}
\frac{d\langle\hat{\sigma}_+\hat{\sigma}_-\rangle}{dt} &= -ge^{i\Delta t}\langle\hat{a}\hat{\sigma}_+\rangle - g^*e^{-i\Delta t}\langle\hat{a}^\dagger\hat{\sigma}_-\rangle - \gamma\langle\hat{\sigma}_+\hat{\sigma}_-\rangle && (2.31)\\
\frac{d\langle\hat{a}^\dagger\hat{\sigma}_-\rangle}{dt} &= -ge^{i\Delta t}(\langle\hat{a}^\dagger\hat{a}\rangle - \langle\hat{\sigma}_+\hat{\sigma}_-\rangle) - (\gamma/2+\kappa/2)\langle\hat{a}^\dagger\hat{\sigma}_-\rangle && (2.32)\\
\frac{d\langle\hat{a}^\dagger\hat{a}\rangle}{dt} &= ge^{i\Delta t}\langle\hat{a}\hat{\sigma}_+\rangle + g^*e^{-i\Delta t}\langle\hat{a}^\dagger\hat{\sigma}_-\rangle - \kappa\langle\hat{a}^\dagger\hat{a}\rangle && (2.33)\\
\frac{d\langle\hat{\sigma}_-\rangle}{dt} &= -ge^{i\Delta t}\langle\hat{a}\rangle - \gamma/2\langle\hat{\sigma}_-\rangle && (2.34)\\
\frac{d\langle\hat{a}\rangle}{dt} &= g^*e^{-i\Delta t}\langle\hat{\sigma}_-\rangle - \kappa/2\langle\hat{a}\rangle. && (2.35)
\end{aligned}$$

To solve these equations the explicit time dependence is removed by introducing a transformation of the off diagonal elements: $\langle\hat{a}^\dagger\hat{\sigma}_-\rangle = \overline{\langle\hat{a}^\dagger\hat{\sigma}_-\rangle}e^{i\Delta t}$, $\langle\hat{a}\hat{\sigma}_+\rangle = \overline{\langle\hat{a}\hat{\sigma}_+\rangle}e^{-i\Delta t}$, $\langle\hat{\sigma}_-\rangle = \overline{\langle\hat{\sigma}_-\rangle}e^{i\frac{\Delta}{2}t}$, and $\langle\hat{a}\rangle = \overline{\langle\hat{a}\rangle}e^{-i\frac{\Delta}{2}t}$ leading to the

following system of differential equations:

$$\frac{d\langle\hat{\sigma}_+\hat{\sigma}_-\rangle}{dt} = -g\langle\overline{\hat{a}\hat{\sigma}_+}\rangle - g^*\langle\overline{\hat{a}^\dagger\hat{\sigma}_-}\rangle - \gamma\langle\hat{\sigma}_+\hat{\sigma}_-\rangle \quad (2.36)$$

$$\frac{d\langle\overline{\hat{a}^\dagger\hat{\sigma}_-}\rangle}{dt} = -g(\langle\hat{a}^\dagger\hat{a}\rangle - \langle\hat{\sigma}_+\hat{\sigma}_-\rangle) - (\gamma/2 + \kappa/2 - i\Delta)\langle\overline{\hat{a}^\dagger\hat{\sigma}_-}\rangle \quad (2.37)$$

$$\frac{d\langle\hat{a}^\dagger\hat{a}\rangle}{dt} = g\langle\overline{\hat{a}\hat{\sigma}_+}\rangle + g^*\langle\overline{\hat{a}^\dagger\hat{\sigma}_-}\rangle - \kappa\langle\hat{a}^\dagger\hat{a}\rangle \quad (2.38)$$

$$\frac{d\langle\overline{\hat{\sigma}_-}\rangle}{dt} = -g\langle\overline{\hat{a}}\rangle - (\gamma/2 + i\Delta/2)\langle\overline{\hat{\sigma}_-}\rangle \quad (2.39)$$

$$\frac{d\langle\overline{\hat{a}}\rangle}{dt} = g^*\langle\overline{\hat{\sigma}_-}\rangle - (\kappa/2 - i\Delta/2)\langle\overline{\hat{a}}\rangle. \quad (2.40)$$

The equations 2.36 to 2.38 constitutes a system of differential equations and can be solved to find the time-dependence of the excitation of the emitter and the cavity field. The two last equations will be needed for calculating the spectrum as shown in section 2.3.2 below. In time-resolved measurements it is the rate of change of the population of the emitter that is measured and therefore the one that needs to be solved for comparison with time-resolved measurements. In the case of no detuning ($\Delta = 0$) and a real electric field ($g = g^*$) these equations reduces to three as $\langle\hat{a}^\dagger\hat{\sigma}_-\rangle = \langle\hat{a}\hat{\sigma}_+\rangle$ and can be solved analytically.

The equations will be solved with initial conditions of non-coherent excitation of the emitter corresponding to a single excitation of a quantum dot by a non-resonant pump pulse:

$$\langle\hat{\sigma}_+\hat{\sigma}_-\rangle(0) = 1,\ \langle\hat{a}^\dagger\hat{\sigma}_-\rangle(0) = 0,\ \langle\hat{a}^\dagger\hat{a}\rangle(0) = 0 \quad (2.41)$$

Using these initial values the solution for the population of the emitter is

given by

$$\begin{aligned}\langle\hat{\sigma}_+\hat{\sigma}_-\rangle(t) &= \frac{g^2}{B^2}\Big[-2e^{-(\gamma/2+\kappa/2)t} \\ &+ \Big(\frac{(\gamma/2-\kappa/2)(\gamma/2-\kappa/2+B)}{2g^2}-1\Big)e^{-(\gamma/2+\kappa/2+B)t} \\ &+ \Big(\frac{(\gamma/2-\kappa/2)(\gamma/2-\kappa/2-B)}{2g^2}-1\Big)e^{-(\gamma/2+\kappa/2-B)t}\Big], \\ & B=\sqrt{(\gamma/2-\kappa/2)^2-4g^2} \end{aligned} \tag{2.42}$$

An important parameter for the time evolution of the solution is the constant B which can either be real or imaginary depending of the parameters of the system ($\gamma,\ \kappa,\ g$). If $|\gamma-\kappa|<4g$, B is imaginary and the energy of the system oscillates between the light field of the cavity ($\langle\hat{a}^\dagger\hat{a}\rangle$) and the excitation ($\langle\hat{\sigma}_+\hat{\sigma}_-\rangle$). This is called the strong coupling regime and has been demonstrated with atoms [42], semiconductor quantum wells [43], and with quantum dots in microcavities [44, 45, 46, 13]. In the extreme case of a lossless system ($\kappa=\gamma=0$) the solution reduces to a pure Rabi oscillation with a Rabi frequency of $2g$.

If $|\gamma-\kappa|>4g$, B is real and the excitation decays exponentially. The case typically encountered for quantum dots in micro cavities is $\gamma\ll g\ll\kappa$ as the homogenous linewidth is typically small ($\gamma\sim 1$ GHz), Q factors in cavities with quantum dots reach 30000 at a resonance wavelength of 1 μm resulting in $\kappa>100$ GHz, and the coupling constant g is in between, e.g. for a typical mode volume $V=1\ \mu\text{m}^3$ and a dipole moment of $1\cdot10^{-28}$ Cm [23] the coupling constant is 16 GHz. In this limit the solution reduces to an exponential decay

$$\langle\hat{\sigma}_+\hat{\sigma}_-\rangle(t)=e^{-(\frac{4g^2}{(\kappa-\gamma)}+\gamma)t}\Rightarrow\Gamma_{cav}=\frac{4g^2}{(\kappa-\gamma)}+\gamma. \tag{2.43}$$

This shows that the cavity adds an additional decay rate which is proportional to the coupling to the cavity field and the Q factor of the cavity. The decay rate of the emitter in the cavity Γ_{cav} can then be compared to the expression obtained in eq. 2.17 from Fermis golden rule in the case where

there is only decay into the cavity ($\gamma = 0$). Inserting the decay rate from eq. 2.43 and eq. 2.14 the expression for the Purcell factor of eq. 2.17 is found

$$F_P = \frac{\langle \Gamma_{cav} \rangle}{\Gamma_0} = \frac{3Q}{4\pi^2 V} \left(\frac{\lambda}{n}\right)^3 \frac{\langle |\boldsymbol{d} \cdot \boldsymbol{f}(\boldsymbol{r})| \rangle^2}{|\boldsymbol{d}|^2}, \tag{2.44}$$

with the addition of the orientation of the dipole to the field.

If a high Purcell effect is desired, as e.g. for single-photon sources the device should be designed with a high Q factor and small mode volume. However, it may not be desirable to reach the strong coupling regime. For this reason cavity based single-photon sources could operate in an "intermediate" coupling regime where g is just slightly below κ. In this regime the decay will not be described by a single exponential and the full solution is needed.

Decay curves for high-Q cavities

To investigate the deviation from the Purcell expression of (eq. 2.43) the decay curves for typical values of the cavity decay rate have been calculated numerically using typical values for quantum dots ($g = 16$ GHz, $\gamma = 1.6$ GHz). The decay curves are plotted in figure 2.3 along with a fit to an exponential decay. For the the two lowest Q values ($\kappa = 4000g,\ 40g$) the decay is exponential and the Purcell effect is seen to enhance the decay rate as the cavity Q increases. For the decay at the critical value of Q at the transition to strong coupling the decay is no longer exponential and the fit underestimates the decay rate. When the strong coupling regime is reached for $\kappa < 4g$ the Rabi oscillation is observed and the population switches back and forth with the cavity field and remains in the cavity longer than at the critical point due to the slow decay out of the cavity.

To quantify the deviation from eq. 2.43 the decay rate as a function of κ is shown in the right part of figure 2.3. In an experiment the measured decay curve will often be modeled by an exponential decay when doing the analysis and to compare with this the decay rate has been obtained by such a fit to the calculated decay curve. Another way of characterizing the decay is from the fastest decay rate of the curve. Both of these values

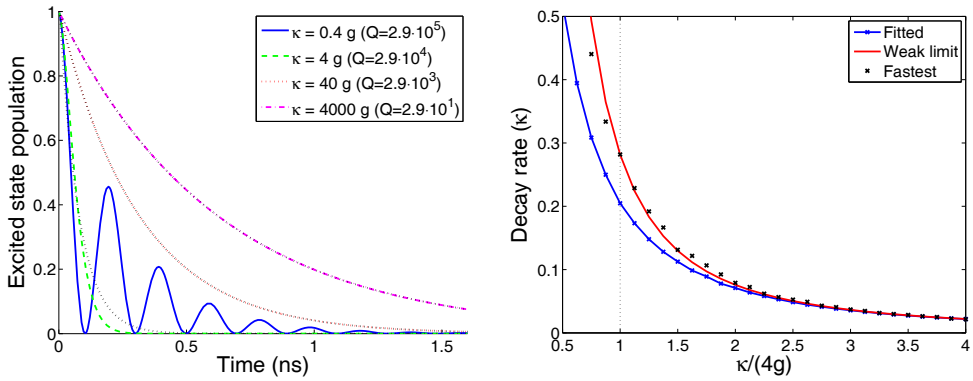

Figure 2.3: Left: The excited state decay ($\langle\hat{\sigma}_+\hat{\sigma}_-\rangle(t)$) for different values of the cavity decay rate (κ) or Q factor. The decay curves are calculated by numerical solving the density matrix equations with no detuning and a coupling strength $g = 16$ GHz and $\gamma = 1.6$ GHz. The dashed black lines show an exponential decay fitted to the decay curves for $\kappa = 4g$, $40g$, and $400g$. Right: The decay rate as a function of the cavity decay rate (κ). The values used for γ and g is the same as the left plot. The blue line shows the decay obtained by fitting an exponential function to the calculated decay curve and the black dots show the decay rate of the fastest decay rate of the curve. The red line shows the expression for the decay rate in the weak coupling limit (eq. 2.43).

have been plotted in figure 2.3 along with the value calculated in the weak coupling regime from eq. 2.43. As was seen in the left part of figure 2.3 the decay rate is underestimated as Q increases (or κ decrease). At the critical point ($\kappa = 4g$) a deviation of 23% is seen between the fitted decay rate and the value in the weak coupling limit. However, this deviation is only seen for values of $\kappa < 10g$. For the fastest decay rate of the curve the value is seen to follow eq. 2.43 well and only deviate a little in the part strong coupling regime plotted. This means that modeling measured decay curves with an exponential decay, using the weak coupling limit, is valid even at high Purcell factors but care should be taken when the system is close to strong coupling.

Decay curves as a function of detuning

The decay rate of the emitter in the weak coupling regime follows the Lorentzian line shape of the cavity as shown by eq. 2.16. To investigate the deviation from this expression for high-Q cavities the decay curves as a function of detuning is calculated. Two such decay curves are shown in the left part of figure 2.4. In this figure the decay curves for a decay with a high Purcell factor is shown. Here the decay rate is seen to decrease as the detuning is increased. An example in the strong coupling regime is also shown ($\kappa = 0.4g$) where it can also be found that the oscillation of the population does not go to zero thereby decreasing the amplitude of the oscillation with higher detunings. The decay rate is also seen to decrease. To investigate what effect the deviations from the weak coupling regime have on the decay rate as a function of detuning the decay curves have been calculated for two small values of κ as a function of detuning and the curves fitted to a single exponential decay. The first value of κ is at the critical point to strong coupling ($\kappa = 4g$) and the other is at $\kappa = 40g$. The result of the decay rates of a fit to the decay curves are shown as blue lines in the right part of figure 2.4. A curve where dephasing is included is also seen in the figure and will be discussed below. To compare with the expression for the weak coupling regime this has also been plotted as black lines in the figure. The calculation shows that there is a significant deviation at resonance as already discussed

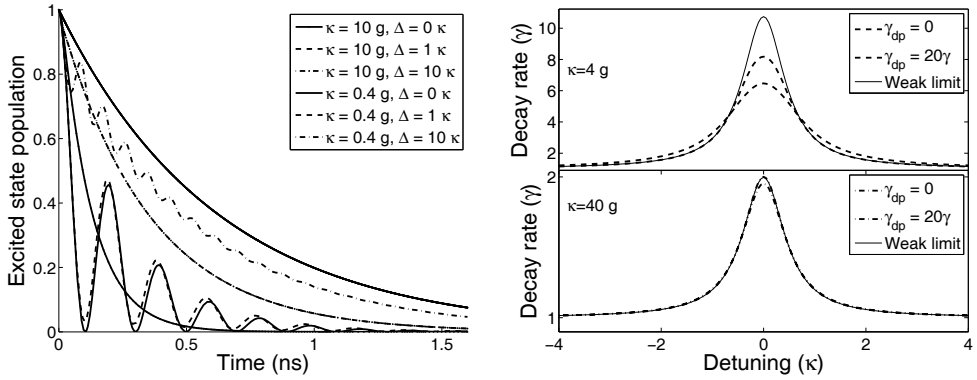

Figure 2.4: Left: Decay curves as a function of detuning. The parameters used are the same as in figure 2.3 ($\gamma = 1.6$ GHz, $g = 16$ GHz). The decay curves are plotted in the case of a high Purcell factor ($\kappa = 10g$) and strong coupling ($\kappa = 0.4g$). Right: The decay rate obtained by fitting an exponential decay to the calculated decay curves as a function of the detuning. The values of the upper panel is calculated at the critical coupling point $\kappa = 4g$ and the lower panel is for $\kappa = 40g$. Both curves have also been calculated with a dephasing rate of 20γ shown by the green lines. The black lines are Lorentzian functions calculated using eq. 2.16 obtained from Fermis golden rule.

above. The deviation is also seen to decrease when the detuning increase. The effect is that a broader line is observed. For a cavity with $\kappa = 40g$ the effect seen in the lower panel is found to be small. However, the calculations show again that care should be taken when interpreting measurements of a system close to strong coupling.

2.3.1 Decay dynamics with the inclusion of dephasing

Dephasing of the system can be included by introducing a random time dependent energy shift of the emitter $\delta\omega(t)$ such that $\Delta \rightarrow \Delta + \delta\omega(t)$. It is assumed that the noise is gaussian with zero mean value ($\langle\delta\omega(t)\rangle =$

0) and that the variations happens on a timescale of $1/\gamma_{dp}$ that is fast compared to the other timescales of the system such that there is no history ($\langle \delta\omega(t)\delta\omega(t')\rangle = 2\gamma_{dp}\delta(t-t')$). This will result in an extra decay of the off diagonal elements of the equation of motion [29]:

$$\begin{aligned}
\frac{d\langle\overline{\hat{a}^\dagger\hat{\sigma}_-}\rangle}{dt} &= -g(\langle\hat{a}^\dagger\hat{a}\rangle - \langle\hat{\sigma}_+\hat{\sigma}_-\rangle) \\
&\quad -(\gamma/2+\kappa/2+\gamma_{dp}/2-i\Delta)\langle\overline{\hat{a}^\dagger\hat{\sigma}_-}\rangle \qquad (2.45)\\
\frac{d\langle\overline{\hat{\sigma}_-}\rangle}{dt} &= -g\langle\overline{\hat{a}}\rangle - (\gamma/2+\gamma_{dp}/2+i\Delta/2)\langle\overline{\hat{\sigma}_-}\rangle \qquad (2.46)\\
\frac{d\langle\overline{\hat{a}}\rangle}{dt} &= g^*\langle\overline{\hat{\sigma}_-}\rangle - (\kappa/2-i\Delta/2)\langle\overline{\hat{a}}\rangle. \qquad (2.47)
\end{aligned}$$

Eq. 2.45 can now be used with eq. 2.36 and eq. 2.38 to calculate the time-dependent decay curves of the atom cavity system including dephasing and detuning. The equations no longer have a simple analytical solution but can easily be calculated numerically. To illustrate the influence of adding dephasing to the decay some examples of decay curves are shown in figure 2.5.

The left plot of figure 2.5 shows the excited state decay calculated using the same value of the coupling and emitter decay rate as above ($g = 16$ GHz, $\gamma = 1.6$ GHz) for different cavity decay rates (κ) and dephasing rates (γ_{dp}). The dephasing rates shown are chosen to cover the values for quantum dots up to a temperature of ~ 200 K [26]. For the largest cavity decay rate of $40g$ plotted $\kappa > g, \gamma$ and it is seen that the influence of dephasing is small. However, when the system gets close to strong coupling ($\kappa = 10g$) a large influence is observed where the decay rate is reduced. When the system is in the strong coupling regime the dephasing damps the oscillations and eventually reduce the decay to an exponential.

As the dephasing increases the linewidth of the emitter increases and another way of seeing the effect is that when the emitter linewidth gets large compared to the cavity linewidth the coupling is reduced. The influence of dephasing on the decay rate as a function of detuning is also shown in the right part of figure 2.4. This also shows that there is an increased effect

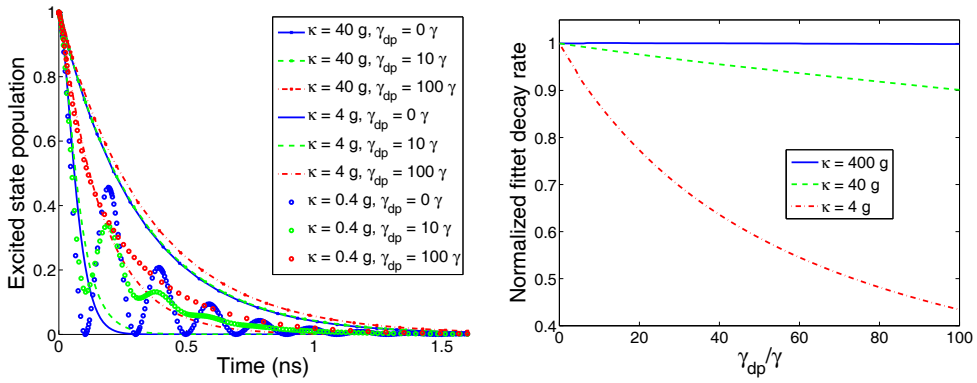

Figure 2.5: Left: Influence of dephasing on the excited state decay ($\langle\hat{\sigma}_+\hat{\sigma}_-\rangle(t)$) for different values of the cavity linewidth (κ). The decay curves are calculated by solving the density matrix equations numerically with a value of the coupling $g = 16$ GHz. Solutions for three values of the cavity decay rate is shown corresponding to the weak coupling regime ($\kappa = 40g$ and $\kappa = 40g$) and the strong coupling regime ($\kappa = 0.4g$). Right: The influence of dephasing on the decay rate of the emitter. The decay rate is found by fitting an exponential decay to the calculated decay curve and the decay rate normalized to the decay rate with no dephasing is plotted. The decay rate is plotted for three different cavity decay rates one at the critical decay rate ($\kappa = 4g$) and two for different weak coupling parameters ($\kappa = 40g$ and $400g$).

on the linewidth measured with dephasing in high-Q cavities. It should be noted that the value of κ of $4g$ where a significant effect is seen still corresponds to a large, but not unrealistic, Q factor of $\sim 3 \cdot 10^4$. This shows that dephasing is important when interpreting the decay rate of quantum dots in cavities with high Purcell factors, but also that it should be included in a quantitative description of time-resolved measurements of a quantum dot in a high-Q cavity.

2.3.2 Emission spectra

The spectrum of the spontaneous emission can be calculated from the Wiener-Khintchine theorem from the two-time correlation function of the atomic operators [29]

$$2\pi S(\omega) = \int_0^\infty dt \int_0^\infty dt' \langle E^-(t)E^+(t')\rangle e^{-i\omega(t'-t)}, \tag{2.48}$$

in a pulsed experiment with a pulse at $t = 0$ this can be written as a function of the time difference $\tau = t - t'$ [47]:

$$S(\omega) \propto Re\left(\int_0^\infty d\tau e^{-i\omega\tau} \int_0^\infty dt' \langle \hat{\sigma}_+(t'+\tau)\hat{\sigma}_-(t')\rangle\right) \tag{2.49}$$

To calculate the correlation function $\langle \hat{\sigma}_+(t+\tau)\hat{\sigma}_-(t)\rangle$ the quantum regression theorem is used. According to this the correlation functions $C_s(t'+\tau, t') = \langle \hat{\sigma}_+(t'+\tau)\hat{\sigma}_-(t')\rangle$ and $C_a(t'+\tau, t') = \langle \hat{\sigma}_+(t'+\tau)\hat{a}(t')\rangle$ follow the same equation of motion as $\langle \hat{\sigma}_-\rangle$ and $\langle \hat{a}\rangle$ (eq. 2.46 and 2.47) with the initial conditions $C_s(t', t') = \langle \hat{\sigma}_+\hat{\sigma}_-\rangle(t')$ and $C_a(t', t') = \langle \hat{\sigma}_+\hat{a}\rangle(t')$. These initial conditions are given by the solution of equation 2.36, 2.38, and 2.45 [48]. The equation of motion for $C_s = \bar{C}_s e^{i\frac{\Delta}{2}t}$ and $C_a = \bar{C}_a e^{-i\frac{\Delta}{2}t}$ are then given by the equation of motion of $\langle \overline{\hat{\sigma}_-}\rangle$ from eq. 2.46 and $\langle \bar{\hat{a}}\rangle$ from eq. 2.47:

$$\partial_\tau \bar{C}_s = -g\bar{C}_a - (\gamma/2 + \gamma_{dp}/2 + i\Delta/2)\bar{C}_s \tag{2.50}$$

$$\partial_\tau \bar{C}_a = g^*\bar{C}_s - (\kappa/2 + \gamma_{dp}/2 - i\Delta/2)\bar{C}_a \tag{2.51}$$

The above equations can be solved analytically and the solution for $\bar{C}_s(t'+\tau,t')$ is given by

$$\bar{C}_s(t'+\tau,t') = \frac{1}{2B}e^{-\frac{1}{4}\tau(B+\gamma+\kappa+2\gamma_{dp})}\Big[-4\bar{C}_a(t',t')\left(e^{\frac{B}{2}\tau}-1\right)g + C_s(t',t')\left(B+\gamma-\kappa+2i\Delta+e^{\frac{B}{2}\tau}(B-\gamma+\kappa-2i\Delta)\right)\Big], \tag{2.52}$$

where $B=\sqrt{(\gamma-\kappa+2i\Delta)^2-16g^2}$. This equation can now be inserted in the τ-integral in eq. 2.49 which can then be solved

$$\int_0^\infty d\tau e^{-i(\omega-\Delta/2)\tau}\bar{C}_s(t'+\tau,t') = \frac{2(C_s(t',t')(2i\omega+\gamma_{dp}-2i\Delta+\kappa)-2C_a(t',t')g)}{4g^2-(2\omega-i(\gamma+\gamma_{dp}))(2\omega-i(\gamma_{dp}-2i\Delta+\kappa))}. \tag{2.53}$$

In the general case with detuning and dephasing the initial $C_s(t',t')$ and $C_a(t',t')$ can only be calculated numerically. To calculate the spectra in this case the time-dependence of the decay curves are calculated numerically as a function of t and inserted in the solution of the integral in eq. 2.53 and the integral in t' is then done numerically.

Examples of calculated spectra as a function of cavity-quantum dot detuning are seen in figure 2.6. The spectra were calculated with the same values of the coupling and homogenous linewidth as used above and three different values of κ. The left most series is calculated for a cavity decay of $0.4g$ which is in the strong coupling regime and the avoided crossing and spectral splitting of the peaks on resonance are readily seen. The middle series is for $\kappa=4g$, which is at the edge of strong coupling and the broadening of the quantum dot peak on resonance is seen due to the increased decay rate. The last series of spectra is calculated with $\kappa=10g$ which is in the weak coupling regime and the quantum dot peak is seen to cross the cavity resonance with a small increase in linewidth. In measured spectra of the cavity emission an increase in the intensity would be seen when the quantum dot reaches the cavity resonance due to the increase in the β factor which is not taken into account in the calculation.

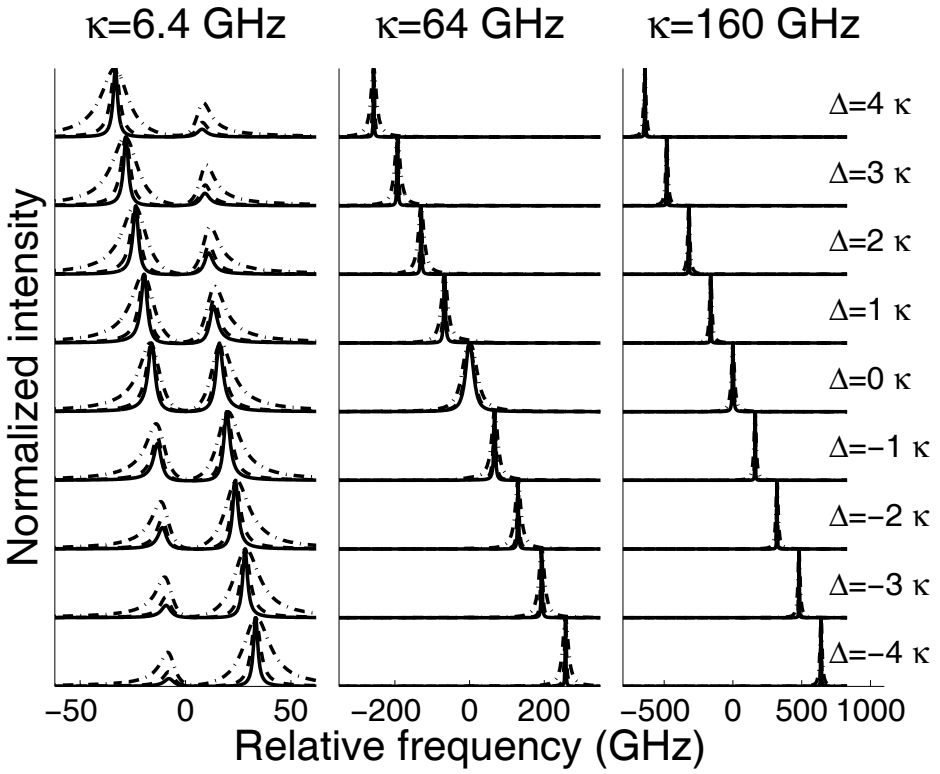

Figure 2.6: Calculated emission spectra scaled to the maximum of the spectrum. The values used for the coupling and homogenous linewidth is $g = 16$ GHz and $\gamma = 1.6$ GHz. Each column shows spectra as a function of the cavity-quantum dot detuning (Δ) for three values of the cavity decay rate (κ). For each of these parameters the spectra have been calculated with a dephasing rate of 0 (solid line), 16 GHz (dashed line), and 160 GHz (dash-dotted line).

The spectra are also shown with a dephasing rate of 16 GHz and 160 GHz to illustrate the effect of dephasing on the spectra. The dephasing is seen to increase the line width of the emitter but also to increase the amount of light emitted from the cavity peak. This is most notable in the case of strong coupling but it is also visible in the middle series of spectra.

2.4 Single-photon statistics and the Hanbury-Brown and Twiss experiment

The characteristic property of a single-photon source is the photon statistics characterized by the emission of one and only one photon per excitation. The statistics of a single photon source is very different from coherent and thermal sources that has a finite probability of emitting more than one photon per excitation.

To characterize a light source as a single-photon source the photon statistics should consequently be measured. The single-photon detectors typically used for detection cannot distinguish between one or multiple photons and the photon statistics can therefore not be measured directly. Instead a Hanbury-Brown and Twiss (HBT) setup is used [49]. In the optical version the light is incident on a beamsplitter with single photon detectors on each output arm as shown in the left part of figure 2.7. The correlation between the arrival time of photons in the two detectors is then measured. For a single-photon source there will never be a click in both detectors at the same time resulting in a correlation of 0 at a time delay of 0.

The time correlation of the detectors is calculated as the normalized second order coherence of the outputs of the beam splitter. For a single mode of light the normalized second order coherence is given by

$$g^{(2)}(\tau) = \frac{\langle \hat{a}^\dagger(t)\hat{a}^\dagger(t+\tau)\hat{a}(t+\tau)\hat{a}(t)\rangle}{\langle \hat{a}^\dagger(t)\hat{a}(t)\rangle\langle \hat{a}^\dagger(t+\tau)\hat{a}(t+\tau)\rangle} \tag{2.54}$$

For $\tau = 0$ this can be written in terms of the photon number operator

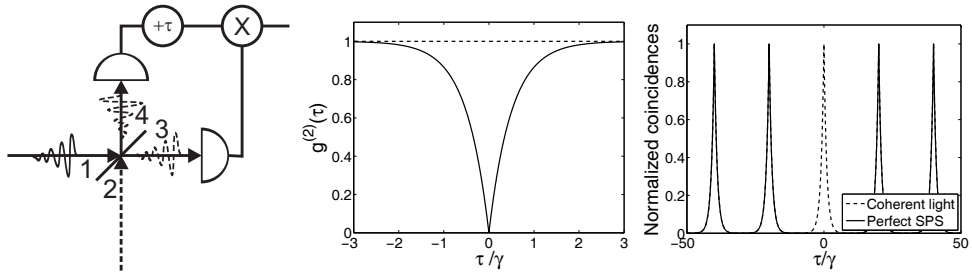

Figure 2.7: Left:Hanbury-Brown and Twiss (HBT) beam splitter setup for measuring $g^{(2)}(\tau)$. The photon enters port 1 and exits either to the detector in 3 or 4. Middle: Second order coherence ($g^{(2)}(\tau)$) for an exponentially decaying emitter with a rate of γ and incoherent continuous wave excitation (solid line). For reference the second order coherence of a coherent light source is also shown (dashed line). Right: Hanbury-Brown and Twiss measurement of a perfect single photon source with a decay rate of γ and pulsed excitation with a repetition rate of 20γ. The signal for coherent light is also shown (dashed line).

($\hat{n} = \hat{a}^\dagger \hat{a}$)

$$g^{(2)}(0) = \frac{\langle \hat{a}^\dagger \hat{a}^\dagger \hat{a} \hat{a} \rangle}{\langle \hat{a}^\dagger \hat{a} \rangle \langle \hat{a}^\dagger \hat{a} \rangle} = \frac{\langle \hat{n}(\hat{n}-1) \rangle}{\langle \hat{n} \rangle^2} = \frac{\langle n^2 \rangle - \langle n \rangle}{\langle n \rangle^2}, \tag{2.55}$$

For a coherent state $\langle n^2 \rangle = \langle n \rangle^2 + \langle n \rangle$ resulting in $g^{(2)}_{\mathrm{coh}}(0) = 1$ which shows that the second order coherence is independent on τ. For a thermal state $g^{(2)}_{\mathrm{coh}}(0) = 2$. For a photon number or Fock state $\langle n^2 \rangle = \langle n \rangle^2$ giving a second order coherence of $g^{(2)}_{\mathrm{coh}}(0) = (n-1)/n$. For a single photon state this gives $g^{(2)}_{\mathrm{coh}}(0) = 0$, which distinctively differentiates the single-photon state from coherent, thermal and multi-photon states. For a two-photon state $g^{(2)}_{\mathrm{coh}}(0) = 1/2$ and for this reason $g^{(2)}_{\mathrm{coh}}(0) < 1/2$ is often used as a practical definition of a single photon source, however, a completely pure single photon source will have $g^{(2)}(0) = 0$.

To calculate what is measured in a HBT setup the correlation of the

output arms of the beamsplitter in figure 2.7 is calculated. For a beam splitter with equal transmission and reflection and without losses the fields at the output arms are given by

$$\hat{a}_3(t) = \frac{1}{\sqrt{2}}(\hat{a}_1(t) + \hat{a}_2(t)) \quad (2.56)$$

$$\hat{a}_4(t) = \frac{1}{\sqrt{2}}(\hat{a}_1(t) - \hat{a}_2(t)) \quad (2.57)$$

The correlation measured between the two detectors with a time delay τ and normalized to the value for large time delays is

$$g^{(2)}_{3,4}(\tau) = \frac{G^{(2)}_{3,4}(\tau)}{\lim_{\tau\to\infty} G^{(2)}_{3,4}(\tau)} = \frac{\langle \hat{a}^\dagger_3(t)\hat{a}^\dagger_4(t+\tau)\hat{a}_4(t+\tau)\hat{a}_3(t)\rangle}{\langle \hat{a}^\dagger_3(t)\hat{a}_3(t)\rangle\langle \hat{a}^\dagger_4(t)\hat{a}_4(t)\rangle}. \quad (2.58)$$

Inserting the beam splitter transmission from eq. 2.56 and 2.57 into the equation with no photon in port 2 of the beam splitter results in the normalized second order coherence of eq. 2.54. This shows that the HBT setup measures the second order coherence and for this reason the HBT setup is the standard way to prove that a source emits single photons. This was first experimentally demonstrated on fluorescence from sodium atoms in 1977 by Kimble et al. [50] and was demonstrated for quantum dots in 2000 by Michler et al. [51].

The HBT measurement can either be done on a pulsed source or for a continuous wave (cw) source. For optically excited quantum dots this corresponds to pulsed or cw excitation. The correlation signal measured in the two cases is illustrated in the middle and right part of figure 2.7. In a cw experiment the correlation will give at dip at $\tau = 0$ and for incoherent cw excitation of an emitted with an exponential decay rate γ the correlation signal will be given by $1 - e^{-2\gamma|\tau|}$ [52] and is illustrated in the middle part of figure 2.7. With pulsed emission the correlations will result in a series of peaks and for a pulse separation much larger than the decay rate of the source the area of the central peak will be reduced compared to the non-central peaks to the value of $g^{(2)}(0)$. For a perfect single-photon source the central peak will then vanish as illustrated in the right part of figure 2.7. Theoretically the two measurements are equally good, however, experimental conditions such as the type of source, count rates, dark counts and time

jitter of the detectors makes these more or less practical and pulsed experiments are often preferred which will be further discussed in connection with experiment in chapter 5.

2.4.1 Second order coherence measurements with a background contribution

In a real experimental setup the input field is newer in a pure single-photon state. To investigate the second order coherence of a state that is a combination of a single-photon state and a coherent state the second order coherence is calculated. The field operator is written as $\hat{a}_1 = \hat{a} + \hat{b}$ and the input state is given by the $|1, \psi_b\rangle$, where $|1\rangle$ denotes a single photon state and $|\psi_b\rangle$ is the 'polluting' state and $\hat{a}|1, \psi_b\rangle = |0, \psi_b\rangle$. This state will result in contribution to the correlation signal where a photon from the field b is detected in one of the detectors and the single photon is detected in the other increasing the measured value of the second order concrescence at $\tau = 0$. The second order coherence is then given by (ignoring the factors of $\frac{1}{\sqrt{2}}$)

$$\begin{aligned} G^{(2)}_{3,4}(t,\tau) &= \left\langle \left(\hat{a}^\dagger(t) + \hat{b}^\dagger(t)\right)\left(\hat{a}^\dagger(t+\tau) + \hat{b}^\dagger(t+\tau)\right) \right. \\ &\quad \left. \times \left(\hat{a}(t+\tau) + \hat{b}(t+\tau)\right)\left(\hat{a}(t) + \hat{b}(t)\right) \right\rangle \qquad (2.59) \\ &= \left\langle \hat{b}^\dagger(t)\hat{b}(t)\right\rangle + \left\langle \hat{b}^\dagger(t+\tau)\hat{b}(t+\tau)\right\rangle \\ &\quad + \left\langle \hat{b}^\dagger(t)\hat{b}(t+\tau)\right\rangle + \left\langle \hat{b}^\dagger(t+\tau)\hat{b}(t)\right\rangle \\ &\quad + \left\langle \hat{b}^\dagger(t)\hat{b}^\dagger(t+\tau)\hat{b}(t+\tau)\hat{b}(t)\right\rangle . \qquad (2.60) \end{aligned}$$

The result is a combination of photon numbers ($n_b = \langle \hat{b}^\dagger \hat{b}\rangle$), first order coherences ($\langle \hat{b}^\dagger(t)\hat{b}(t+\tau)\rangle$) and second order coherence. These can be calculated for different sources of light [52]. The field b is assumed to be first order incoherent such that $\langle \hat{b}^\dagger(t)\hat{b}(t+\tau)\rangle = 0$ and without antibunching which is the case for chaotic light, except for small τ where the first order coherence approaches 1 and the normalized second order coherence approaches 2. Using these assumptions the normalized second order coherence is given

by

$$g^{(2)}(0) = \frac{2n_b + n_b^2}{(1+n_b)^2}. \tag{2.61}$$

The expression shows that such a background contribution is important to reduce. The calculation is done for a single photon in the field a which means that n_b is the number incoherent photons per single photon. As an example a contribution from the incoherent state b equal to the contribution from the single photon state will result in a measured $g^{(2)}(0)$ of 0.75.

2.5 Photon indistinguishability

Many applications of single photons in quantum information are dependent on the interference of single photons to generate entanglement. This can only be achieved by using indistinguishable photons meaning that the individual photons have the same frequency, polarization, and time-dependence such that they cannot be separated if they overlap in time and spatial mode. Especially in the general case of linear quantum computing this is the key element [2]. The entanglement can be generated by sending two indistinguishable photons on to each port of a beam splitter. As photons are bosons they obey Bose-Einstein statistics which will result in both photons exiting the beam splitter on the same output.

Indistinguishable single photons were first demonstrated with photons generated by parametric down conversion [53] and later on photons from quantum dots in micropillar cavities [8]. In the first experiment ([53]) the generated photons are correlated as they are generated in the same process but in the latter ([8]) the photons are generated from independent processes which can be repeated to generate as many photons as desired.

To measure the photon indistinguishability the same principle as in the HBT measurement is used with two photons combined on the beam splitter instead of one and the photon correlation of the output is measured. The system is shown in figure 2.8.

The time correlation is again calculated from the normalized second order coherence of the two outputs. The second order coherence is calculated

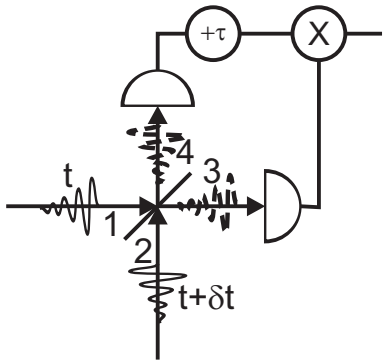

Figure 2.8: The setup for measuring the indistinguishability of two photons. The photons enter the beam splitter at port 1 and 2 and the correlations of the output port 3 and 4 is measured.

by inserting the beam splitter equations from eq. 2.56 and 2.57 into the second order coherence of eq. 2.58:

$$\begin{aligned} G^{(2)}_{3,4}(0) &= \tfrac{1}{2}\Big(\langle \hat{a}_1^\dagger \hat{a}_1^\dagger \hat{a}_1 \hat{a}_1\rangle + \langle \hat{a}_2^\dagger \hat{a}_2^\dagger \hat{a}_2 \hat{a}_2\rangle \\ &\quad -\langle \hat{a}_1^\dagger \hat{a}_2^\dagger \hat{a}_1 \hat{a}_2\rangle + \langle \hat{a}_1^\dagger \hat{a}_2^\dagger \hat{a}_2 \hat{a}_1\rangle + \langle \hat{a}_2^\dagger \hat{a}_1^\dagger \hat{a}_1 \hat{a}_2\rangle - \langle \hat{a}_2^\dagger \hat{a}_1^\dagger \hat{a}_2 \hat{a}_1\rangle\Big) \\ \Rightarrow g^{(2)}_{3,4}(0) &= 2g^{(2)}(0) - |g^{(1)}(0)|^2 + 1, \end{aligned} \tag{2.62}$$

where $g^{(2)}$ is the normalized second order coherence and $g^{(1)}$ is the normalized first order coherence of the input fields given by

$$g^{(1)}(\tau) = \frac{\langle \hat{a}_1^\dagger(t)\hat{a}_2(t+\tau)\rangle}{\langle \hat{a}_1^\dagger(t)\hat{a}_2(t)\rangle}. \tag{2.63}$$

The input field used to evaluate this is given by two single-photon wave packets with the same temporal shape but with a small difference in arrival time (δt). The state can be written as

$$|\Psi\rangle = \int_0^\infty \int_0^\infty dt_1 dt_2 x_1(t_1) x_2(t_2) \hat{a}_1^\dagger(t_1) \hat{a}_2^\dagger(t_2+\delta t)|0\rangle, \tag{2.64}$$

where $x_{1,2}(t)$ defines the temporal shape of the wave packet that depends on the emission properties of the emitter (e.g. as discussed in section 2.3). From this expression the first order coherence can be calculated and defined as the overlap of the wave packets

$$|g^{(1)}|^2 = \left| \int x_1(t) x_2^*(t+\delta t) dt \right|^2 = V(\delta t), \tag{2.65}$$

where δt is the difference in arrival time of the photons on the beam splitter. For two perfectly indistinguishable single-photons ($x_1(t) = x_2(t)$) with no time delay the overlap is unity and the second order coherence is 0 as both photons will either go to the detector in arm 3 or 4 of the setup.

2.5.1 Dephasing

For single photons emitted at different times the wave packet of the photons will change due to random interactions of the environment characterized by the dephasing of the emitter. For solid-state emitters this can be significant and will limit the indistinguishability of the emitted photons.

In a model where dephasing is introduced in a similar way as in section 2.3.1 above, such that the result is an exponential decay of the coherence with a rate γ_{dp}, the overlap is given by [54]:

$$V(\delta t) = \frac{\gamma}{\gamma + \gamma_{dp}} e^{-(\gamma+\gamma_{dp})|\delta t|} + \frac{\gamma}{\gamma_{dp}} \left(e^{-\gamma|\delta t|} - e^{-(\gamma+\gamma_{dp})|\delta t|} \right) \tag{2.66}$$

For no time delay between the photons ($\delta t = 0$) the overlap of the photons is given by

$$V(0) = \frac{\gamma}{\gamma + \gamma_{dp}}. \tag{2.67}$$

This shows that improving the indistinguishability of photons from a single-photon source can either be achieved by increasing the spontaneous emission decay rate (γ) or reducing the dephasing rate (γ_{dp}). For quantum dot sources as the ones investigated in this thesis this can be achieved by using structures with a high Purcell factor to increase γ and going to low temperatures to decrease γ_{dp}. Cavities or waveguides at low temperatures should

therefore be good candidates for single-photon sources with indistinguishable photons.

It should also be noted that the decay rate (γ) can be found from time-resolved measurements and the indistinguishability can therefore be used to measure the dephasing rate of the emitter.

Chapter 3

Experimental setup for time-resolved photoluminescence of single quantum dots

To investigate the emission from quantum dot based single-photon sources a setup has been established to measure photoluminescence from single quantum dots in nanophotonic structures.

To only measure the photoluminescence of a single quantum dot the emission from the individual quantum dots needs to be isolated. This can be done by utilizing the difference in position and emission frequencies of the individual quantum dots. As described in section 2.1 the random nature of the quantum dot formation results in random positioning of the quantum dots and an inhomogeneous broadening of the emission frequencies. To distinguish the emission lines of the individual quantum dots as few dots as possible should be optically addressed such that the remaining lines can be spectrally separated. As we are concerned with single emitters the light emission is limited to a single photon per excitation cycle and it will therefore be very important to have as high a collection and detection efficiency as possible.

In addition the sample must be cooled to low temperatures and a suit-

able pulsed source for excitation is needed for time-resolved measurements. The setup can be grouped in four parts: the cryogenic part for cooling and positioning the sample, the excitation of the sample, the collection and detection of the emitted photoluminescence.

In this chapter the four parts of the setup will be described addressing the above requirements and discussing the different design considerations and the solutions chosen along with characterizations of the performance of the individual parts.

3.1 Cryostat and sample mounting

To cool the sample to low temperatures a cryostat is used. The cryostat should have good optical access to allow the use of optics with a large collection angle or numerical aperture (NA) and also allow for the possibility of excitation from another angle than the detection to avoid a direct reflection of the excitation light into the collection optics.

The positional and vibrational stability of the sample is important as the measurements will be done on structures with dimensions that are smaller or comparable to the optical resolution of the setup and long measuring times will be needed. The positional stability should therefore be much smaller than the optical resolution which is on the order of 1 μm.

The cryostat used satisfying these requirement is a Microstat HiRes II cryostat from Oxford Instruments. This cryostat is made for microscopy and has a high stability and small positional drift with good optical access from a top window with a diameter of 25 mm, a thickness of 1.5 mm, and an additional distance to the sample of $\sim$ 2 mm. This gives optical access in a large solid angle. The cryostat is primarily cooled by liquid helium and can reach a temperature of 3.2 K.

The cryostat is based on a cold finger in vacuum and the heat of the sample is removed by the thermal contact to the cold finger. As there will be heating of the sample from the excitation laser and thermal radiation from the surroundings the mounting of the sample is important. To achieve an efficient thermal contact of the samples to the cold finger a custom sample

mount has been made consisting of two parts: a piece mounted on the cold finger and individual copper pieces on which the samples are glued using silver glue with a high thermal conductivity. The copper pieces can then be mounted by screws on the cold finger enabling a good thermal contact.

To allow for the precise positioning of the sample with respect to the collection and excitation optics the cryostat is mounted on two translation stages which enables the positioning of the cryostat with a precision of 0.1 μm.

3.2 Excitation

The excitation part of the setup is shown in figure 3.1. The source of the excitation light is a Coherent Mira 900 mode-locked Ti:Sapphire laser which is pumped by a 5 W frequency doubled YAG laser (Coherent Verdi). The laser can either be operated in femto- or picosecond mode but due to the large spectral width in femtosecond mode the laser is used in picosecond mode where the pulse length is ~ 2 ps giving a spectral width of ~ 0.5 nm. The pulse length in picosecond mode is much smaller than the time-resolution of the detectors used and will not limit the time-resolution of the setup.

The optics in the excitation part of the setup is mainly used for controlling the excitation power and polarization. The light from the laser is first sent through two sets of polarizing beam splitters with a quarter wave plate in front. These are used to control the intensity together with a set of neutral density (ND) filters. After these a half wave plate and a quarter wave plate is placed to allow the control of the polarization of the excitation light.

In addition there is a delay line used for the photon indistinguishability measurements. This evenly splits the light on the first beam splitter and delays one part before combining the two beams on the second beam splitter. When the laser is mode-locked this results in two excitation pulses separated by approximately 2 ns. This is further described in relation to the photon indistinguishability measurements in chapter 5.

After the power and polarization control the light passes a lens (L1)

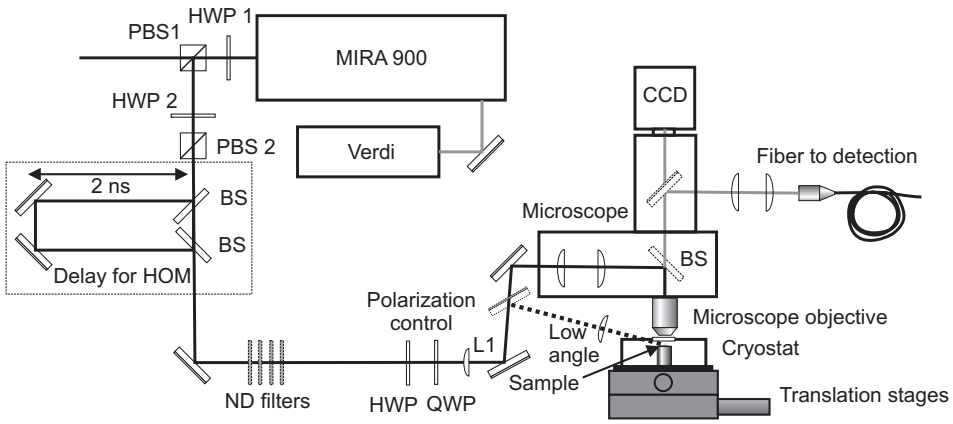

Figure 3.1: A sketch of the excitation part of the setup along with the microscope and the cryostat mounted on the translation stages.

before entering the microscope to be focussed on the sample by a microscope objective. This lens together with the lenses in the microscope ensures than the beam is collimated and that the beam waist of the laser matches the aperture of the microscope objective.

3.3 Microscope

To collect the light emitted by the sample a microscope is mounted above the cryostat as sketched in figure 3.1. The microscope is an Olympus BXFM system customized with an input port for the laser and an output port for the fluorescence. The microscope used enables easy switching between viewing of the sample and measuring fluorescence. It also offers good control of the focus, good stability and makes it easy to switch between objectives.

The illumination of the sample can be switched between a built-in halogen lamp or the excitation light from the laser. The light is reflected through the microscope objective and onto the sample by a beam splitter cube.

The light emitted from the sample is then collected by the objective transmitted through the beam splitter and either sent to a camera or to the detection part of the setup though a polarization maintaining single mode fiber[1]. A beam expander is added before the fiber to match the output mode of the objective to the mode of the input coupler on the fiber. The fiber also acts as a confocal pinhole as the light collected from the sample is imaged onto the tip of the single mode fiber with a diameter of 6.1 μm. By matching the magnification of the objective and the fiber coupling lens using the beam expander a collection area on the sample can be reached matching the optical resolution of the microscope objective.

Two beam splitter cubes are used in the microscope one reflects $\sim 10\%$ and transmits $\sim 90\%$ in a broad wavelength range and is primarily used when viewing the sample using the halogen light. The other has a dichroic mirror mounted which reflects light from 650 nm to ~ 860 nm and transmits light from 900 nm. This is used to effectively separate the excitation light scattered from the sample and the emitted fluorescence. The transmission of the dichroic mirror is between 95% and 99% from 900 nm to 1200 nm. After the dichroic mirror a long pass filter with a cut off wavelength of 850 nm is also mounted to further suppress the excitation light. This cube is used when doing photoluminescence with excitation above the GaAs band gap or in the wetting layer.

3.3.1 Microscope objectives

The microscope objective is an important part of the setup and to achieve a high collection efficiency and resolution it should have as high a numerical aperture (NA) as possible. It should also have a good transmission in the emission range of the quantum dots from 800 nm to 1050 nm. In addition the working distance should be large enough to focus through the window and onto the sample. An important limitation of the optical access to the sample in the cryostat is the window. When using a high NA objective this results is a significant change of the focal distance at different angles similar

[1] Schäfter + Kirchhoff (PMC-980/1060-6.1-NA012-3-APC-500-P) and coupling lens (60FC-4-A18-02).

to a spherical abberation [55]. Ideally the objective should also be able to correct for this.

Two objectives have been used in the setup. The first is a 100X objective from Olympus[2] optimized for near infrared applications with a NA of 0.8. From the specifications the transmission of the 100X objective from 800 nm to 1000 nm is $\sim 80\%$, which has been verified by measurements. The other objective is a 40X objective from Nikon[3]. This objective has a lower NA of 0.6 and is not optimized for near infrared wavelengths. In return is can compensate for the abberation of the cryostat window. The transmission of the 40X objective was measured at 800 nm to 950 nm and a transmission of $77 \pm 1\%$ was found in this range.

The spot size of the laser has been measured for the two objectives and a diameter (FWHM) of 1.4 μm if found for the 100X objective and 2.4 μm for the 40X objective.

The optical resolution of the setup should be very close to the spot size of the laser. This can be measured by imaging a point source. Single quantum dots can be used as such point sources and the resolution can be found by moving the sample and measuring the fluorescence spectra as function of the position. The intensity at a specific wavelength can then be plotted and the resolution found. This has been done using an unprocessed quantum dot sample and is shown for the 40X objective in figure 3.2 where a resolution of 2.1 ± 0.3 μm was found. This figure also illustrates that individual quantum dot emission lines can be isolated by the spectral and positional resolution of the setup. The resolution has also been measured using small test structures and consistent values was found. Similarly for the 100X objective a resolution of 1.4 ± 0.2 μm was measured.

This shows that the 100X objective should be preferred for high resolution measurements and due to the higher NA the collection efficiency should also be higher. However, the large NA and the lack of correction for the cryostat window will limit the coupling efficiency to the fiber due to the resulting optical abberations. To compare the total collection effi-

[2]LMPL 100XIR

[3]CFI Super Plan Fluor ELWD 40XC

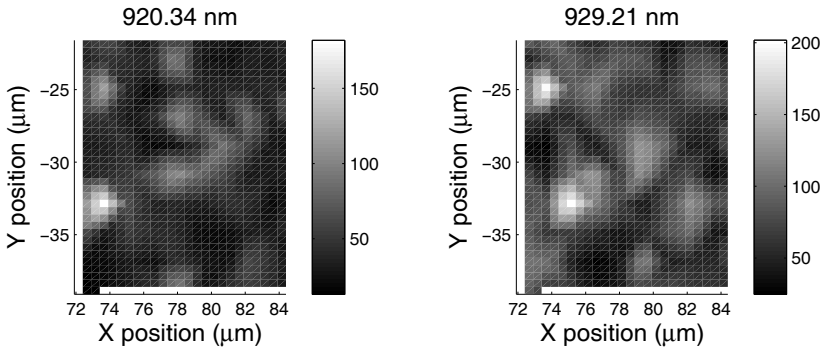

Figure 3.2: Photoluminescence intensity as a function of position for a bulk quantum dot sample at different wavelengths. The intensity given by the color bars are counts on the CCD.

ciency of the two objectives the photoluminescence intensity of quantum dots in a bulk material was measured as a function of pump power for both objectives. From these measurements the measured intensity at the saturation power of the two objective was found and the collection efficiency of the 40X objective was found to be a factor of 2.2 ± 0.1 higher than the 100X objective. This will be different for different nanostructures with more complicated emission patterns but shows the importance of the cover glass correction for high NA objectives and that the 40X objective is preferable unless the higher spatial resolution of the 100X objective is needed.

3.3.2 Coupling efficiency of the fiber

The maximum value of the coupling into the single mode fiber is given by the manufacturer to be 80%. This is, however, for a perfect Gaussian mode and not for confocal imaging. In this case a theoretical value for perfect optics of 51% has been calculated [56].

To find the coupling efficiency to the fiber different approaches has been used one is to use diffuse scattered laser light where a transmission of 42%

was found at 960 nm. The transmission of the fiber has also been measured using photoluminescence of quantum dots. The fluorescence signal was measured with the light through the fiber and by with the light bypassing the fiber using free space optics. The difference in signal was found to be $46\% \pm 5\%$ in the measured range of $900 - 950$ nm.

This shows that using the fiber is associated with a significant loss, however the fiber has some important advantages as discussed below.

3.3.3 Low angle excitation

Instead of exciting the sample from above through the microscope objective there has also been added an option for excitation of the sample at a low angle of 15° past the objective. This is shown by the doted line in figure 3.1.

The light cannot be focussed as tight as with the microscope objective due to the long distance to the sample and lack of space. The light is focussed by a lens with a focal length of 85 mm to a spot size of 8 μm. Due to the angle to the substrate the spot is elliptical with the long axis given by $8\ \mu\text{m}/\sin(15°) = 31\ \mu\text{m}$. This setup is especially useful when exciting quantum dots in the p-shell where the separation of the excitation light from the detected fluorescence is more difficult with filters due to the small difference in wavelength.

3.4 Detection

When the photons have been collected and coupled to the fiber they are sent to the detection part of the setup shown in figure 3.3. Depending of the type of measurement to be done the output position of the fiber is selected among the following options

- Time-resolved spectroscopy
- Hanbury-Brown and Twiss correlations
- Hong-Ou-Mandel interferometry

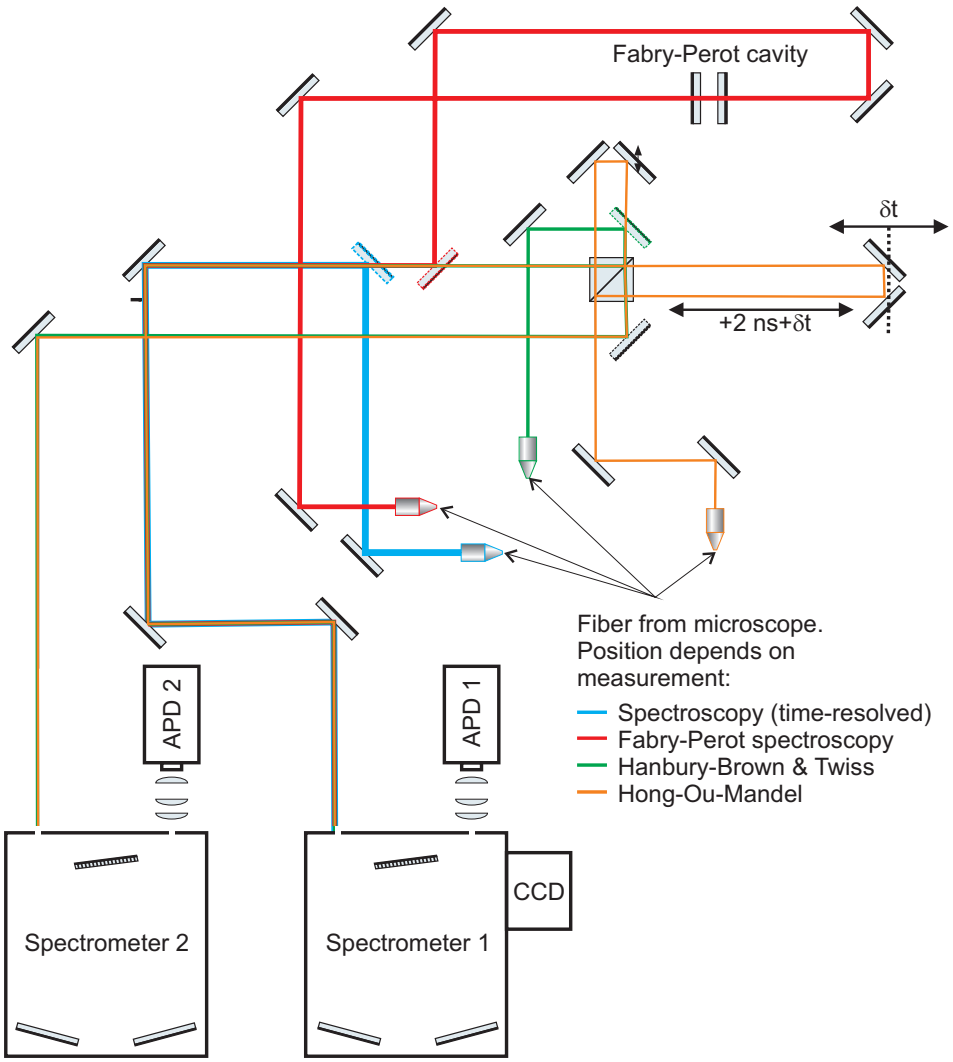

Figure 3.3: A schematic drawing of the detection part of the setup. Depending on the measurement the output of the fiber can be positioned in one of four positions and the different beam paths are illustrated by the colors.

- Fabry-Perot spectroscopy

The beam paths of the different options are illustrated by the different colors in figure 3.3. The switching between experiments makes it easy to do different measurements on the same sample without changing anything in the collection or excitation part of the setup thereby making sure that the excitation and detection conditions of the sample are unchanged.

The fiber also ensures that the mode into the detection part of the setup is always the same and the alignment of the collection and detection part of the setup are independent.

A narrow linewidth grating feedback diode laser emitting at 970 nm is installed such that it can be coupled to the input of the fiber instead of the signal from the microscope. This enables easy alignment of the detection optics and is crucial for the alignment of the Hong-Ou-Mandel interferometer and the Fabry-Perot cavity.

For all the experiments the photons are sent to one or both of the spectrometers shown in figure 3.3 where they are detected by a CCD or single-photon detectors. The spectrometers are similar 0.67 m grating spectrometers where different gratings can be installed depending on the desired resolution. The options used here are either a 1200 g/mm or 600 g/mm. A resolution of 0.04 nm can be reached with the 1200 g/mm grating, however the transmission of the 600 g/mm grating is larger and for most measurements this is used.

Total transmission from the output of the fiber to the detectors depends on the grating used. For the 600 g/mm this has been measured using the alignment laser at 977 nm to be 38% but for the 1200 g/mm grating this is only 18%. This means that the high resolution grating should only be used when the factor of two in resolution is important.

The output of spectrometer 1 can either be directed to a CCD for measuring spectra of to a single photon detector for time-resolved measurements. The single-photon detectors used are silicon avalanche photodiodes (APDs) integrated in single-photon counting modules. An APD with both high sensitivity, low noise and good time-resolution is not available and for this reason two different types are used in the experiments. The first type

is from Perkin Elmer[4] (PE) which is the most sensitive but has a large time-jitter of 280 ps increasing with higher count rates. The quantum efficiency is 34% at 900 nm and 14% at 1000 nm with a the dark count rate of $\sim 80\ s^{-1}$. The other type of APD used is from Micro Photon Devices[5] (MPD) which has a much better time-resolution with a time-jitter of 50 ps but the quantum efficiency is also a factor of 5 lower. The two types thereby complements each other and they are used depending on whether time-resolution or sensitivity is most important.

For high resolution spectroscopy the grating spectrometer can also be combined with a Fabry-Perot cavity as shown in figure 3.3. This makes it possible to measure the linewidth of individual quantum dot lines with a spectral resolution of 1.5 GHz matching the homogenous linewidth of the quantum dots. No measurements using Fabry-Perot spectroscopy is presented here but is included for completeness.

3.4.1 Time correlated single-photon counting

The principle used in the time-resolved photoluminescence measurements is called time correlated single photon counting (TCSPC) and relies on fast single-photon detectors and electronics to measure the time-difference between the excitation of the sample and the detection of an emitted photon. The TCSPC electronics used is a PicoHarp 300, which can measure the arrival time of two independent channels with a resolution of 4 ps. For time-resolved measurements a fast photodiode is used to get a trigger signal from the laser which is used in one channel and the APD is connected to the other. When a photon is detected on the APD the TCSPC electronics then calculates the time-difference between the last excitation pulse and the photon arrival time and builds up a histogram of the time differences. In this way a decay curve is measured. For low count rates this is a very effective technique to measure decay curves with a high signal to noise ratio.

[4] SPCM-CD3226
[5] PDM-50CT

3.4.2 Hanbury-Brown and Twiss setup

A described in section 2.4 a beam splitter and two detectors are needed to measure the HBT signal. This is implemented in the setup by sending the light onto a beam splitter and then directing each of the outputs into separate spectrometers where the photon arrival time are detected by the APDs at the outputs. This is illustrated in figure 3.3 by the green beam path.

For HBT measurements the two individual spectrometers are adjusted to the same detection wavelength and bandwith. The output of the APDs are feed to the TCSPC electronics and the arrival time of the photons are recorded from which the time correlation can then be calculated.

The use of two spectrometers also enables the setup to measure correlations between different wavelength which can be used to investigate whether different emission lines are originating from the same emitter [57, 13, 58].

3.4.3 Hong-Ou-Mandel interferometer

The indistinguishability of the photons emitted by the micropillar is measured using a Hong-Ou-Mandel interferometer [53].The beam path of the interferometer is shown in figure 3.3 by the orange lines. The principle is to use the same beam splitter to split two photons generated by a single photon source and to combine then again. The two photons exiting the fiber is split on the lower left corner of the beam splitter and sent to a short and a long arm of the interferometer the difference in distance of the arms are set by the time difference of the photons as will be described in chapter 5. The long arm can be moved along a track to change the delay of the interferometer. The position of the recombination of the light from the two arm are the same as for the HBT setup and the light goes into the same beam paths and into the spectrometers.

The interferometer is roughly aligned with the help of a CCD camera in one of the output arms. This can be used with the alignment laser to overlap the two beam from the different arms and the shape of the interference fringes on the camera makes it possible to align the interferometer precisely.

The visibility of the interferometer is then optimized and measured using the alignment laser and a piezo electric element mounted on one of the mirrors of the short arm. This can move the mirror a few μm to measure the interference fringes of the interferometer on a photodiode in one of the output arms. As the alignment laser is sent though the single mode fiber this ensures that the interferometer is aligned to the mode of the detected fluorescence. In this way the visibility of the interferometer can easily be measured when the interferometer delay is changed without interfering with the alignment of the detection optics. A visibility of up to 95% can be achieved.

Chapter 4

Coupling of quantum dots to micropillar cavities

In this chapter measurements of the coupling of quantum dots to a micropillar cavity is presented. The coupling is investigated from the photoluminescence spectra and time-resolved photoluminescence measurements. From these measurements the decay rate as a function of the detuning of the quantum dot from the cavity resonance is investigated. A strong enhancement of the quantum dot decay rate at resonance is seen and this Purcell effect is found to decrease with detuning following the cavity linewidth. In contrast, pronounced emission is observed in the cavity emission spectrum even for detunings much larger than the cavity linewidth.

Decay rates of quantum dots on resonance with a cavity are always found in the literature to be much smaller than the theoretical decay rates using simple models. In this chapter the measured data are in detail compared to the model described in chapter 2 to see if they can be consistently described by the model. This also makes it possible to set limitations on important parameters of quantum dots in micropillar cavities such as the dephasing rate and non-radiative decay rates.

4.1 Micropillar cavities

To achieve an efficient single-photon source the emission from the single-photon emitter can be enhanced by enhancing the emission into a single mode and one solution is to use a nanocavity. To reach an efficient coupling a cavity with a small mode volume and low loss is needed as discussed in section 2.2.1. To reach a small volume comparable to the wavelength of the emitter cubed, a cavity with a mode volume of $\sim (\lambda/n)^3$ is needed. In the case of InAs quantum dot emitters this results in a mode volume below 1 μm^3. A lot of work has been done to fabricate such microcavities in the last 20 years and there are basically two principles that can be used alone or in combination to achieve this. One is total internal reflection which is the principle behind the guiding in optical fibers and the other is based on distributed Bragg mirrors (DBRs). Structures based on total internal reflection, where high Q factors and small mode volumes have been achieved includes microspheres [59, 60, 61], microtoroids [62], microdiscs [63, 46], and recently also using metal microdiscs where the cavity mode is a surface-plasmon-polariton whispering gallery mode [64]. In all of the mentioned dielectric structures the strong coupling regime has been reached.

The other solution of creating confinement for high Q and low volume microcavities is based on distributed Bragg reflection or photonic crystals described in section 2.2.2. This can either be used in one, two or three dimensions. In 1D this corresponds to adding Bragg mirrors above and below a cavity. To reach the lowest possible mode volume a $\lambda/2$ cavity should be used, however, in this case there is no antinode of the field in the cavity and the coupling to the emitter would be weak in such a cavity. To achieve the smallest mode volume with efficient coupling a λ cavity is therefore used [65]. An illustration of the field in a λ cavity with a quantum dot is shown in figure 4.1. The confinement in the two other dimensions can then by achieved by waveguiding. The resulting structure is a micropillar cavity which is the structure investigated in this chapter.

In the more general case of two and three dimensions the distributed Bragg approach result in photonic crystal membranes or full 3D photonic crystals. To create a cavity in these structures a defect is introduced. In pho-

Figure 4.1: Sketch of the electric field of a λ distributed Bragg cavity. The light blue and dark blue regions are the two materials with different refractive index used (eg. AlAs and GaAs). The amplitude of the electric field is shown by the red line and the layer of quantum dots is illustrated with a yellow dot at the center of the cavity where the field is strongest.

tonic crystal membranes this is done by "removing" a number of holes and possibly changing the size and position of the neighboring holes to minimize the mode volume or maximize the Q factor [33]. Large Q factors and small mode volumes have been reached in photonic crystal membrane cavities in GaAs [11, 12, 66, 67] resulting the demonstration of strong coupling with quantum dots [13].

One of the major advantage of using micropillar cavities is the emission pattern. In a photonic crystal cavity the emission is evenly distributed above and below the membrane and the emission pattern can be complex and with a strong emission into large angles requiring very high numerical aperture collection optics. This can to some extend be compensated for by careful design of the cavity [68]. In micropillar cavities the emission leaking from the cavity mode is guided by the pillar and the emission in therefore emitted from the ends. By adding more Bragg layers to the bottom of the pillar compared to the top layers the emission from the cavity resonance will primarily leak through the top mirror and be directed towards the detection optics.

Micropillar cavities have been investigated for the last 20 years starting with the fabrication of vertical surface emitting lasers. For micropillar cavities with embedded quantum dots efficient coupling to the cavity mode [69] and single-photon emission [6, 70, 71] have been demonstrated including the

first demonstration of indistinguishable photons from quantum dots [8].

4.2 Samples

The samples investigated in this thesis are fabricated by our collaborators at the University of Würzburg. The samples are state-of-the-art micropillar cavities with high Q factors. In this section the fabrication process will be briefly sketched. For more information on the fabrication see Löffler et al. [72].

The wafer[1] is grown by molecular beam epitaxy starting with the bottom DBR containing 30 layers of alternating 80 nm AlAs and 75 nm GaAs. Then a layer of GaAs is grown as the lower part of the central λ-cavity and on top of this the quantum dots are grown. These are $In_{0.3}Ga_{0.7}As$ self assembled quantum dots with a low density of $6 - 9 \cdot 10^9$ cm^{-2}. The rest of the GaAs cavity is then grown resulting in a 288 nm cavity length. Finally the top DBR consisting of 26 periods of 81 nm AlAs and 72 nm GaAs layers is grown.

From this wafer micropillars with a diameter from 1 μm to 4 μm are fabricated using electron-beam lithography and reactive ion etching. The result is free standing pillars with a height of ~ 9 μm and smooth surfaces. The pillars are approximately 200 nm thicker than the designed diameter at the position of the cavity. The structure of the pillars are illustrated in figure 4.2 along with a scanning electron micrograph (SEM) of pillar with a diameter of 1 μm. The number of quantum dots in a pillar with a diameter of 3 μm is $\sim$ 200. The pillars are ordered in fields with a 6×6 arrays of micropillars with the same diameter. This redundancy is needed as the random nature of the quantum dot growth will result in only a few samples per field where the emission wavelength of the a quantum dot matches the cavity resonance and is positioned close to the center of the pillar, where the coupling is strongest.

[1] The wafer described is numbered C1188

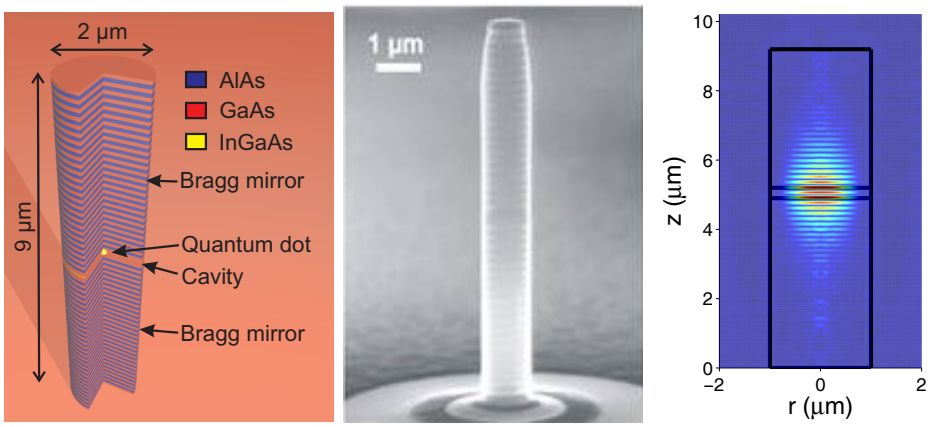

Figure 4.2: Left: Sketch of the micropillars investigated with a cut out to show the inside of the pillar. The drawing is to scale with a diameter of 2 µm and layer thicknesses from SEM characterization. The different materials are colored with GaAs colored red and AlAs blue. The InGaAs quantum dots in the middle of the cavity are illustrated by a single (yellow) dot at the center. In the real samples the quantum dots are randomly distributed in a layer in the middle of the cavity. Middle: A scanning electron micrograph of a micropillar similar to the ones investigated. The layers of the Bragg mirrors are clearly visible and the cavity can also be seen as the wide layer in the center of the pillar. The pillar on the micrograph is $\sim$ 1 µm in diameter. The image is from The University of Würzburg. Right: A simulation of the electric field of a micropillar with a diameter of 2 µm and the same structure as the pillars used in this chapter. From the simulation a mode volume of $V = 0.33$ µm^3 is found. The simulation is done by N. Gregersen and is described in [73].

4.2.1 Choosing a pillar diameter

Several considerations have to be taken into account when selecting an optimal diameter of the micropillars. For single-photon emission a high β-factor is desired and this requires a high Purcell factor, which again requires a small mode volume and a high Q factor.

The mode volume of a micropillar can be approximated from the length of the cavity and the effective mode area (A_{eff}) by $V \sim 2L_c \cdot A_{\text{eff}} = 2L_c\alpha\pi r^2$, where the parameter α is between $\frac{1}{3}$ and $\frac{1}{4}$ [74]. This means that the diameter should be minimized, however, as the primary losses are due to scattering at the surface of the pillar a smaller diameter will also result in a smaller Q factor. This has been investigated for the design of pillars used here and the Q factor is seen to increase rapidly up to a diameter of 2 µm where the optimal ratio between Q and r is also found [75, 72]. To calculate the mode volume and the Q factor exactly numerical calculations must be used [73]. For the DBR and cavity structure used in this chapter and a pillar diameter of 2 µm this has been done by N. Gregersen and the field is shown in figure 4.2. A mode volume of 0.33 $\mu m^3 = 18(\lambda/n)^3$ is found, which results in $\alpha = 0.19$ that is slightly smaller than the range from [74] given above.

Another consideration is that increasing the Q factor by adding layers to the mirrors will result in a Q factor mainly limited by scattering at the sides of the pillar. This will result in the light being emitted from the sides of the pillar and not from the top mirror resulting in a lower collection efficiency. This effect will decrease for an increasing diameter of the micropillar but the mode volume will then decrease and there will be an optimal diameter for the collection efficiency [76].

Furthermore only a single quantum dot should couple to the cavity mode to ensure clean single-photon emission. This requirement favors small cavity diameters to limit the number of quantum dots in the cavity. On the contrary there should not be to few quantum dots as it will be difficult to find one compatible with the cavity resonance wavelength. Another solution to limit the number of dots close to the cavity resonance is to design the cavity to be resonant at the high or low energy part of the inhomogenous broadening of the quantum dots.

From these considerations a diameter was chosen where the ratio between the Q factor and the radius was highest. This resulted in the selection of a designed diameter of 1.8 μm, corresponding to a real diameter of 2 μm at the position of the cavity.

4.3 Photoluminescence measurements

To measure the photoluminescence (PL) from the micropillars the experimental setup described in chapter 3 is used. The samples are mounted in the cryostat such that the low angle excitation (section 3.3.3) can be utilized. Using the angled pump has two main advantages as the pump beam does not have to propagate though the top DBR mirror such that lower a intensity is needed and estimating the actual pump power of the quantum dots is simpler. Another major advantage is that the reflection from the laser is better separated from the detection as no direct reflection is sent into the objective. This is especially important when pumping in the excited states of the quantum dots due to the small difference in excitation and detection wavelength. The data presented in the rest of the chapter are exclusively pumped from the side.

The emission is collected from the top of the pillar by the Nikon microscope objective (NA = 0.6). Only one polarization is detected by sending the collected light through a half-wave plate and a fixed polarizer before coupling it to the detection fiber.

To achieve an optimal signal the precise alignment of the pillars to the detection setup is important. The rough alignment is done using the microscope image on the CCD. An example of a microscope image of a field of micropillars is seen in the insert of figure 4.3. This is also used to avoid broken pillars or pillars with other visible defects. The setup is then switched to PL detection on the spectrometer and the pillar is pumped at 800 nm to get a strong signal on the spectrometer. This signal is then used to fine tune the position of the translation stages and the focus of the microscope.

To locate the cavity resonance and the spectral position of the quantum dots, photoluminescence spectra are taken with continues wave (cw)

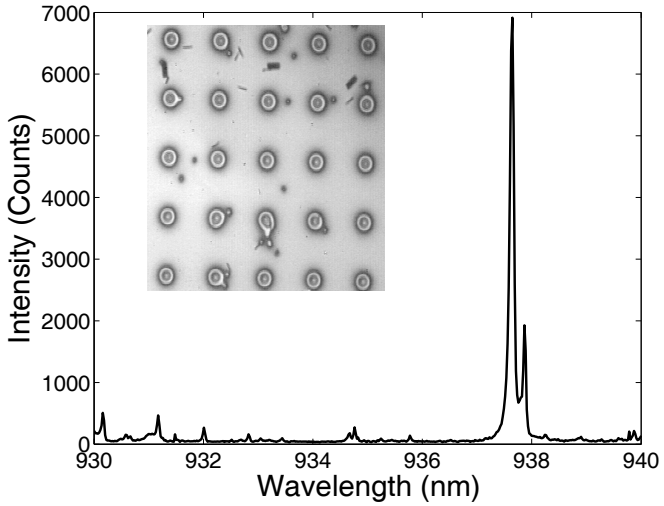

Figure 4.3: Photoluminescence spectrum of a pillar with a diameter of 2.0 μm at 20 K. The pillar is excited using a cw laser at 800 nm. The strong emission at 937.6 nm is from the cavity resonance and a number of quantum dot lines are seen at other wavelengths, most notably the peak at 937.9 nm which is enhanced due to the coupling to the cavity mode. The insert shows an optical microscope image of a field of micropillar cavities with a diameter of 2.0 μm.

excitation using a wavelength of 800 nm and a power above the saturation of the single exciton lines. This excitation wavelength corresponds to an energy above the GaAs band gap which efficiently excites all quantum dots in the pillar. A typical PL spectrum is seen in figure 4.3. The spectrum originates from a micropillar with a diameter of 2 μm and is measured at a temperature of 20 K. When pumping at energies above the GaAs band gap the spectrum is dominated by a strong emission from the cavity resonance. This is seen in the spectrum as the large emission peak at 937.6 nm. Depending on the specific pillar the intensity varies a lot due to the different spectral positions of the quantum dots in the pillar but the cavity peak always dominates the emission even a low excitation powers. The spectrum also shows a number of smaller peaks. These are narrower than the cavity linewidth and limited by the spectrometer resolution which identifies them as originating from quantum dots in the micropillar. A strong emission line just above the cavity resonance is also seen. This is a quantum dot close to resonance which shows enhanced emission compared to the other quantum dots as it couples to the cavity mode. To achieve an efficient coupling such a quantum dot peak close to the cavity resonance is needed. However, to reach the optimal coupling a quantum dot needs to be perfectly at resonance with the cavity. This can be done by changing the temperature of the sample or using electric tuning by the Stark effect [77].

4.3.1 Temperature tuning

To tune the quantum dots into resonance with the cavities temperature tuning is used. Temperature tuning is based on the difference in the change of the refractive index and the band gap of GaAs and InAs as a function of temperature. The resonance frequency of the cavity is determined by the thicknesses and refractive indices of the layers in the micropillar structure while the temperature dependence of the energy levels of the quantum dots are changing due to the change in the band gaps of InAs and GaAs with temperature. As the relative change of the energy levels with temperature are larger than the relative change of the resonance frequency of the cavity it is possible to use the temperature to tune the quantum dots into resonance

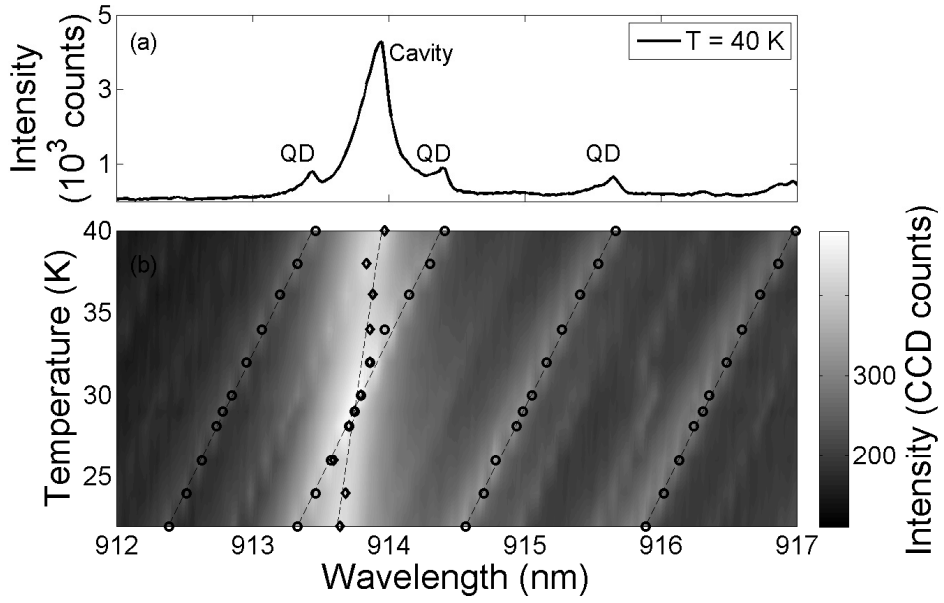

Figure 4.4: (a) Photoluminescence spectrum of a micropillar cavity with a diameter of 2 μm. The excitation is done above the GaAs band gap at 800 nm cw and with an intensity around saturation of the ground state exciton lines. The strong cavity peak and some of the quantum dot peaks are marked. (b) Photoluminescence spectra as a function of sample temperature for the same micropillar and parameters as the spectrum in (a). The quantum dot peaks are marked by circles and the center wavelength as a function of temperature has been fitted by a linear function shown by the black dashed lines. A value of 0.060 ± 0.001 nm/K is found for the quantum dot emission change. The cavity peak is marked by the open squares and the center is fitted to a linear function giving a change of 0.018 nm/K.

with the cavity.

An example of such temperature tuning is shown in figure 4.4. The

top part of the figure shows a PL spectrum of a micropillar taken with cw excitation at 800 nm around the cavity resonance. The spectrum is taken at a sample temperature of 40 K. The cavity is seen to have a resonance around 914 nm and three quantum dot peaks are also seen in the spectrum. The temperature was changed to measure the change in cavity and quantum dot emission wavelength with temperature. The result is plotted in the lower part of figure 4.4. The color shows the intensity on a logarithmic scale to easily see both the quantum dot and cavity peaks. The cavity peak is seen to change little with temperature compared to the quantum dot peaks. It is also seen that one of the quantum dots is tuned though the cavity which enhances the emission from the cavity at the resonance temperature of 30 K. To find the change in resonance frequency with temperature the maximum of the cavity and four quantum dot peaks has been found. These are shown by the black circles in the figure. The positions of the peaks have then been fitted with a linear function to find the wavelength change with temperature. For the cavity peak a value of 0.018 nm/K is found and a value of 0.060 nm/K is found for the quantum dot lines. This gives a relative change of 0.042 nm/K around 30 K which is a relative change of the detuning of only $4.6 \cdot 10^{-5}$ K^{-1} giving a total tuning range of ~ 2 nm for a 50 K temperature range. This shows the limitation of temperature tuning as a sample with a quantum dot close to the cavity resonance is needed. This value is also temperature dependent and gets smaller with lower temperatures [78], making it more difficult to tune quantum dots into resonance at lower temperatures.

4.3.2 Measuring cavity Q factors

The Q factor of the cavity is determined by the width of the cavity resonance. To find the Q factor the width can be measured from photoluminescence spectra of the micropillars, however, care must be taken to measure the right value as the width can be influenced by single dot lines. To measure the correct Q factor from photoluminescence measurements the emitters must ideally be emitting with a flat spectrum in the wavelength range of the cavity. As quantum dots have much narrower lines than the cavity

it is important not to be influenced by these lines. This can be avoided by pumping the quantum dots with a high excitation power resulting in a strong and almost flat emission due to the many lines from biexcitons and higher excited states [79]. To fulfill these requirements the measurement is done by exciting the pillar above the GaAs band gap at 800 nm using a cw laser at approximately 10 times the saturation power of the single exciton lines. An example of such a spectrum is seen in figure 4.5. The spectrum shown is from a micropillar with a diameter of 2.0 μm which is the main pillar under investigation in the rest of the chapter[2].

As the width of the cavity resonance is comparable to the instrument response function (IRF) of the spectrometer the Lorentzian line shape of the cavity resonance must be convoluted with the IRF of the spectrometer to find the cavity linewidth. The data are therefore fitted with a Lorentzian convoluted with the IRF. The result is shown in figure 4.5 where both the IRF (gray dashed line), the convoluted Lorentzian (black dashed line) and the resulting deconvoluted Lorentzian (black solid line) are shown. A small shift of the top of the peak is seen in the convoluted spectrum due to the asymmetry of the IRF. A linewidth (FWHM) of 43.5±0.6 pm corresponding to a Q factor of 21300 ± 300 is found for this pillar. This is a high Q factor for micropillar cavities with quantum dots showing the state-of-the-art quality of the samples [80, 81]. The measured Q factor is consistent with measurements performed on similar pillars in Würzburg and is in general around 2.5 times smaller than the values obtained from simulations of the pillars [3]. The primary reason for this deviation is fabrication tolerances and roughness which is not taken into account in the simulations.

4.3.3 Photoluminescence excitation spectroscopy and excited state excitation

As it is seen in the PL spectra in figure 4.3 and 4.4 strong emission is observed from the cavity peak even when no quantum dot is resonant with

[2] This pillar is from the sample C1188-10-4C, the field E5 and is the pillar at the 6th row, 4th column (v4h6).

[3] From unpublished simulations by N. Gregersen and [73]

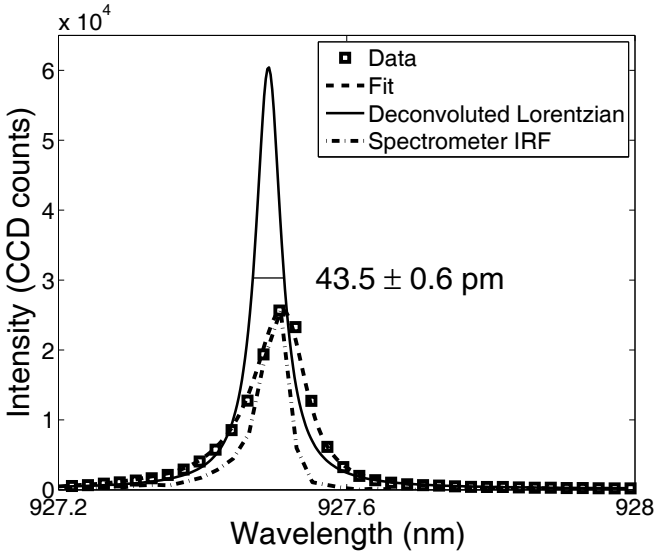

Figure 4.5: Strongly excited spectrum of a micropillar with a diameter of 2.0 μm (red squares). The pillar is excited at 800 nm cw with ~ 10 times the single line saturation intensity. To extract the Q factor of the cavity the spectrum is fitted with a Lorentzian line shape convoluted with the IRF of the spectrometer. The fit is shown by the dashed black line. The dashed gray line shows the IRF of the spectrometer and the solid black line shows the deconvoluted Lorentzian line of the cavity. A full width at half maximum (FWHM) of 43.5 ± 0.6 pm is found corresponding to a Q factor of 21300 ± 300.

the cavity. This indicates that even with a quantum dot on resonance there is also contributions from other quantum dots in the cavity emission. To investigate the coupling of a quantum dot to the cavity it is important only to have a single quantum dot coupled to the cavity as it will be more difficult to interpret the data if the emission is a mixture from many quantum dots. For a single-photon source this is also crucial as multiple quantum dots coupling to the cavity will suppress the single-photon emission.

To attain a cleaner emission from the micropillar the quantum dots can be selectively excited by excitation in the excited states of the quantum dots. In analogy with atomic physics this is also called 'p-shell' excitation. To find the excited state resonances of the quantum dot photoluminescence excitation (PLE) spectroscopy is used. The detection wavelength is kept at a fixed emission frequency, in this case the ground state emission of a quantum dot and the excitation wavelength is varied. In this way the absorption spectrum of the quantum dot is measured. To measure PLE on the micropillars a quantum dot is first tuned into resonance with the cavity using temperature. This is done by PL measurements with excitation above the GaAs band gap. When the resonance temperature is found the excitation wavelength is changed towards the emission wavelength and emission spectra are recorded from which the emission intensity of the quantum dot is extracted. The excitation wavelength is measured on another spectrometer. As the absorption changes the power is adjusted to compensate such that a good signal to noise ratio is conserved in the detected spectra.

An example of a PLE measurement on a micropillar is shown in figure 4.6. When the excitation wavelength reaches the band gap of the GaAs surrounding the quantum dots, marked by the dashed line in the figure, the emission drops as there is no longer absorption from the GaAs surrounding the quantum dot layer. It then stays almost constant until a wavelength of approximately 870 nm where is drops almost two orders of magnitude. This range is where the excitation is absorbed in the wetting layer, which is a quantum well with a continuum of states as discussed in section 2.1. The emission then drops as the excitation energy is below the wetting layer and absorption is possible only directly in the quantum dots. In this range some structure is seen, most notable strong resonances which are narrower than

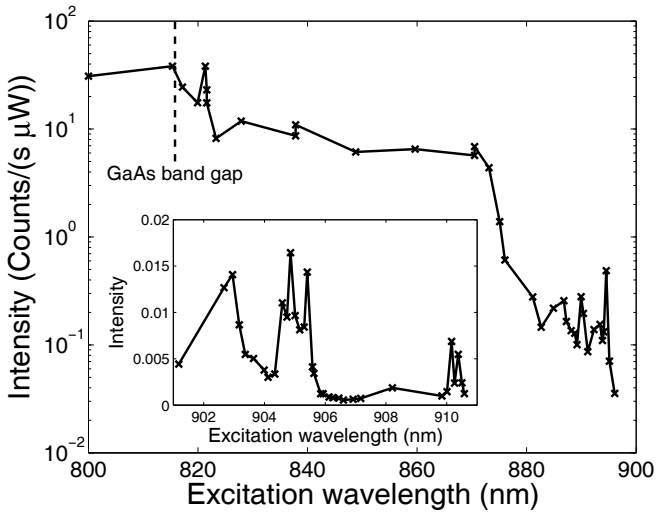

Figure 4.6: Photoluminescence excitation (PLE) spectrum of a quantum dot in a micropillar cavity. The emission is detected at the cavity resonance (927.7 nm). When the absorption decreases the pump power is increased to compensate for the decrease of the PL signal. The insert shows a PLE spectrum of another pillar close to the excited state resonances. The emission for this measurement is at 924.2 nm.

the resolution of the spectrometer used to measure the excitation wavelength (0.3 nm). This is also seen in more detail in the insert measured on another pillar. These resonances correspond to the excited states of the quantum dot (or possibly more dots) and will be used for the excitation of the micropillars. To achieve the 'cleanest' excitation of the quantum dot the lowest strong resonance is used. In the case where there are more quantum dots emitting at the cavity resonance this technique will also ensure that only one of them is excited.

4.3.4 Excitation intensity

To make sure that the emission is from ground state excitons and ensure single-photon emission from the micropillars the ground state of the exciton should not be saturated and it should be confirmed that the emission is from a ground state. Furthermore a high photon count rate is desired which means that the quantum dot should be pumped close to saturation but not above. To find the excitation power to use the emission intensity as a function of the pump power is measured. Such a measurement is shown in figure 4.7.

The figure shows the emission intensity of a pillar pumped using pulsed excitation of the excited state at 909.6 nm. The power on the x-axis is the total power measured before the focusing lens. A black dashed line is added with a slope of one to compare the measured data to the expected linear dependence. The emission is seen to vary linearly for small excitation powers as expected. A saturation is seen around 100 μW and the intensity completely saturates around 2 mW. A simple model of the saturation can be used where the excitation is assumed to be a Poissonian process. At the saturation power (P_s) the mean population is one and the probability of excitation is given by the probability of one or more excitations. The emission is then proportional to the excitation probability, which is then given by $(1 - \exp(-P/P_s))$. For small power this is linear and will saturate around P_s. This model has also been plotted as the red dotted line in figure 4.7 where a saturation power of 500 μW is found to fit the data well.

To calculate the excitation intensity of the quantum dots inside the pillar the transmission of light into the pillar must be found. The intensity

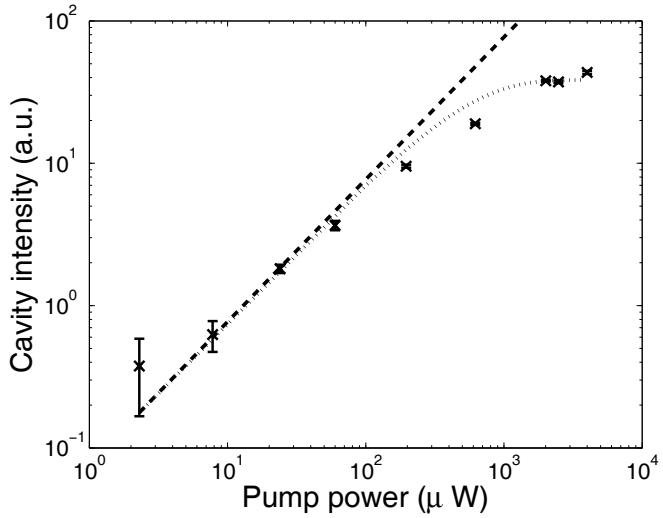

Figure 4.7: Emission intensity as a function of pump power using pulsed laser excitation at 909.6 nm corresponding to the excited state of the pillar. The crosses show the intensity of the cavity peak obtained from CCD spectra as a function of the total pump power into the cryostat. The dashed line has a slope of one to compare the data with a linear power dependence. The dotted line is a linear power dependence with saturation, using a saturation power of 500 μW, as described in the text.

at the center of the excitation spot reaching the sample can be calculated assuming a Gaussian beam with the size of the spot given in section 3.3.3. Taking into account the optics and the reflection from the cryostat window the power reaching the sample is $I_0 = 3.8 \cdot 10^{-3}\ \mu\text{m}^{-2} P_\text{m}$, where P_m is the power measured before the focussing lens. In the limit where the pillar diameter is large compared to the wavelength and the DBRs are neglected the transmission into the pillar can be calculated regarding the pilar as a GaAs interface. In this case the transmission for s-polarized light is 0.68. Taking the angle of the quantum dot plane into account the intensity reaching the quantum dots can then be calculated to be $6.5 \cdot 10^4\ \text{cm}^{-2} P_\text{m}$, where P_m is the measured power of the laser (i.e. the values of the x-axis in figure 4.7). For a power of 500 μW this corresponds to 33 W/cm^2.

Defining the absorption cross section as $\sigma = P/I$, where P is the scattered power and I is the excitation intensity it can be estimated, by assuming that one photon is emitted for every excitation pulse at saturation, as $\sigma = \hbar\omega f_\text{rep}/I$. Using a saturation power (P_m) of 500 μW gives an estimated absorption cross section of $3 \cdot 10^{-12}$ cm^2.

This value is consistent with the value of $1.4 \cdot 10^{-12}$ cm^2 measured by Nakamura et al. [82]. The absorption cross section can also be calculated from the dipole moment as $\sigma = \omega |d|^2/(n\epsilon_0 c\gamma\hbar)$ and for a typical value of the dipole moment of $1 \cdot 10^{-28}$ Cm [23, 24] the calculated absorption cross section would be $3.4 \cdot 10^{-11}$ cm^2. This value is a factor of 10 higher than the measured absorption cross section but the dipole moment used is for the ground state which has been shown to be smaller for the excited states [19].

4.3.5 Photoluminescence spectra of a quantum dot tuned to the cavity mode

The first step in investigating the coupling of the quantum dot to the micropillar cavity is to measure the photoluminescence spectra as a function of detuning. This has been done for the pillar with a diameter of 2.0 μm, where the Q factor and power dependence was measured in section 4.3.2 and 4.3.4 above. The pillar is pumped by pulsed excitation in the excited

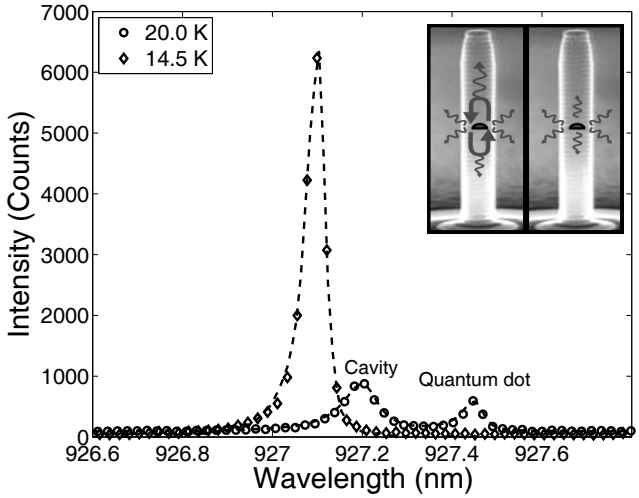

Figure 4.8: Spectrum of the micropillar emission with the QD off resonance with a detuning $\Delta = 0.22$ nm (20 K) and the QD on resonance (14.5 K). The QD is pumped in the excited state (909 nm) with a total power of 500 μW into the cryostat. The right inset displays a SEM picture of a micropillar where the coupling of the QD on (left) and off (right) resonance is illustrated.

state of the quantum dot with a power of 500 μW before the cryostat. The resulting spectra at two different temperatures are shown in figure 4.8.

Figure 4.8 shows two selected spectra, where the quantum dot is non-resonant at 20 K and resonant at 14.5 K. When the dot is non-resonant two lines are observed: one originating from the cavity resonance and one from the quantum dot. One way to distinguish the two are from the linewidth of the peaks. These have been found for the two spectra by fitting a Lorentzian function to the peaks taking into account the spectrometer IRF, as described in section 4.3.2. For the off resonant spectrum at 20 K the cavity peak is found to have a width corresponding to a Q factor of $1.8 \cdot 10^4 \pm 0.4 \cdot 10^4$. This is compatible with the Q factor measured in section 4.3.2 above, however,

one should be careful to use this as the real Q factor of the cavity as it is pumped at a low intensity where the emission is dominated by single dot lines [79]. The width of the quantum dot peak is limited by the resolution of the spectrometer, which is also the case for the peak for the peak os the on resonant spectrum. This illustrates the problem of using low excitation PL spectra for determining the cavity Q factor as the width of the on resonance peak is determined by the linewidth of the emitted and not the cavity.

When changing the temperature the lines are easily distinguished by their change in wavelength. This is seen in the left part of figure 4.9, where a series of spectra are shown from 20 K to 4.5 K. These spectra have been scaled to unity at the highest intensity in the spectra. At high temperatures the quantum dot peak is seen to change linearly with temperature, as discussed in section 4.3.1, before crossing the cavity resonance at 14.5 K. At low temperatures the energy change diminishes, which is due to the low temperature behavior of the GaAs and InAs band gaps [78]. As the quantum dot can be tuned through the resonance and a strong increase in the emission is observed on resonance this sample is suitable to study the coupling as a function of detuning. From the spectra the dependence of the detuning on the temperature is also extracted. The resulting temperature dependence of the detuning is seen in the right part of figure 4.9. For small detunings the resolution of the spectrometer is not high enough to distinguish the peaks and the detuning cannot be found. In this range between 12 K and 15.5 K the detuning is found by fitting a parabola to the data points and using this fit to find the detuning for the temperatures around resonance. The fit is shown by the black line and the interpolation range is indicated in the right part of figure 4.9 by the red lines which also indicates the error of the fitted value in that range.

The unscaled spectra in figure 4.8 shows that when the quantum dot is tuned into resonance at 14.5 K the emission from the pillar is strongly enhanced by a factor of 11. This increase is due to the channeling of photons into the cavity mode due to the increase in the β-factor as a result of the Purcell effect as described in section 2.2.3. In addition the DBR mirrors blocks the off resonant emission which enhances the effect. This is further illustrated in the left inset of figure 4.8: Off resonance, the quantum dot

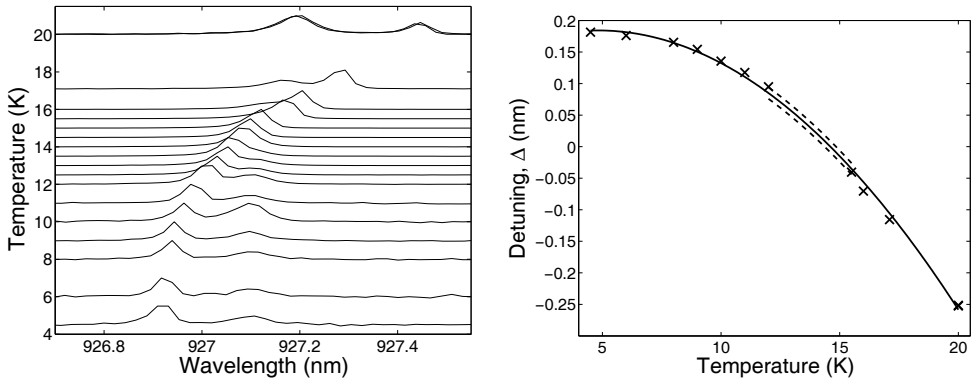

Figure 4.9: Left: The complete series of photoluminescence spectra as a function of temperature from 20 K to 4.5 K. The spectra have been scaled to unity at the maximum intensity. The spectra at 20 K and 14.5 K are the scaled spectra from figure 4.8. Right: Detuning of the quantum dot from the cavity mode as a function of temperature. The data points marked by the crosses are found from the spectra in the left part of the figure by fitting the two peaks to Lorentzian functions and using the center of these fits. The solid line shows the fitted parabola used for interpolating the temperature dependence of the detuning in the range around $\Delta = 0$, where the peaks cannot be distinguished. In this range the thin dashed lines indicate the error of the interpolation which is extracted from the fit.

primarily couples to leaky radiation modes, while on resonance the photon is efficiently channeled into the cavity mode and outcoupled through the top mirror. Due to the influence of the leaky radiation modes and the DBR the Purcell enhancement cannot be measured from the spectra. Determining the Purcell enhancement requires time-resolved measurements to be discussed below.

An interesting thing to notice in the detuned spectrum is the observed pronounced emission at the cavity resonance even though the quantum dot is several cavity linewidths away from resonance. This effect has been observed already in both micropillar cavities [44, 83] and photonic crystal cavities [13, 58], however, only in the latter case a Purcell effect ranging beyond the cavity linewidth was observed in the case of non-resonant excitation of the quantum dots [13, 84].

There have been several recent theoretical investigations of the influence of dephasing on the emission spectra of two-level system coupled to a cavity using different approaches but similar models as the one discussed in section 2.3. The investigations has mostly been focussed on the strong coupling regime [47, 85, 86]. A comparison with the the spectra will be done in section 4.4.2 below using parameters found from the time-resolved measurements of the next section.

4.4 Time-resolved measurements

To determine the coupling of the quantum dot to the cavity time-resolved measurements have been done as a function of the detuning. Examples of measured decay curves on resonance and off resonance are displayed in figure 4.10. A pronounced increase in the decay rate is readily observed when tuning the quantum dot into resonance. The decay rates are extracted by modeling the decay with a double exponential model, which is known to be a good model for self assembled quantum dots [23]. The fast decay rate is primarily investigated here, which stems from the recombination of bright excitons. The decay rates are then found by fitting the model convoluted with the temporal instrument response function (IRF, also shown in the

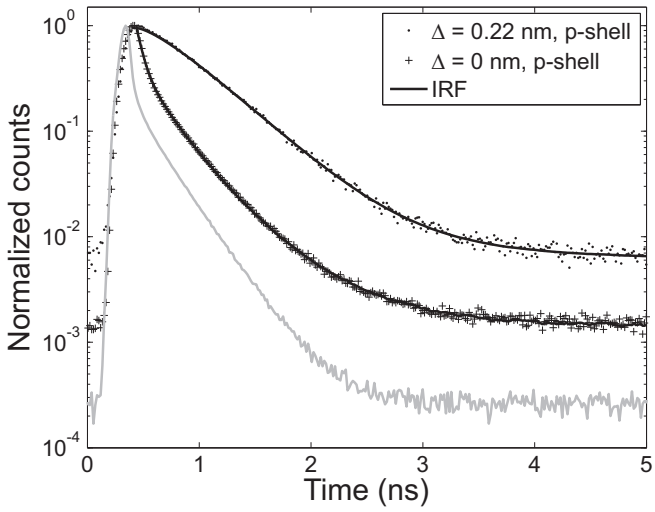

Figure 4.10: Measured decay curves of the quantum dot off resonance using p-shell excitation at 20 K (Δ = 0.22 nm) and on resonance at 14.5 K (Δ = 0 nm). Black lines are bi-exponential fits to the decay curves. Also shown is the instrument response function (IRF).

figure) to the decay curves, starting at the top of the curve. These fits are shown as the black lines in figure 4.10. The model fit the data well for all times of the decay curve and a value of 2.3 ns^{-1} is found off resonance which increase by a factor of 10 to 22.3 ns^{-1} on resonance.

In order to observe decay curves that are easily interpretable it is essential to probe a single quantum dot. This is assured by the p-shell excitation, where an exciton is generated directly in the excited state. If the quantum dots are pumped above the GaAs band gap or in the wetting layer, which is the case for many experiments in the literature [44, 13], several quantum dots are excited and can couple to the cavity. The effect on the decay curves for non-resonant pumping will be discussed further in section 4.5 below.

To prove that p-shell excitation ensures that the cavity emission origi-

nates primarily from a single quantum dot, we have carried out pulsed autocorrelation measurements for the quantum dot tuned to resonance. This is done using the Hanbury-Brown and Twiss setup described in section 3.4.2. A value of $g^{(2)}(0) = 0.17$ is found on resonance which shows that the emission is primarily from a single quantum dot but with a small multi-photon contribution. The single-photon emission of the micropillar is discussed in detail in chapter 5. One important contribution to residual multi-photon emission is dark excitons recombining radiatively after an induced exciton spin-flip [19] but background emission from other quantum dots which are weakly pumped by the tails of the pump laser spectrum may also contribute.

4.4.1 Detuning dependence of the decay rate

The decay curves have been measured for a range of temperatures from 26 K to 4.5 K at both the emission wavelength of the quantum dot and the cavity. The resulting decay curves are fitted with a double exponential model as described above. The fast decay rate as a function of detuning is displayed in figure 4.11. Both the decay rate of the quantum dot and the cavity are shown with the exception of small detunings where the cavity and quantum dot peaks cannot be distinguished.

Pronounced enhancement of the quantum dot decay rate in a narrow peak around resonance is observed with the fastest measured decay rate being 22.30 ns^{-1}, and a leveling off at 2.4 ns^{-1} for large negative detunings (high temperatures) and 2.2 ns^{-1} at positive detunings (small temperatures). This corresponds to an enhancement factor of 9.3 and 10.1. This is a large value in micropillars compared to the literature where a factor of 5-7 has been measured directly from the decay rate [8], however Purcell factors up to 11.4 have been measured in photonic crystal cavities [66]. It is also observe from figure 4.11 that the cavity decay rate agrees very well with the quantum dot decay rate, which confirms that the cavity emission originates from the quantum dot and furthermore that temporal delays due to propagation in the cavity are negligible.

The slow decay rates of the double exponential fits do not depend on the detuning and have a value of 1.7 ± 0.3 ns^{-1} indicating that there is a

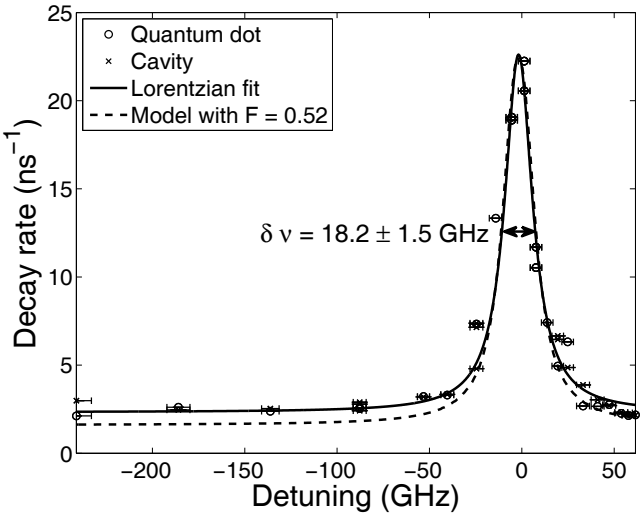

Figure 4.11: The fast decay rate of the quantum dot and cavity peaks as a function of the quantum dot detuning from the cavity resonance. The detuning is given in frequency for easy comparison with theory. The maximum measured decay rate is 22.3 ns^{-1} which is from the decay curve in figure 4.10. The measured decay rates have been fitted with a Lorentzian function (solid line). The width (FWHM) of the fitted Lorentzian is 18.2 ± 1.5 GHz, the decay rate on resonance is 22.9 ns^{-1} and the decay rate far from resonance is 2.26 ns^{-1}. The dashed line shows a calculated decay rate with a quantum dot dipole overlap with the cavity mode (F_d) of 0.52. This value has been fitted as described in the text.

background emission from other quantum dots into the cavity as this decay rate is consistent with the decay rate of the quantum dots in a homogenous medium. The contribution of the slow decay component is $6\% \pm 3\%$ on resonance which is consistent with the HBT measurement in section 4.4 that corresponds to a contribution of 8% using the model in section 2.4.1.

The coupling of a quantum dot to the cavity mode is determined by a number of factors as discussed in section 2.3. For comparison with the theoretical models discussed, these parameters must be extracted from the experimental values. Starting with the cavity decay rate which is found from the Q factor by $\kappa = \omega_c/Q$, and using the Q factor of $21.3 \cdot 10^3$ found in section 4.3.2 above, the cavity decay rate is $\kappa = 95$ GHz. The quantum dot decay rate in a homogenous medium (γ) is found from bulk material to be[4] 1.6 ns^{-1}. The coupling constant g is found from the definition in chapter 2 eq. 2.23 and 2.2:

$$g = \frac{1}{\hbar} E_0 \boldsymbol{d} \cdot \boldsymbol{f}(\boldsymbol{r}) = \sqrt{\frac{\omega_0}{\hbar 2 n^2 \epsilon_0 V} |d|^2} \times \sqrt{\frac{V_{\text{real}}}{V_{\text{theory}}}} \frac{|\boldsymbol{d} \cdot \boldsymbol{f}(\boldsymbol{r})|}{|d|} = g_{\max} \times F_d, \quad (4.1)$$

where F_d is the overlap between the quantum dot dipole and the cavity mode ($|\boldsymbol{d} \cdot \boldsymbol{f}(\boldsymbol{r})|/|d|$) multiplied by the factor stemming from the ratio of the real mode volume (V_{real}) to the calculated mode volume (V_{theory}). This discrepancy is introduced as the measured and calculated Q factors of the micropillar cavities are different indicating that the mode volume is also larger. The position of the quantum dot parallel to the pillar is well known, however, the lateral position in the pillar is unknown along with the discrepancy between the calculated and real mode volume. This means that the parameter F_d not known. The maximum achievable coupling constant with a perfect overlap of dipole with the cavity mode and no discrepancy between the real and calculated mode volume is given by $g_{\max}$. This can now be calculated using the mode volume of 0.33 μm^3 from the numerical calculations described above, a refractive index of GaAs at ~ 900 nm and ~ 10 K of 3.45 [87], and a dipole moment of $1.15 \cdot 10^{-28}$ Cm corresponding

[4] From measurements done by S. Reitzenstein at the University of Würzburg.

to a decay rate in a homogenous medium of 1.6 ns^{-1}. Using these values g_{max} is found to be 68 GHz.

These parameters show that for a quantum dot with $F = 1$ the system should be in the the strong coupling regime since $4g/\kappa = 2.8$, however, no evidence of this is seen in the on resonant spectrum of figure 4.8, which suggests that the quantum dot is not optimally coupled to the cavity mode or a large dephasing is present that reduces the coupling.

The simplest model to compare the measured decay rates to is the Purcell expression of eq. 2.16 even though this is only valid in the weak coupling regime. In this model the decay rate is determined by the cavity Q factor, the mode volume of the cavity and the decay rate in a homogenous medium. The model gives a Lorentzian line shape with a height given by the Purcell expression (eq. 2.17). To compare the measurement to this model the data are fitted to the Lorentzian model where there is accounted for the decay of the quantum dot into leaky modes with a rate γ and through non-radiative recombination with a rate γ_{nr}. Both contributions are assumed to be independent of the detuning (Δ). The fit to this model is shown as the black line in figure 4.11 and the parameter found are a decay rate off resonance $\gamma + \gamma_{nr} = 2.26$ ns^{-1}, a height of 20.6 ns^{-1} and a width corresponding to a Q factor of 17800 ± 1400. The decay rate off resonance ($\gamma + \gamma_{nr}$) could either be due to a large homogenous decay rate of the quantum dot or it could be due to the non-radiate decay rate of the quantum dot. In the case where the radiative decay rate in the pillar off resonant with the cavity is the same as in a homogenous medium the non-radiative decay-rate would be 0.66 ns^{-1}, which is large compared to values in bulk material. In micropillars the decay off-resonance has been shown in calculations to be suppressed by a factor of 0.8 [65] which would give an even higher non-radiative decay rate of 0.98 ns^{-1}. The large non-radiative decay rate could be caused by a close proximity of the quantum dot to the surface of the pillar that has been shown to result in a significant non-radiative decay rate [23]. This also has influence on the measured Purcell enhancement on resonance as this is either 9.1 or 12.9 depending on the value of γ used. With an overlap of 1 the Purcell expression yields a Purcell factor of 95.2, however as the weak coupling approximation is not fulfilled this model is not expected to be con-

sistent with the data and a comparison with the full density matrix model of section 2.3 should be made. It can also be seen that the width of the fitted Lorentzian is broader than expected for the measured Q factor. The width of the resonance is however not much broader as it has been seen in the case of non-resonantly pumped photonic-crystal cavities, where Purcell enhancement was found to range many cavity linewidths [13, 84], which was suggested to originate from charging of quantum dots with multiple holes [58].

To better describe the measured data they are compared to the density matrix model which also includes dephasing. The unknown parameters of the model is the parameter F and the dephasing. The model has been calculated using three different values of the dephasing rate: no dephasing, a temperature dependent dephasing rate of 0.5 μeV/K, and 2 μeV/K to cover the range of measured values of quantum dots in bulk material (see section 2.1.3). If the dephasing rate of the quantum dot in the micropillar is significantly larger than in bulk the model calculated should then be inconsistent with the data. F has then been fitted to get the maximum measured decay rate on resonance as found by the Lorentzian fit. The rest of the parameters of the model used is the ones described above without a non-radiative decay rate. The resulting detuning dependent decay rates are seen in figure 4.12 along with the measured decay rates of the quantum dot line from figure 4.11.

The two calculations with no dephasing and a dephasing rate of 0.5 μeV/K are both consistent with the data. The large dephasing rate of 2 μeV/K gives a broader detuning dependence and is only consistent with half of the data points. This sets a limit on the dephasing rate and shows that the dephasing rate is not considerable larger in the micropillar than in bulk. This shows that measuring the decay rate as a function of detuning can be used set limits on the dephasing rate of the emitter. The model also shows that the width of the data are now consistent with the Q factor as the peak is broadening by the suppression of the decay rate on resonance due to the system being close to the strong coupling limit. For the off resonant values the model is seen to be below the data points for large negative detunings but a good agreement is seen for the positive detunings. This shows that there is

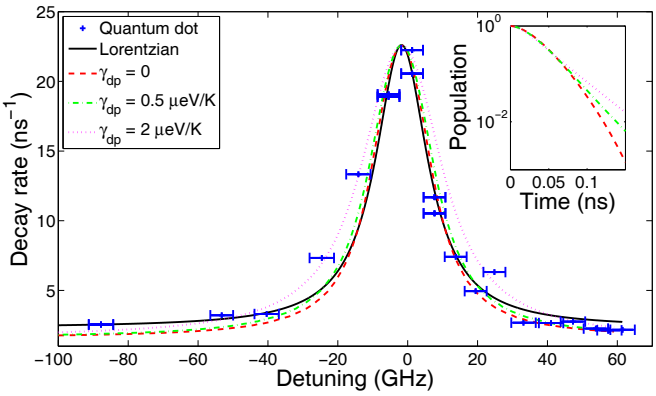

Figure 4.12: Comparison with different models to the data in figure 4.11. Only the data for the quantum dot peak have been plotted (blue crosses). The black line shows the same Lorentzian fit as in figure 4.11. The other three lines shows density matrix calculations where the overlap has been fitted to the maximum of the fitted Lorentzian. The calculations are done with no dephasing (red dashed line), a dephasing of 0.5 μeV/K (green dash-doted line), and for a dephasing of 2 μeV/K (magenta dotted line). To illustrate the difference in the decay the three decay curves of the model on resonance has been shown in the insert. The different lines correspond to the same parameters as the line in the main figure.

an additional decay rate due to non-radiative decay or an enlarged radiative decay not originating from the coupling to the cavity. The overlaps found for the two decay curves are 0.40 for $\gamma_{dp} = 0$ and 0.41 for $\gamma_{dp} = 0.5$ μeV/K. This will only be changed by a few percent with the inclusion of a non-radiative decay. These overlaps suggests that the quantum dot is just at the strong coupling limit as this gives $4g/\kappa = 1.2$ for the case of $\gamma_{dp} = 0.5$ μeV/K but this limit is only in the case of no dephasing. To illustrate the deviation from an exponential decay the decay of the population is displayed in the insert of figure 4.12 where the decay with a dephasing rate of 0.5 μeV/K only shows a small deviation from the exponential decay which would not be observable in the decay curves with the resolution of the experiment.

The comparison of the data with the model gives a consistent picture of the decay rate as function of the coupling to a micropillar cavity and shows no deviations from the theory of chapter 2 is seen.

4.4.2 Comparison between measured and calculated spectra

The values extracted from the time-resolved measurements can be used in the model to calculate the emission spectra as described in section 2.3.2. To compare the measured spectra with the model, spectra have been calculated with different temperature dependent dephasing rates. The calculated spectra along with the measured spectra from figure 4.9 are shown in figure 4.13. In the figure the complete series of spectra are compared to the calculated spectra with no dephasing, and a temperature dependent dephasing rate of 0.5 μeV/K and 2 μeV/K. The spectra in the figure are not directly comparable with the experimental spectra as they have not been convoluted with the instrument response of the spectrometer. One thing to notice is that the enhanced emission from the cavity is not modeled even by the calculation using a dephasing rate of 2 μeV/K. To make a real comparison with the experimental data the model has to be convoluted with the instrument response function which has been done and the resulting spectra shown in figure 4.14. Three selected spectra has been shown and the calculated spectra with dephasing is also shown. The spectra shows that a dephasing rate of 0.5 μeV/K is compatible with the data but the larger

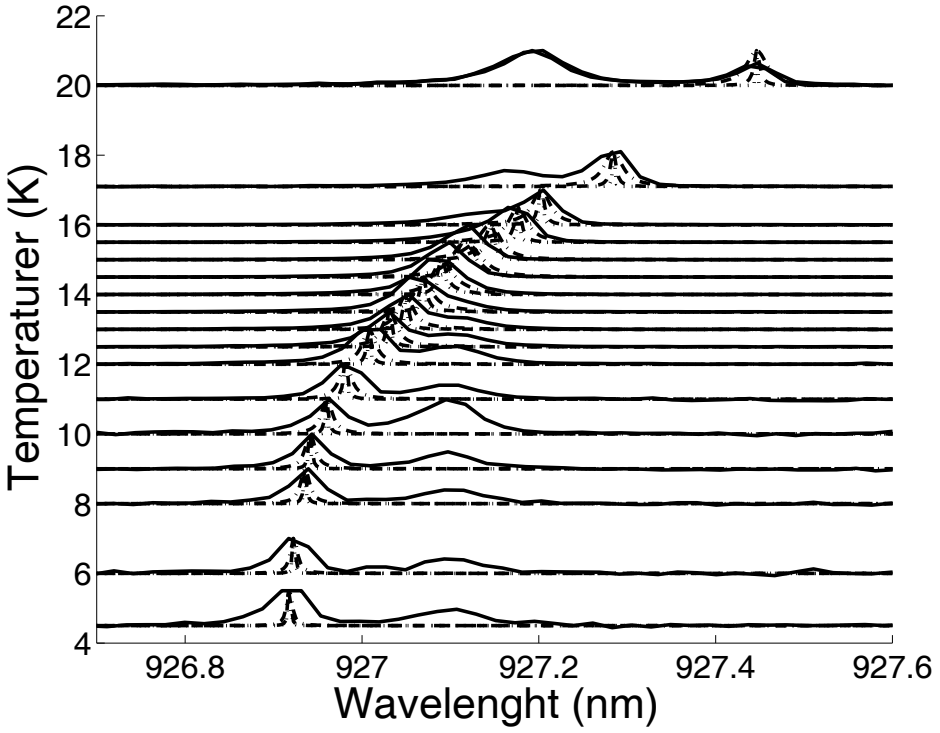

Figure 4.13: Comparison of the the experimental spectra from figure 4.9 (solid lines) with the spectra calculated using the density matrix model. The results without dephasing (dotted line) and the two temperature dependent dephasing rates used above: 0.5 μeV/K (red dashed line) and 2 μeV/K (dash-dotted line). The spectra have been scaled to the maximum intensity. The calculations have not been convoluted with the instrument response function (IRF) which is need for comparison with the experimental data and is shown in figure 4.14

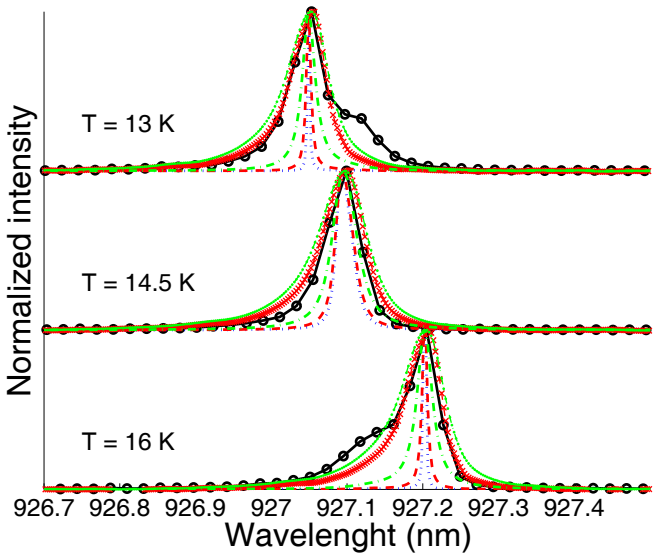

Figure 4.14: Selected experimental spectra from figure 4.9 (black circles) compared with the calculated spectra convoluted with the spectrometer IRF and a dephasing rate of 0.5 μeV/K (red crosses) and 2 μeV/K (green dots). Also shown are the non-convoluted spectra from the left figure.

dephasing of 2 μeV/K results in a too broad spectrum. This is consistent with the findings from the time-resolved data. The spectra also shows that the emission from the cavity peak off resonance cannot be accounted for by the model.

4.4.3 β-factor

An important parameter for the use of micropillars as single-photon sources or micro lasers is the β-factor. This can be calculated from the measured decay rates using eq. 2.21. The total decay rate is given by $\Gamma_{\mathrm{Tot}} = \gamma + \Gamma_{\mathrm{l}} + \Gamma_{\mathrm{nr}}$, where Γ_{l} is the decay rate into the leaky radiative modes modes of the micropillar and Γ_{nr} is the non-radiative decay rate. By assuming that $\Gamma_{\mathrm{l}} + \Gamma_{\mathrm{nr}}$ is given by the decay rate of the quantum dot detuned far from resonance. The β-factor on resonance can be calculated from the on resonance and off resonance decay rates (Γ_0 and Γ_Δ) as

$$\beta = \frac{\Gamma_0 - \Gamma_\Delta}{\Gamma_0} = \frac{22.3\ \mathrm{ns}^{-1} - 2.26\ \mathrm{ns}^{-1}}{22.3\ \mathrm{ns}^{-1}} = 0.90. \tag{4.2}$$

This value is comparable to values obtained in other systems such as photonic crystal waveguides as discussed in chapter 6 and photonic crystal cavities [88] showing that micropillars are good candidates for efficient single-photon sources. However, increasing the β-factor much higher will be limited by the large value of Γ_l which is not suppressed as efficiently as in the photonic crystal based micro structures.

4.5 Time-resolved measurements with non-resonant pumping

In several experiments in the literature the quantum dot has been excited non-resonantly above the GaAs band gap or in the wetting layer. The dephasing rates are also known to increase when excitation is not done in the excited states of the quantum dot [26] and this would influence the measured decay rates. As it was seen in the spectrum in figure 4.3 significant

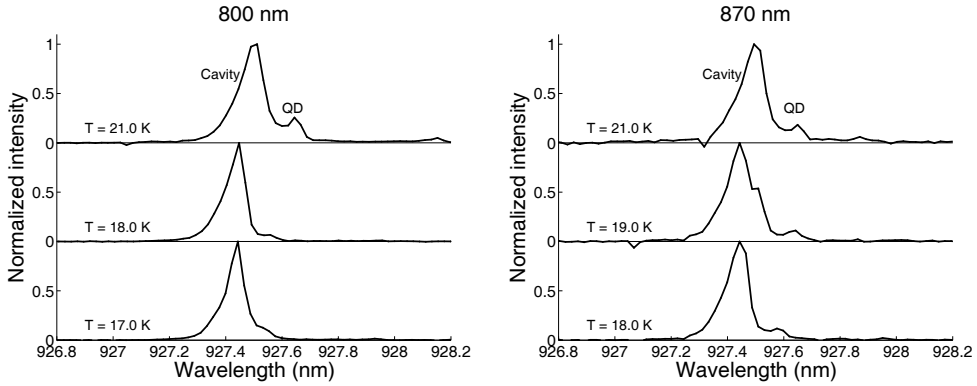

Figure 4.15: Normalized photoluminescence spectra of a 1.8 μm pillar. The excitation in the left figure was pulsed at 800 nm with a power of 2 μW into the cryostat and 870 nm with a power of 10 μW on the right figure. The quantum dot and cavity peaks are marked in the top spectrum.

emission is seen from the cavity resonance even though the quantum dot is not at resonance indicating that a lot of quantum dots couple to the cavity mode. To investigate the coupling under non-resonant excitation decay rates have been measured as a function of detuning for an excitation of 800 nm and 870 nm. The photoluminescence spectra are shown in figure 4.15. For both excitation wavelengths the saturation power has been measured and the power adjusted to excite the quantum dots at the same excitation power relative to saturation as for the p-shell excitation. The left image shows the emission when the excitation is done above the GaAs band gap. In this case strong emission is seen from the cavity compared to the case with p-shell excitation investigated above. For excitation in the wetting layer (870 nm), shown in the right part, a similar structure is seen. The cavity emission compared to the quantum dot emission is slightly smaller than in the case of 800 nm excitation.

The decay curves has been measured as a function of detuning by changing the temperature as above and examples of the resulting decay curves

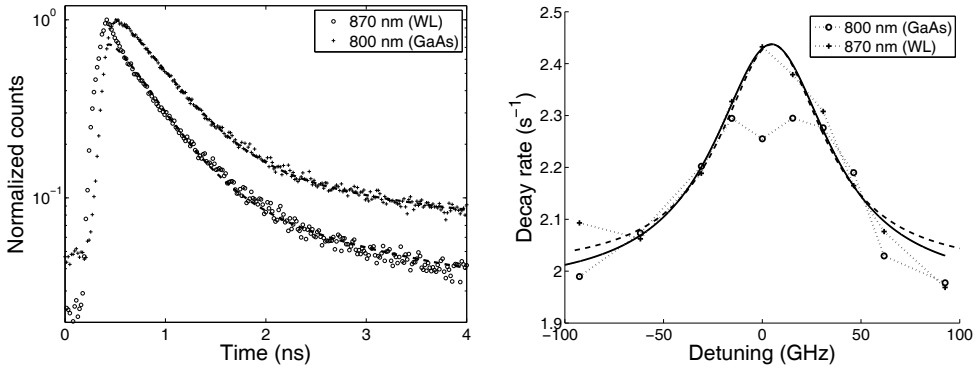

Figure 4.16: Left: Decay curves of a micropillar with a quantum dot on resonance with non-resonant excitation of the quantum dot. The two decay curves were taken with excitation above the GaAs band gap at 800 nm (crosses) or in the wetting layer (WL) at 870 nm (circles). The dashed lines show fits to a double exponential decay model. Right: Fitted fast decay rate as a function of detuning with different non-resonant excitation either above the GaAs band gap at 800 nm (crosses) or in the wetting layer (WL) at 870 nm (circles). The solid line shows a Lorentzian fit to the data points of the wetting layer excitation and has a width (FWHM) of 71 GHz.

with the quantum dot on resonance is shown in figure 4.16. The decay curve is significantly different from the case of p-shell pumping and cannot be modeled as a bi-exponential decay anymore where deviations are observed especially for short times. For excitation at 800 nm the decay curve has a flat top and the decay on resonance is only slightly larger than the off-resonant case as opposed to the much faster decay measured with p-shell pumping. The decay curve excited in the wetting layer shows a similar slow decay, however at the beginning of the curve a fast decay is seen which is not fitted with the double exponential model. This shows that the interpretation of the decay curves is not simple and that a crude interpretation will only be done below. Another indication of multiple quantum dots contributing to the emission is that no significant dip is seen in autocorrelation

measurements with the quantum dot on resonance.

To extract the decay rates the decay curves have been fitted with a double exponential model similarly to the decay curves with p-shell excitation. The fast decay rate as a function of detuning is shown in figure 4.16. An increase in the fitted decay rate is seen around resonance with both excitation wavelengths and except for two data points on resonance the decay rates follow each other. On resonance the decay rate where the excitation is done at 800 nm is slower and the line shape seems to be truncated. The decay rates with wetting layer excitation shows a more Lorentzian shaped peak. This has been fitted to a Lorentzian function which is also seen in figure 4.16. The Lorentzian fit the data well but with a linewidth corresponding to a Q factor of $4.5 \cdot 10^3$. This is more than twice the width of the peak in the p-shell pumped data above. This could indicate a large dephasing rate of the quantum dot. The peak can be fitted with the density matrix model used for the p-shell pumped data, where a dephasing rate of 200 μeV is found to fit the width of the data and an overlap of $F_d = 0.1$ is found to match the decay rate on resonance. The calculated decay rates using these parameters is shown as the green line in figure 4.16.The dephasing rate of 200 μeV is very high compared to measured values at low temperatures. Due to the much slower decay measured than for p-shell excitation and the bad fitting of the complex decay curves caution should be taken in the interpretation of these parameters.

The important conclusion is that to measure the Purcell factor of a quantum dot in a microcavity it is important to ensure that mainly emission from a single quantum dot is detected, which in this experiment is done by selectively exciting the quantum dots in an excited state.

4.6 Conclusion

The Purcell factor has been directly measured as a function of detuning of a single quantum dot coupled to a micropillar cavity. At resonance the decay rate was enhanced by a factor of ~ 10 compared to far away from resonance. The emission spectra show pronounced emission in the cavity even when the

quantum dot is detuned several cavity linewidths away from resonance. In contrast, Purcell enhancement is only observed within the cavity linewidth in agreement with theory. These observations are consistent with the models of quantum dots in cavities in the presence of pure dephasing presented in section 2.3 and other theoretical works [85, 86]. However, the emission from the cavity peak at large detunings are not accounted for in the theoretical spectra. This indicates along with the HBT measurement that the emission is not originating from the same quantum dot. The detailed comparison of the decay rate data with the model from section 2.3 gives a consistent picture of the interaction of the quantum dot with a micropillar cavity and shows that the measurements can be used to put an upper limit on the dephasing rate of the quantum dot of $\simeq 2$ μeV/K.

As the system is just at the strong coupling limit the pillar investigated is a very good candidate for a single photon source, however, the single-photon emission properties such as the photon statistics and indistinguishability of the photons must be investigated which is the subject of the next chapter.

Chapter 5

Single-photon emission from quantum dots in micropillar cavities

The property defining a single-photon source is the photon statistics as it should emit one and only one photon. Another important property for applications in quantum information is the photon indistinguishability. In this chapter these single-photon emission properties of the micropillars with embedded quantum dots investigated in chapter 4 are presented.

First the photon statistics is investigated using Hanbury-Brown and Twiss measurements to show that the quantum dots in the micropillar cavities emit single photons and the origin of multi-photon emission is explored. Then the photon indistinguishability is measured and the results are compared to the values expected from theory using the measurements on the coupling of the quantum dot to the micropillar cavity in chapter 4.

5.1 Single-photon emission

As discussed in section 2.4 the purity of the single-photon emission is characterized by measuring the normalized second order coherence ($g^{(2)}(\tau)$) using

a Hanbury-Brown and Twiss (HBT) setup.

The measurement can both be done using continues wave (cw) excitation or pulsed excitation. With continues wave excitation the width of the dip at $\tau = 0$ is given by the decay rate of the emitter while it will be a series of peaks using pulsed excitation as described in section 2.4. Which type of excitation to use is an important thing to consider when measuring $g^{(2)}(\tau)$.

The first parameter is the achievable count rate in the two cases. The coincidence count rate per bin of the measured correlation histogram is given by the count rates of the two APDs (CR_1, CR_2) and the bin size (Δt)

$$CCR = CR_1 \times CR_2 \times \Delta t = \frac{\alpha_1}{\Delta T} \times \frac{\alpha_2}{\Delta T} \Delta t, \tag{5.1}$$

where $\alpha_{1,2}$ is the collection efficiency of the setup including the quantum efficiency of the detectors and $1/\Delta T$ is the photon emission rate. With cw excitation the maximum photon emission rate from the source is given by the decay rate $\gamma = 1/T_1$, where T_1 is the decay time of the emitter. Using pulsed excitation the maximum emission rate is one photon per excitation pulse and the rate is given by the repetition rate of the laser $1/T_{\text{rep}}$. For the quantum dots in micropillar cavities investigated here decay rates up to 22 ns^{-1} was measured and the repetition rate of the laser is only 0.075 ns^{-1}. However, in a pulsed experiment the bin size is given by the laser repetition rate as all counts in the central peak corresponds to the same excitation. The ratio between the coincidence counts in a cw and pulsed experiments is then given by

$$\frac{CCR_{\text{cw}}}{CCR_{\text{pulses}}} = \frac{\Delta t \times T_{\text{rep}}}{T_1^2}. \tag{5.2}$$

This shows that for a fast decaying source the count rates in a cw experiment can be much higher depending on the bin size used. However, to resolve the dip in coincidence events at $\tau = 0$ a bin size much smaller than the decay time is needed. With e.g. a bin size of $T_1/10$ there is still a significant gain in using cw excitation proportional to the ratio between the repetition rate and the decay rate. This illustrates another problem with cw excitation as this bin size is much smaller than the time-resolution of the APDs used for detection. Even with the fast APDs (MPD) used for the time-resolved

measurements of chapter 4 the dip cannot be properly resolved which means that pulsed excitation must be used.

With pulsed excitation the correlation signal of a classical field is given by the probability of detecting a photon on one of the APDs ($F(t)$) as

$$S(\tau) = \int_{-\infty}^{\infty} F(t)F(t+\tau)dt. \tag{5.3}$$

The probability of detecting a photon on one of the APDs at a certain time (t) is given by the convolution of the decay of the quantum dot with the temporal instrument response function (IRF) of the setup. The shape of the IRF is mainly due to the time jitter of the APD as described in section 3.4.1. If the decay is assumed to be single exponential and the IRF is approximated by a Gaussian the signal on the APDs can be calculated as

$$F(t) = \int_0^t \Theta(t) e^{-\gamma(t-t')} \frac{1}{\sigma\sqrt{2\pi}} e^{-t'^2/2\sigma^2} dt' \tag{5.4}$$

$$= \Theta(t)\frac{1}{2} e^{-\gamma(t-\gamma\sigma^2/2)} \left(\mathrm{erf}\left(\frac{\gamma\sigma}{\sqrt{2}}\right) + \mathrm{erf}\left(\frac{t-\gamma\sigma^2}{\sqrt{2}\sigma}\right)\right), \tag{5.5}$$

where $\Theta(t)$ is the unit step function with a value of 1 for $t \geq 0$ and 0 for $t < 0$ and the FWHM of the IRF is given by $\sqrt{\ln(2)}\sigma$ which is a good approximation for the high sensitivity (PE) APDs used in the measurements in this section. The integration in eq. 5.3 can now be done to get the shape of the peaks. The integration cannot be done analytically due to the step functions but can be done numerically. The width of the peak is either limited by the width of the IRF (σ) for fast decay rates or by the decay rate for slow decay rates. For the repetition rate of the laser of 76 MHz this means that the peaks are well separated as $T_{\mathrm{rep}} \ll \sigma,\ \gamma$.

5.1.1 Hanbury-Brown and Twiss measurements

To measure the HBT signal the light collected from the micropillar is directed to the HBT part of the setup described in section 3.4.2 where the collected fluorescence from the samples in the cryostat is put on a beam

splitter and the two output arms are directed to the two separate spectrometers. The spectrometers are set to the same detection wavelength and the width of the output slits are set to a detection bandwidth of 0.1 nm. The photon arrival time is then recorded by the TCSPC electronics and the correlation of the data is done.

For all of the HBT measurements presented in this chapter pulsed excitation was used. The high efficiency APDs (PE) were used for detection as these are ~ 5 times more sensitive than the fast APDs resulting in a factor of ~ 25 in the coincidence count rate. The poorer time-resolution is still much smaller than the repetition rate. Another reason to use pulsed excitation is that the measurements of photon indistinguishability is done using pulsed excitation and that the HBT measurements are important in the interpretation of these.

An example of a HBT measurement is seen in the top part of figure 5.1. The measurement in done on the micropillar previously investigated in chapter 4 with the quantum dot on resonance and with pulsed p-shell excitation at 909 nm. The data show a series of peaks separated by the repetition rate of the laser (~ 13 ns). A strong decrease of the peak at a delay of ~ 8 ns is seen which is the peak corresponding to a time delay of zero at the beam splitter. The delay of ~ 8 ns is due to the difference in optical length from the beam splitter to the two APDs and the difference in length of the APD cables. To find the area of the peaks the centers of the peaks are first found to get the delay interval corresponding to each peak. The total counts in each interval, shown by the red lines in figure 5.1, are then found to obtain the peak areas which are plotted in the lower part of the figure. A zoom of one of the central and one of the non-central peaks are also shown in the insert. This shows the shape of the peaks and the model from eq. 5.3 is plotted, where the measured FWHM of the IRF and the measured decay rate from time-resolved measurements has been used and the height has been fitted. The fit is seen to follow the data very well and shows that the decay rate is high. The decay rate could also be fitted from these data but the IRF of the APDs is too broad to be used to fit the fast decay rate of the quantum dot.

To find the second order coherence the central peak area is then nor-

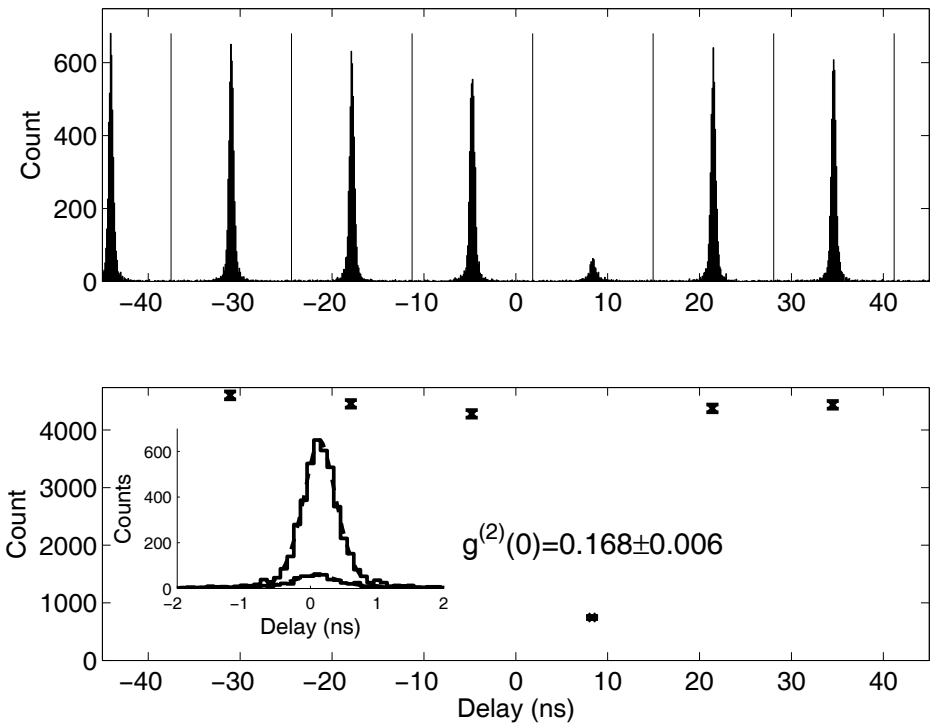

Figure 5.1: Top: Pulsed HBT measurement on a micropillar with p-shell excitation of 500 μW. The quantum dot is tuned to resonance with the cavity and the temperature is 14.5 K. Bottom: The integrated counts for each pulse interval marked by the vertical lines in the top figure. The normalized second order coherence found from the central peak at a delay of 8 ns is 0.168 ± 0.006. The insert shows one of the non-central peaks and the central peak along with the modeled peak shape shown by the dashed line.

malized to the mean value of the non-central peaks. In the measurements of figure 5.1 a central area of $16.8 \pm 0.6\%$ is found. As the value is below 0.5 this shows that the micropillar is emitting single-photons. There is, however, still a residual multi-photon emission which can either originate from the quantum dot or from other quantum dots coupling to the cavity mode.

Measurements have been done on several pillars and values ranging from 0.13 to more than 0.5 were found on different pillars all with slower decay rates and with the best results for low power and good coupling to the cavity. To investigate where the residual emission is originating from, the single-photon emission has been investigated for different pump powers and detunings of the quantum dot with the cavity mode.

5.1.2 Power dependence on the single photon emission

The quantum dot is pumped close to the saturation of the ground state and this might influence the purity of the single-photon emission. To investigate this the second order coherence of the micropillar with the quantum dot on resonance with the cavity has been measured for different pump powers.

The results for three different pump powers are shown in figure 5.2. The figure shows $g^{(2)}(0)$ as function of the pump power, where the power is the input power to the cryostat. The saturation power was measured in chapter 4 to be ~ 500 μW. A clear dependence on the second order coherence is seen with a lower value of $g^{(2)}(0)$ for lower pump power. A simple model for the power dependence of the second order coherence can be found by using eq. 2.61 and assuming a linear dependence of the incoherent emission such that $n_b = \mu P$:

$$g^{(2)}(0, P) = \frac{2\mu P + (\mu P)^2}{(1 + \mu P)^2}, \tag{5.6}$$

The constant μ can now be fitted to the data. The model implies that the second order coherence should go to zero at low excitation powers. However, this is not supported by the data and the model has therefore been fitted to the data both with and without an offset at $P = 0$ μW. The two resulting models are plotted in figure 5.2 as the dotted (without offset) and dashed (with offset) black lines. The model with an offset gives a very good fit

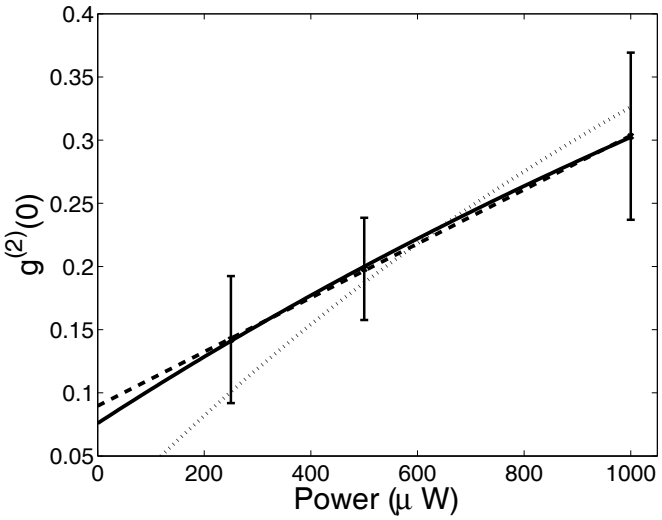

Figure 5.2: Pump power dependence of the second order coherence of a micropillar cavity. The pump power on the x-axis is the power reaching the cryostat. A fit to the model described in the text is shown (solid line). A value of $g^{(2)}(0, P = 0\ \mu\text{W}) = 7.6\%$ and $1.4 \cdot 10^{-4}\ \mu\text{W}^{-1}$ background photons per pulse is found from the fit. The dotted line shows the model without an offset For reference a linear fit is also shown (dashed line) giving a value of $g^{(2)}(0, P = 0\ \mu\text{W}) = 9.0\%$.

and a value of $g^{(2)}(0,0) = 8.2\%$. The model without offset does not fit the data very well even though it is consistent with the error bars. This indicates that there is both a multi-photon contribution to the emission that is proportional to the pump power and a constant contribution. As n_b in the model is the ratio between the incoherent and single-photon emission (N_b/N_a) the offset is explained by contribution from one or more other quantum dots as they will have the same linear power dependence of the emission as the qauntum dot on resonance.

The proportionality of the multi-photon emission with the pump power could be explained by the generation of biexcitons from long lived dark excitons [19]. This would happen if a dark exciton is created and it stays in the dot until another exciton is created resulting in a two-photon emission as both states are now bright excitons. The probability of this is proportional to the square of the power resulting in a linear contribution of two-photon events relative to the one-photon events as a function of pump power.

5.1.3 Influence of detuning on the single-photon emission

If there is a contribution to the emission of the micropillars from other quantum dots the single-photon emission is purest when the quantum dot is on resonance with the cavity as the channeling of photons due to the increased β factor will enhance the emission from the single quantum dot ground state. To investigate the origin of the multi-photon emission and whether it is dependent on the detuning the second order coherence has been measured as a function of the coupling of the quantum dot to the cavity. This is done by varying the temperature of the sample and thereby the detuning of the quantum dot to the cavity mode. The coupling was already measured in 4 which forms the basis of understanding the dependence of the single photon emission. The temperature was varied and $g^{(2)}(0)$ was measured at the emission wavelength of the cavity. The results are shown in figure 5.3.

The data show the expected increase in second order coherence as the quantum dot is detuned away from the cavity mode. A model of the detuning dependence of $g^{(2)}(0)$ can be constructed by considering the contributions

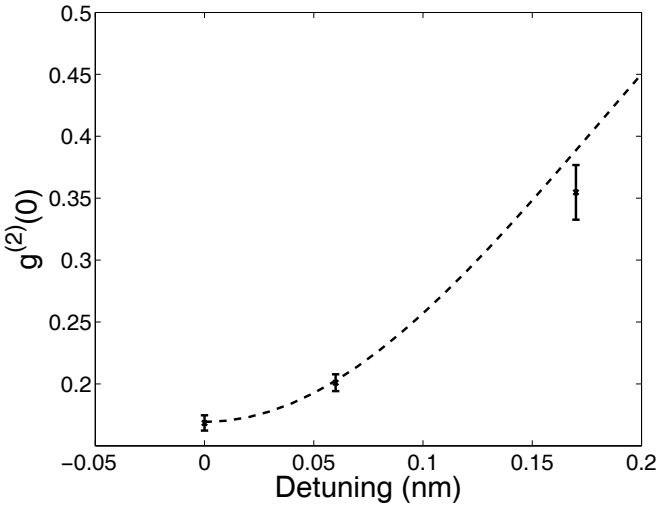

Figure 5.3: The second order coherence as function of the detuning of the cavity to the quantum dot emission wavelength. The dashed black line shows the model described in the text.

to the signal from an incoherent source N_b to be independent on the detuning and the single photon emission N_a to be given by the β factor of the cavity. The relative contribution from the incoherent source as a function of detuning is then given by

$$n_b = \frac{N_b}{N_a(\Delta)} = \frac{N_b\beta(0)}{\beta(\Delta)N_a(0)} = n_b(0)\frac{1}{\beta(\Delta)}. \tag{5.7}$$

The expression for the β factor is given in section 2.2.3 and assuming that the decay rate at large detunings (γ) is the homogenous decay rate (Γ_0) and using a Lorentzian model of the decay rate as function of detuning the β factor can be calculated. Inserting the expression for n_b in eq. 2.61 the second order coherence is found. The dependence of the decay rate on the detuning was found in section 4.4.1 and the values from the Lorentzian fit to the decay rate in this section can then be used in the model. The result is shown as the black dashed line in figure 5.3. The model fits the data well even though there are not many measurement points it shows that the photon flux from the multi-photon field does not change significantly with detuning. This means that the multi-photon emission is not originating from the quantum dot state coupled to the cavity and shows that the most probable cause of the impurity of the single-photon emission is caused by emission from other quantum dot emission lines that are not in resonance with the cavity mode but still couples weakly to the cavity mode. This could be the same contribution that was seen in the emission spectra in section 4.4 and is consistent with this.

5.2 Photon indistinguishability and Hong-Ou-Mandel interferometry

The indistinguishability of the photons emitted by the micropillar is measured using a Hong-Ou-Mandel interferometer [53]. As described in section 2.5 the photon indistinguishability is measured by interfering two individual photons on a beam splitter and measure the time correlation of the output of the beam splitters. The two photons are generated by the same quantum

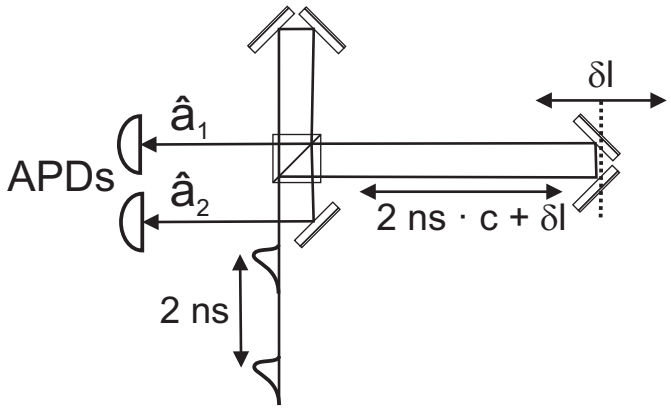

Figure 5.4: A sketch of the Hong-Ou-Mandel interferometer. The photons enter the interferometer from below with a time delay Δt (2 ns) and are split into a short and a long arm with a difference in length given by $\Delta t \cdot c + \delta l$. The photons are then combined on the beam splitter and detected by single-photon detectors (APDs) on the output ports of the beam splitter.

dot by consecutive excitations. This is done by generating two excitation pulses with a delay (Δt) that is much larger than the decay time of the quantum dot to allow the quantum dot to decay before reexcitation. In this way the quantum dot will emit two photons with a time delay of Δt into the same mode.

To overlap the two emitted photons a HOM interferometer as illustrated in figure 5.4 is used. The interferometer works by first splitting the photons on the lower left part of the beam splitter into the short and the long arm of the interferometer and then recombines on the upper right corner of the beam splitter. The long arm is adjusted to be approximately Δt longer than the short arm such that if the first photon enters the long arm and the second the short arm they will overlap on the beam splitter.

The input state can be written in the same way as in eq. 2.64 but with

the two photons as excitations of the same mode with a time delay of Δt:

$$|\Psi\rangle = \int_0^\infty \int_0^\infty dt_1 dt_2 x_1(t_1) x_2(t_2) \hat{a}^\dagger(t_1) \hat{a}^\dagger(t_2 + \Delta t)|0\rangle. \tag{5.8}$$

The field operators at the two outputs of the beam splitter given by the input field $\hat{a}(t)$ is

$$\hat{a}_1 = -\sqrt{RT}\hat{a}(t - \delta t) + \sqrt{RT}\hat{a}(t) \tag{5.9}$$
$$\hat{a}_2 = R\hat{a}(t - \delta t) + T\hat{a}(t), \tag{5.10}$$

where $\delta t = \Delta t + \delta l/c$ is the time delay of the long arm of the interferometer and R and T is the intensity reflection and transmission coefficients of the beam splitter. From these equations the correlation signal can be calculated as the second order coherence of the outputs. It is assumed that the quantum dot decays much faster than δt and that $\delta t - \Delta t$ is on a time scale comparable to the decay time. The second order coherence is given by

$$\begin{aligned} G_{12}^{(2)}(\tau) &= \langle \hat{a}_1^\dagger(t) \hat{a}_2^\dagger(t+\tau) \hat{a}_2(t+\tau) \hat{a}_1(t) \rangle \\ &= \langle TR^3 \hat{a}^\dagger(t - \delta t) \hat{a}^\dagger(t - \delta t + \tau) \hat{a}(t - \delta t + \tau) \hat{a}(t - \delta t) \rangle \\ &\quad - \langle T^2 R^2 \hat{a}^\dagger(t - \delta t) \hat{a}^\dagger(t + \tau) \hat{a}(t - \delta t + \tau) \hat{a}(t) \rangle \\ &\quad + \langle T^3 R \hat{a}^\dagger(t - \delta t) \hat{a}^\dagger(t + \tau) \hat{a}(t + \tau) \hat{a}(t - \delta t) \rangle \\ &\quad + \langle TR^3 \hat{a}^\dagger(t) \hat{a}^\dagger(t - \delta t + \tau) \hat{a}(t - \delta t + \tau) \hat{a}(t) \rangle \\ &\quad - \langle T^2 R^2 \hat{a}^\dagger(t) \hat{a}^\dagger(t - \delta t + \tau) \hat{a}(t + \tau) \hat{a}(t - \delta t) \rangle \\ &\quad + \langle T^3 R \hat{a}^\dagger(t) \hat{a}^\dagger(t + \tau) \hat{a}(t + \tau) \hat{a}(t) \rangle \end{aligned} \tag{5.11}$$

This means that there will only be contributions to the correlation of the detectors for correlation time (τ) of $\pm 2\delta t$, $\pm\delta$, and 0. This will result in five peaks at these time differences instead of the single peak in the HOM setup. From the normalized second order coherence, the number of excitation events (N) and the combined two-photon generation and detection

efficiency η_2, the mean areas of the five peaks can be calculated:

$$\begin{aligned} A_0^{(2)} &= N\eta_2 g_{12}^{(2)}(0) \\ &= N\eta_2 \left((R^3T + RT^3)(1 + 2g^{(2)}) - 2R^2T^2V_{\mathrm{i}}^2 V(\delta t) \right) \quad (5.12) \\ A_{-1}^{(2)} &= N\eta_2 g_{12}^{(2)}(-\delta t) = N\eta_2 \left(R^3T(1 + 2g^{(2)}) + RT^3 \right) \quad (5.13) \\ A_{+1}^{(2)} &= N\eta_2 g_{12}^{(2)}(+\delta t) = N\eta_2 \left(R^3T + RT^3(1 + 2g^{(2)}) \right) \quad (5.14) \\ A_{-2}^{(2)} &= N\eta_2 g_{12}^{(2)}(-2\delta t) = N\eta_2 R^3T \quad (5.15) \\ A_{+2}^{(2)} &= N\eta_2 g_{12}^{(2)}(+2\delta t) = N\eta_2 RT^3, \quad (5.16) \end{aligned}$$

where V_{i} is the visibility of the interferometer and $g^{(2)}$ is the normalized second order coherence of the single photon source.

The above peak areas are only calculated for the events where two photons are generated. There is also a contribution from the excitations resulting in a single photon emission at $t = 0$ or $t = \delta t$. This contribution can be calculated from eq. 5.11 and will give a contribution to the central peak and the peaks at $\pm\delta t$ of

$$\begin{aligned} A_0^{(1)} &= N\eta^{(1)} g^{(2)} (R^3T + RT^3) \quad (5.17) \\ A_{-1}^{(1)} &= N\eta^{(1)} g^{(2)} R^3T \quad (5.18) \\ A_{+1}^{(1)} &= N\eta^{(1)} g^{(2)} RT^3, \quad (5.19) \end{aligned}$$

where η_1 is the single photon generation and detection efficiency. The contribution is proportional to $g^{(2)}$ and the contribution will thereby only be significant if there is a significant multi-photon emission from the source. The measured peak areas are then given by the sum of the single-photon and two-photon contributions ($A_j = A_j^{(1)} + A_j^{(2)}$).

The quantum dot is assumed to decay before reexcitation and the excitation probability of two excitations are then given by the single excitation probability (P_1) squared. The ratio between the two-photon and single-photon emission and detection efficiencies are then given by $\eta_2/\eta_1 = P_1$ as the detector efficiencies are the same. If the experiment is done with a

pump power close to saturation and the source has a non-vanishing $g^{(2)}$ the contribution from the single-photon events cannot be neglected.

The equations 5.12 to 5.16 show that the signature of photon indistinguishability is a smaller area of the central peak compared to the peaks at $\pm\delta t$. The parameter M characterizing the indistinguishability is therefore defined as

$$M(\delta t) = \frac{A_0}{A_{-1} + +A_{+1}} \tag{5.20}$$

$$= \frac{\eta_1 g^{(2)}(R^3T + RT^3) + \eta_2(R^3T + RT^3)(1 + 2g^{(2)}) - 2R^2T^2V_{\mathrm{i}}^2V(\delta t)}{\eta_1 g^{(2)}(R^3T + RT^3) + \eta_2(R^3T + RT^3)(2 + 2g^{(2)})}$$

$$= \frac{g^{(2)}}{g^{(2)} + (2 + 2g^{(2)})P_1} + \frac{1 + 2g^{(2)}}{2 + 2g^{(2)} + P_1^{-1}g^{(2)}}$$

$$- \frac{2RTV_{\mathrm{i}}^2}{(R^2 + T^2)(2 + 2g^{(2)} + P_1^{-1}g^{(2)})}V(\delta t). \tag{5.21}$$

For two photons entering the beam splitter and $g^{(2)} \sim 0$ this is the probability of the two photons to exit in different directions. The parameter is directly obtained form experimental data and is independent of the number of counts. A decrease in this value as function of time difference of the photon arrival time shows that the photons are partly indistinguishable.

5.2.1 Photon indistinguishability measurements

The HOM signal has been measured on the micropillar sample investigated in the section above and with excitation in the 'p-shell'. The two excitation pulses needed to measure the photon indistinguishability are generated by the delay line in the excitation setup shown in figure 3.1. The pulse from the laser is split on the first beam splitter and one part enters the delay line where it is delayed relative to the other pulse. The delay should be small enough such that there is no overlap between subsequent repetitions of the experiment set by the repetition time of the laser ($T_{\mathrm{rep}} \sim 13$ ns). As the interferometer introduces another delay of $\sim \Delta t$ the time delay should be kept within $T_1^{qd} \ll \Delta t < T_{\mathrm{rep}}/4$ and a delay of 2 ns is therefore used.

The excitation power used in the experiment was 250 μW per pulse which is half the saturation power of the saturation model described in section 4.3.4. This means that the single excitation probability (P_1) is expected to be around 0.39 for this pump power.

The visibility of the interferometer (V_i) is measured before each HOM measurement and each time the interferometer is adjusted using the diode laser as described in section 3.4.3 and values between 90% and 95% are found depending on the interferometer delay.

The collected photons are sent through a polarizer to only measure one linear polarization and further into the HOM interferometer by changing the fiber output to the input port of the interferometer as described in section 3.4.3. The spectrometers are both set to the emission wavelength of the pillar and 0.1 nm detection bandwidth is used with the photons detected by the high quantum efficiency APDs (PE). The photon arrival times are then recorded by the TCSPC electronics from which the correlation histogram can be calculated.

A correlation histogram of a HOM measurement of the 2 μm micropillar investigated in section 5.1.1 and with the interferometer delay matching the excitation delay ($\delta l = 0$) is seen in figure 5.5. The count rates on the single photon detectors was $1.5 \cdot 10^4$ s^{-1} per channel giving a two photon rate of 3 s^{-1}. The histogram shows the five peaks corresponding to the five events described above. The central group of peaks is seen to be reduced compared to the other peaks and the central peak of this group is also seen to be reduced compared to the two neighboring peaks. This shows that the photons are bunching together on the same output port of the beam splitter and is the indication of photon indistinguishability.

To quantify the indistinguishability of the photons the M value defined in eq. 5.20 is found. This is done by finding the repetition rate of the laser and the distance between the five peaks in each group from the non-central peaks as these have a larger number of counts. From this the bins belonging to each of the central peaks are found and the total area of the peaks are calculated. The result is shown in the lower part of figure 5.5 which also clearly shows a reduction of the central peak. As it is seen in figure 5.5 there is a small overlap of the individual peaks. To better separate the

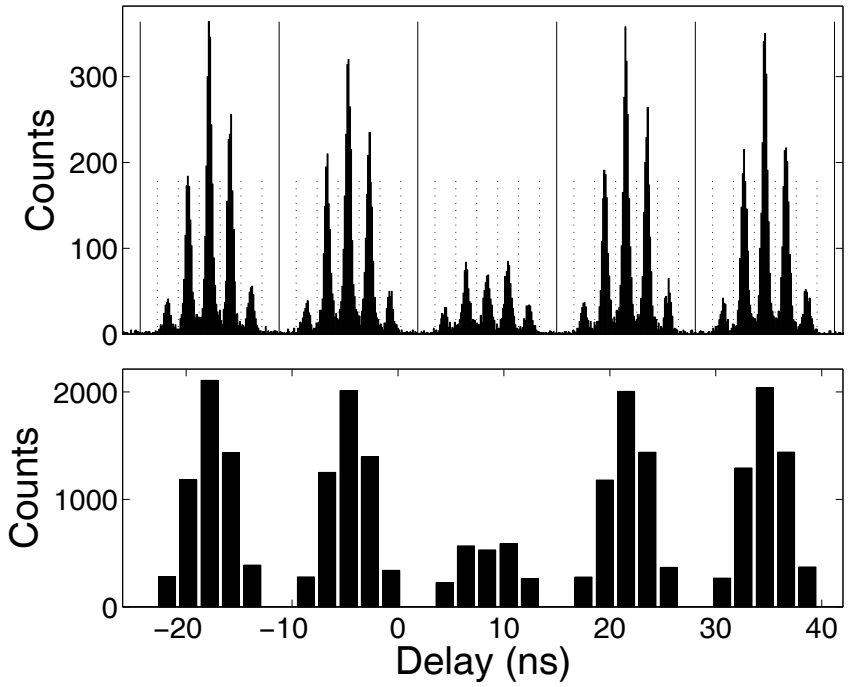

Figure 5.5: Correlation histogram of a HOM measurement on a 2 μm micropillar with p-shell excitation of 250 μW per pulse. The quantum dot is on resonance with the cavity and the temperature of the sample was 14.5 K. The count rates on the single photon detectors was $1.5 \cdot 10^4$ s^{-1} per channel. The top plot shows the histogram of the difference photon arrival time on the two detectors. The solid vertical lines separates the individual groups of peaks corresponding to the repetition time of the laser and the dotted lines are the separation of the peaks used for calculating the peak areas in the lower histogram. The lower histogram shows the total counts in each peak where the summation is done between the dotted lines on the above histogram.

contribution to the peaks it was attempted to fit the complete set of five peaks using the model of the peak shape from eq. 5.5. This gave results that could not be distinguished from the ones obtained by the simpler procedure and the procedure of summing the bins for each peak was used instead as it is more clear and direct. From the peak areas the M value of the data in figure 5.5 is found to be 0.46 ± 0.02. The uncertainty is the standard deviation given by the square root of the number of counts in each peak. To find the two-photon overlap from the M value the value of $g^{(2)}(0)$ and the single-photon emission probability must be known as shown in eq. 5.21. The $g^{(2)}(0)$ value is known from the HBT measurements in section 5.1.1 above but the single-photon emission probability is not known precisely. To find this the HOM signal should be measured as a function the interferometer delay to find the value at large delays where there is no two-photon overlap.

To find the two-photon overlap the HOM signal is measured for a series of interferometer delays. The interferometer is optimized and the visibility is measured at every setting of the interferometer delay. For each delay a correlation measurements is done and the M values are found. The resulting M values are shown in figure 5.6. The figure shows a clear dip of the M value as function of the interferometer delay with a minimum value at zero time delay and reaching a constant level at a time delay of ~ 0.2 ns.

This data can now be fitted to the model of equation 5.21 with the dependence on the overlap given by the expression in eq. 2.66. The value of $g^{(2)}(0)$ is known from the HBT measurements of section 5.1.1, the visibility of the interferometer is measured by the diode laser and the decay rate of the quantum dot in the pillar is known from the time-resolved measurements in chapter 4. The unknown parameters left are the single-photon emission probability (P_1) and the dephasing rate (γ_{dp}). The single-photon emission probability will result in an offset of the curve and the dephasing rate gives the depth of the dip. The resulting least squares fit to the data are show as the solid black line in figure 5.6. The fit results in a single-photon emission probability $P_1 = 0.36 \pm 0.04$ and a dephasing rate of $\gamma_{dp} = 9.3 \pm 2.7$ GHz. The errors are obtained from the covariance matrix of the least squares fit and the model calculated with the parameters $\pm$ the errors are plotted as the dotted lines in figure 5.6.

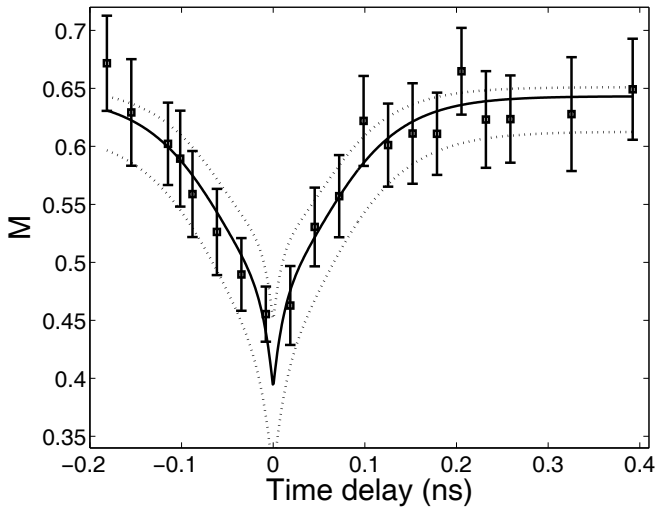

Figure 5.6: The ratio between the central peak and the two peaks at $\pm\Delta t$ (M) as function of interferometer time delay. The error bars are the standard deviation given by the number of counts in the peaks of the time correlation histogram. The solid black line is a fit to the data using the model described in the text. The dotted black lines show the model calculated with $\pm$ the standard deviation of the parameters obtained from the fit.

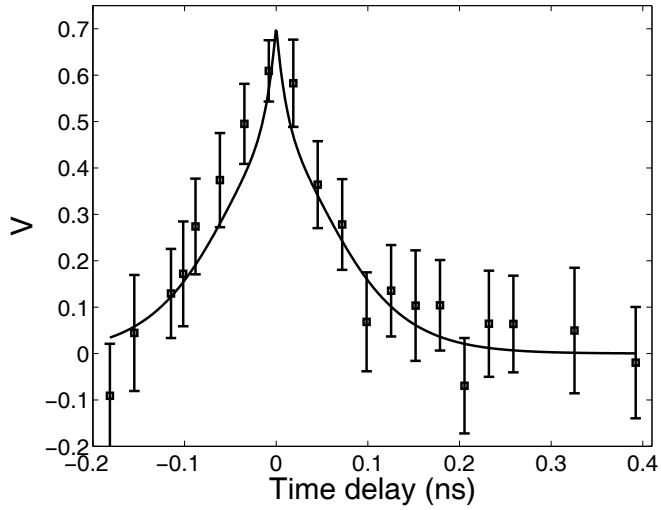

Figure 5.7: The two-photon overlap (V) calculated from the M values in figure 5.6 using the measured values of the interferometer visibility and $g^{(2)}(0)$. The value of the single photon emission probability (P_1) is taken from the fit to the data in figure 5.6 as described in the main text. The solid line is the two-photon overlap found from the fit shown in figure 5.6.

The single-photon emission probability of the fit corresponds very well to the expected value of ~ 0.39 from the measurements of the saturation intensity in section 4.3.4 supporting the validity of the model. The dephasing rate corresponds to 6.10 ± 1.80 μeV and for a linear temperature dependence of the dephasing rate this gives 0.42 ± 0.12 μeV/K. This is consistent with the modeling of the decay rates measured and the spectra in chapter 4.

Using the value of P_1 obtained from the fit the two-photon overlap (V) can be calculated using eq. 5.21. The resulting overlap as function of interferometer delay is shown in figure 5.7. The figure also shows the value of the overlap from the fit to the data in figure 5.6 as the solid black line. The maximum two-photon overlap is found to be 0.61 ± 0.07 with the fit

reaching a value of 0.71, which is between the two lowest measured points.

This value is smaller than the optimum values reported for micropillars in the literature where a value of 0.81 is found somewhere between 3 and 7 K [8] and 0.75 at 4 K [89]. Since the primary limitation of the indistinguishability is the dephasing a lower value would have been reached with a quantum dot on resonance with the cavity at a lower temperature. If a micropillar with the same Purcell effect as the one investigated here was found with a quantum dot on resonance at 4 K and a dephasing rate depending linearly on temperature as measured in literature (e.g. [26]) the dephasing rate would be $\sim$ 2.5 GHz resulting in a photon overlap reaching 0.90. In Varoutsis et al. [89] the indistinguishability is measured as a function of temperature and the dependence on temperature is found to be much weaker and only a change from an overlap of 0.59 to 0.62 is found from 15 K to 4 K for a quantum dot not resonant with the cavity. This indicates that such high visibilities cannot be reached in the micropillars investigated here, however with the right micropillar this could be tested.

5.2.2 Temperature and detuning dependence on the photon indistinguishability

To further investigate the temperature dependence the photon indistinguishability has been measured on the micropillar for different temperatures. This results in the quantum dot being detuned from the cavity resonance which will decrease the photon overlap.

The indistinguishability was measured at the emission wavelength of the quantum dot as described in the previous sections. As the detuning of the quantum dot from the pillar also reduces the detected count rates the measurement times increases with detuning and only a few temperatures have been measured and only with an interferometer time delay of 0. The overlap is calculated from the measured M values using the procedure described above and same excitation probability. The resulting overlap is plotted in figure 5.8. The figure shows a strong reduction of the overlap when the quantum dot is detuned from the cavity. This can be compared with the value calculated using the knowledge of the detuning dependence

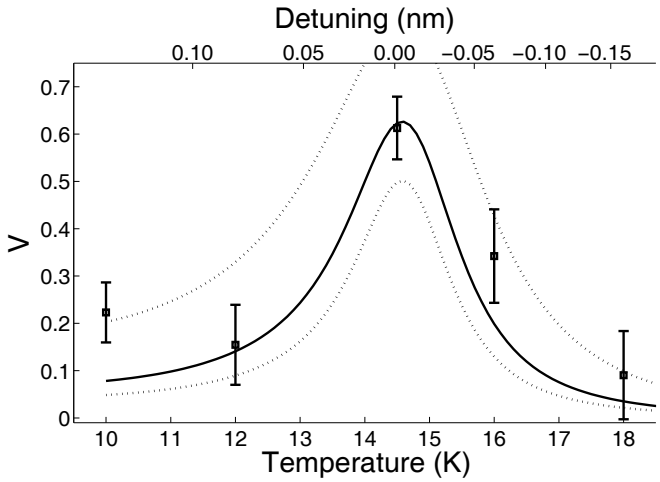

Figure 5.8: The two-photon overlap for a quantum dot in a micropillar as a function of temperature or detuning. The emission was recorded at the wavelength of the quantum dot emission line. The solid line is the model described in the text with a dephasing rate of 0.6 μeV/K and the two dotted lines are with a dephasing rate of 0.2 (upper) and 1.0 μeV/K (lower).

of the decay rate from section 4.4.1 and the temperature dependence of the dephasing rate. The maximum overlap as a function of temperature can be calculated from eq. 2.67, where the decay rate dependence of the decay rate is due to the detuning of the quantum dot to the cavity mode and the dephasing rate changes with temperature. Using a linear dependence of the dephasing rate with temperature this model is plotted as the black lines in figure 5.8 where the solid line is for a dephasing rate of 0.6 μeV/K and the dotted lines are for 0.2 μeV/K and 1.0 μeV/K.

The data are seen to follow the general trend with a maximum overlap on resonance. An increase in the overlap is seen at 10 K but the overlap is also above the theoretical curve for the high temperatures and the large error bars makes it difficult to conclude and more measurements with better signal are needed. The data also shows the importance of being at resonance with the pillar for high indistinguishability and temperature stability is therefore important for these sources.

The influence of the dephasing on the spectra and the time-resolved measurements also includes a possible slow frequency diffusion with time scales up till the integration time of the measurements. In contrast, if there is a slow spectral diffusion of the quantum dots the indistinguishability will only be influenced by these if they are happening on a timescale slower than the time difference of the two photons. As the dephasing rates of the two measurements are consistent it shows that the dephasing of the emitters are primarily resulting from interaction on a timescale faster than the 2 ns between the reexcitation of the quantum dot.

5.3 Conclusion

Single-photon emission and photon indistinguishability were successfully measured from quantum dots in micropillar cavities. The micropillars investigated were found to emit single photons with a minimum multi-photon emission of 0.13. The origin of the multi-photon emission was investigated and found to be dependent on the pump power but not dependent on the detuning of the cavity this supports the hypothesis that the multi-photon

emission is originating from other quantum dots that are not on resonance but still coupling to the cavity.

The single-photon emission might be improved by investigating more samples or it could be optimized by using pillars with lower densities of quantum dots at the resonance frequency of the micropillars. This would, however, result in fewer pillars with a quantum dot emission wavelength at the resonance of the cavity at low temperatures and with an efficient coupling to the micropillar. This illustrates the general problem of finding suitable micropillars for use as single photon sources. However, recent developments in the positioning of quantum dots [22] promise to remove one of these problems by enabling the positioning of the quantum dots at the precise center of the pillar.

A photon indistinguishability of 61% was measured at a temperature of 14.5 K. This in not as good as the optimum values measured by others [8, 89], but for the higher temperature it is an expectable value. The measured photon indistinguishability could be improved by finding another sample with a quantum dot resonant with the cavity at lower temperature to reduce the dephasing rate.

The indistinguishability might also be improved by excitation of the quantum dots directly in the ground state. This has very recently been demonstrated in micropillars similar to the ones investigated here resulting in the highest two photon overlap of 90% measured with solid state sources [90]. This value is comparable to the value measured for cold atoms [91] which shows the potential of quantum dot single-photon sources for quantum information processing.

Chapter 6

Coupling of single quantum dots to a photonic crystal waveguide

The ability to control the spontaneous emission dynamics using photonic crystals has been demonstrated experimentally within the last few years [41, 11, 12, 13, 33]. This has been used to demonstrate single-photon sources where the photons are harvested when a quantum dot is coupled efficiently to an enhanced optical mode. One very successful approach has been to couple single quantum dots to a photonic crystal nanocavity [11, 12, 13]. This is analogous to the coupling of quantum dots to the micropillar cavities presented in the previous chapters. In this process, photons are emitted with large probability to the localized mode of the cavity at a strongly enhanced rate. A drawback of this approach, however, is that the photons subsequently must be coupled out of the cavity, which will reduce the overall efficiency of the device significantly. Furthermore, nanocavity single-photon sources only operate within a narrow bandwidth determined by the high Q factor of the cavity as it was shown in chapter 4. Recently it was proposed that photonic crystal waveguides provide a way of overcoming these limitations [14, 15, 16, 17], which was inspired by early work by Kleppner on metallic waveguides [34] as discussed in section 2.2.1. The special property of photonic crystal waveguides is the possibility to tailor the dispersion of

light by proper design of the structure to have a slow light regime below the light line. In this way impressive light slow-down factors of 300 have been experimentally demonstrated [92]. The efficient slow-down of the photonic crystal waveguide mode implies that the light-matter coupling strength will be largely enhanced as shown by eq. 2.19. This enhanced coupling will allow the efficient channeling of single photons from a quantum dot into the photonic crystal waveguide mode [15, 16, 17]. In this case, the photons are transferred directly to the propagating mode of the photonic crystal waveguide, which is fundamentally different from the coupling to the cavity, and implies that the overall efficiency of the source is potentially very high. Furthermore, the enhancement in a photonic crystal waveguide is not limited to a narrow spectral bandwidth as in a cavity, and precise control over the quantum dot position is not as critical. Consequently demands for spatial and spectral tuning of the emitter are less stringent for photonic crystal waveguides than for photonic crystal nanocavities [13]. A very attractive application of quantum dots coupled to a photonic crystal waveguide is the implementation of an on-chip single-photon source.

In this chapter the experimental verification that single quantum dots can be coupled efficiently to the mode of a photonic crystal waveguide is presented. This is done using time-resolved photoluminescence measurements of single quantum dots embedded in photonic crystal waveguides.

6.1 Photonic crystal waveguide samples

The wafer used in the experiment is grown by molecular beam epitaxy on a GaAs substrate. First a 2 μm layer of $Al_{0.7}Ga_{0.3}As$ is grown which can selectively be etched away. On top a 150 nm GaAs membrane layer is grown with a single layer of InAs quantum dots at the center.

The density of quantum dots is $\sim 250\ \mu m^{-2}$ measured by atomic force microscopy. The quantum dots are grown by the same recipe producing the quantum dots shown in figure 2.1. The photoluminescence of the quantum dots has been measured on the unprocessed sample and the emission wavelength of the quantum dot ground states are found to be centered at 960 nm

and with an inhomogeneously broadened spectral width of 50 nm.

Photonic crystal waveguides are formed by leaving out a single row of holes in the triangular lattice of the photonic crystal which is called a W1 waveguide. The W1 waveguide is used due to the effective confinement of the electromagnetic mode and the large slow down factors that can be achieved.

The photonic crystals are fabricated using electron beam lithography followed by dry etching of the holes using electron cyclotron resonance ion etching[1]. This combination creates holes with very small errors in the position and shape and very straight sidewalls which is important for fabricating good photonic crystals. The AlGaAs layer below the GaAs layer is then removed by a wet etch resulting in a freely suspended membranes. In this way a sample with photonic crystal waveguides with different values of the lattice parameter (a) and radius (r) was fabricated. The individual waveguides are ~ 7 μm wide and 100 μm long such that finite size effects can be neglected. The waveguides are also terminated by the unpatterned membrane which reduces reflection from the ends of the waveguide that could result in Fabry-Perot like resonances between the ends.

canning electron micrographs (SEM) of two photonic crystal waveguides are displayed in figure 6.1. The left is a cleaved sample and it clearly shows free hanging photonic crystal membrane. The dark material in the bottom of the picture is the AlGaAs which has been etched away under the photonic crystal to create the membrane. The right image shows another waveguide from the top. This image illustrates the high uniformity of the photonic crystal; both the position of the holes and the hole shape is very regular. This illustrates the state-of-the-art quality of the waveguide samples.

6.2 Calculating the waveguide modes

As discussed in section 2.2.1 a waveguide with periodic boundary conditions can give rise to an enhancement of the emission into the waveguide mode with a Purcell factor that is inversely proportional to the group velocity

[1]The fabrication has mainly been done at DTU Fotonik except for the dry etching which was done at the University of Würzburg.

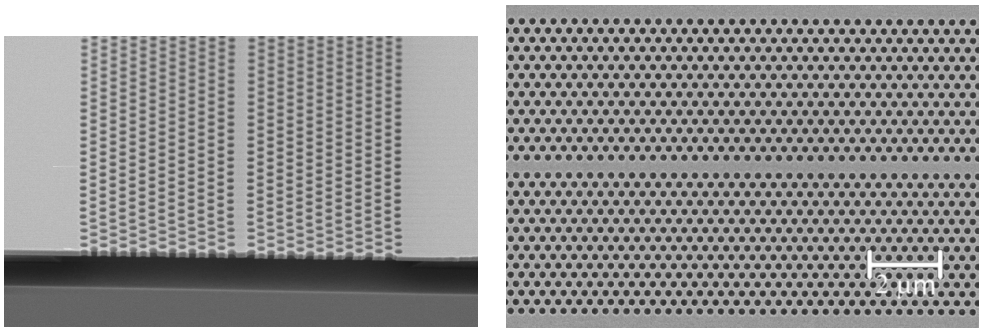

Figure 6.1: Scanning electron micrograph of two photonic crystal waveguides. The left image is a waveguide that has been cleaved to show the free hanging photonic crystal membrane. The waveguide is seen as the row of missing holes in the center of the membrane. The right image is taken from the top for a waveguide with $a = 294$ nm and $r = 87$ nm. The waveguide is clearly visible in the center of the image.

of the mode and the effective mode area (see eq. 2.19). This means that a waveguide should be designed such that the mode area is as small as possible and with a small group velocity. Calculations in the literature [17, 15] shows that a good design to achieve an efficient coupling is a W1 waveguides with a ratio between the radius and lattice parameter of $r/a \sim 0.29$. The value of the lattice parameter should then be chosen such that the slow light regime of the waveguide mode is at the emission wavelength of the emitters.

To find the Purcell factor the mode area and the group velocity must be calculated. This can be done numerically using the MPB software package [93]. The program can solve the Maxwell equations in periodic dielectric structures and in this way calculate the electric fields and dispersion relations of the electromagnetic modes of the structure. From these calculations the group velocity (v_g) and effective mode volume (V_{eff}) can be extracted.

An example of the band structure of a photonic crystal waveguide with a lattice parameter of $a = 256$ nm, a hole radius of $0.286a$ and a membrane thickness of 150 nm is shown in figure 6.2. These are the parameters of one

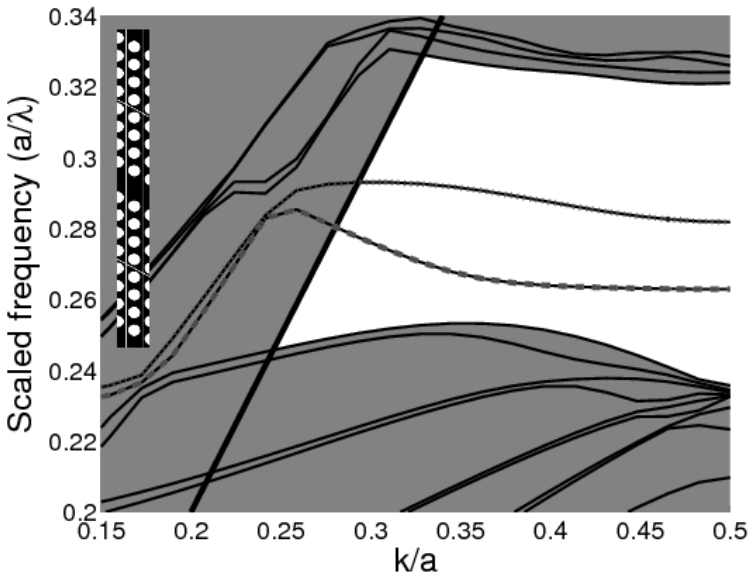

Figure 6.2: The dispersion diagram of the modes of a photonic crystal waveguide with a lattice parameter of $a = 256$ nm, a hole radius of $0.286a$ and a membrane thickness of 150 nm. A refractive index of 3.44 was used corresponding to GaAs at 10 K and a wavelength of 980 nm. The thick black line is the light line and the area above the light line and outside the bandgap is shaded. The dashed (lower) and dotted (upper) bands are the waveguide modes. The upper line is the mode with polarization perpendicular to the waveguide. The lower band is the mode with polarization in the plane of the waveguide and with the lowest group velocity. This is the mode where efficient coupling to the quantum dots is expected and the mode focussed on here. The insert to the left shows a few periods of the unit cell used in the calculations.

of the samples investigated later in the chapter. The unshaded area of the waveguide shows the bandgap of the photonic crystal in the direction of the waveguide. Calculations for a photonic crystal without a waveguide results in a similar band diagram but without the two waveguide modes which are the red and blue lines in the plot. The two waveguide modes have orthogonal polarizations and the slope of the lowest waveguide mode is seen to be very small, which gives a very low group velocity. This is also the mode with a polarization in the plane of the membrane which matches the polarization of the quantum dot ground states. This means that optimal coupling of the quantum dots is expected for this mode and is the one investigated.

From the numerical calculations of the photonic crystal waveguide modes the group velocity is readily found and the effective mode area (A_{eff}) is extracted from the maximum field amplitude of the modes (E), as these are normalized such that $A_{\text{eff}} = a^2/|E|_{\max}$. The calculation shown in figure 6.2 shows that the parameters used are promising for demonstrating coupling of quantum dots to the photonic crystal waveguide.

6.3 Demonstration of coupling of quantum dots to a photonic crystal waveguide

Two of the waveguides on the sample have been used for the experiments in this chapter, one with lattice parameter $a = 248 \pm 2$ nm and radius $r = (0.292 \pm 0.006)a$ and one with $a = 256 \pm 2$ nm and $r = (0.286 \pm 0.006)a$. The pitch and diameter is found from SEM images of the sample and the errors indicate the standard deviation from measurements on more than 20 different holes on the same sample.

The photoluminescence measurements are done using the setup described in chapter 3. The quantum dots are optically excited with pulsed excitation from the Ti:Sapphire laser operating at 800 nm. The sample is mounted in the cryostat perpendicular to the optical axis of the microscope and the excitation and detection is done from the top of the waveguide through the microscope objective. For all the measurements in this chapter the temperature of the cryostat was 10 K.

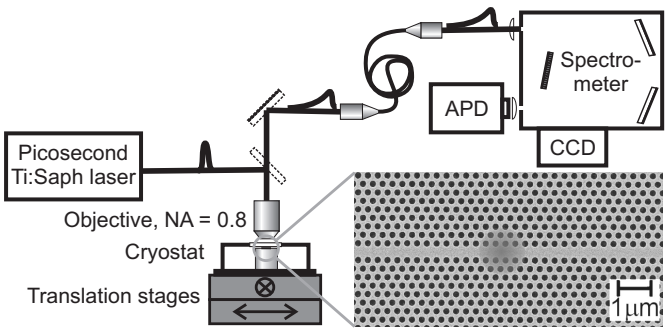

Figure 6.3: A simplified sketch of the setup used for the measurements in this chapter. The SEM image inserted shows a waveguide sample where the red sketched region illustrates the size of the area from which photoluminescence is collected.

The high resolution microscope objective (100X, NA = 0.8) is used to achieve the smallest possible collection area in order to limit the contribution from quantum dots outside the photonic crystal waveguide. With this objective the spatial resolution of the detection is 1.4 μm (as found in section 3.3.1). This should be compared to the size of the waveguide which for a lattice parameter of 256 nm is 370 nm wide. The fraction of the spontaneously emitted photons that couple to radiation modes are collected through the microscope objective and subsequently focussed to the single mode fiber. The output of the fiber is directed to the spectroscopy part of the setup and into the spectrometer as described in section 3.4.

A 600 g/mm grating was used in the spectrometer giving a resolution of 0.06 nm on the CCD. One of the high quantum efficiency APDs (PE) was installed on the output of the spectrometer giving a temporal resolution of 280 ps and the exit slit was set to a detection bandwidth of 0.15 nm.

A simplified sketch of the setup is shown in figure 6.3 along with a SEM image of a waveguide sample where the collection area of the setup is indicated by the red spot. This illustrates that the photons detected are

primarily from the waveguide but also that there is a significant contribution from areas outside the waveguide.

6.3.1 Photoluminescence spectra

The first step in investigating the coupling of the quantum dots to the waveguides is to measure the photoluminescence of the samples. Two examples of photoluminescence spectra recorded at two different positions on the photonic crystal waveguide with $a = 256$ nm are displayed in figure 6.4 and discrete single quantum dot emission lines are observed.

The measurements should be carried out in the low excitation regime below the saturation level of single exciton lines, where predominantly photoluminescence from the quantum dot ground state is observed. To ensure this the photoluminescence spectra as a function of excitation power has been measured. The power dependence is found to be linear up to ~ 60 W/cm^2 and to ensure that emission is primarily from ground state lines an excitation power significantly below this level of 3 W/cm^2 has been used.

The height of the peaks in figure 6.4 reflect that the quantum dot emission is redistributed depending on its position in the photonic crystal membrane and it has been shown that the emission in photonic crystals is enhanced out of plane [94]. In the waveguides this means that dots with a high emission intensity measured out of the plane will not couple to the waveguide while the quantum dots coupling to the waveguide will emit less light due to efficient coupling of the photons into the waveguide mode. In the spectra measured here no any clear signature of the quantum dots coupling to the waveguide is seen. Spectral signatures of quantum dot emission coupled to a photonic crystal waveguide as been reported in [95] but in a transmission geometry. Here time-resolved photoluminescence measurements is instead employed as a way to directly determine the coupling rate of photons from the quantum dot to the photonic crystal waveguide.

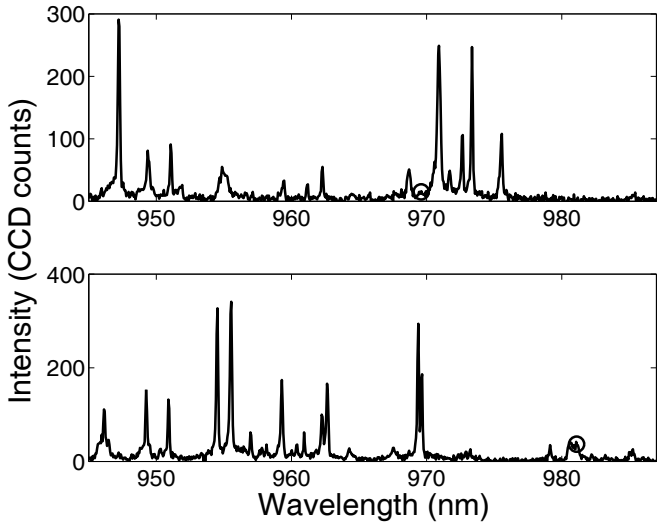

Figure 6.4: Photoluminescence spectra displaying single quantum dot emission lines. The spectra were recorded at two different positions on the photonic crystal waveguide sample with $a = 256$ nm. The excitation density was ~ 3 W/cm^2. The circles in the upper and lower graph are peaks where the decay rates were measured as described in the main text.

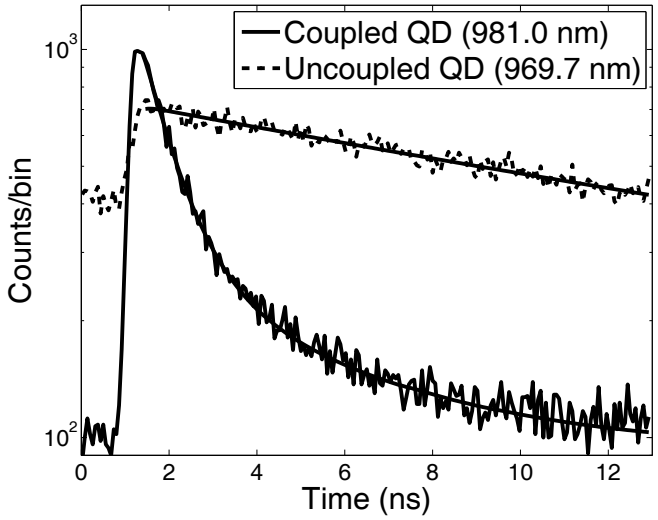

Figure 6.5: Decay curves from two quantum dots in the waveguide with $a = 25$ nm. The solid decay curve is measured at 981.0 nm where the quantum dot is coupled to the photonic crystal waveguide. The dashed decay curve is measured at 969.7 nm and is an example of an uncoupled quantum dot. The decay curves are recorded at the spectral positions marked by the circles in figure 6.4. The solid lines are the fitted single (uncoupled dot) or double (coupled dot) exponential decay models.

6.3.2 Time-resolved measurements

Time-resolved photoluminescence has been recorded on single quantum dot lines at a large number of different emission wavelengths. Two examples of decay curves from the single quantum dot lines in figure 6.4 are displayed in figure 6.5. The two decay curves reveal very different quantum dot dynamics. One of the decay curves displays a very slow single exponential decay with a rate of 0.05 ns^{-1}. This decay curve corresponds to a quantum dot that is not coupled to the photonic crystal waveguide. This can be due to spatial mismatch relative to the photonic crystal waveguide or that the quantum dot dipole moment is oriented along the photonic crystal waveguide axis [17]. The decay rate of the uncoupled quantum dot is inhibited by a factor ~ 20 compared to a quantum dot in a homogeneous medium, which is an effect of the 2D photonic bandgap of the photonic crystal membrane [94, 96]. The decay from the other quantum dot in figure 6.5 is much faster due to coupling to the waveguide mode. The fast decay curve is well described by a double exponential model, where the fast component is the rate due to coupling to the waveguide, while the slow component contains contributions from other quantum dot emission lines and dark exciton recombination in the quantum dot [97, 23]. Note that a weak slow component of the decay rate will also contribute to the decay curve of the uncoupled quantum dot, however in this case it cannot be distinguished from the inhibited decay, and a single-exponential model is sufficient to model the decay. For the fast decay curve displayed in figure 6.5 a fast decay rate of 1.34 ns^{-1} is derived for the quantum dot coupled to the waveguide. Consequently the coupled quantum dot decays 27 times faster than the uncoupled quantum dot and faster than a quantum dot in bulk material, where the decay rate of the ground state is 1.1 ns^{-1}. This demonstrates that photons can be channeled very efficiently into the photonic crystal waveguide.

As described above the slowly decaying quantum dots can be successfully modeled by a single exponential decay but a double exponential model is needed for the fast decaying dots coupling to the waveguide. Intermediate cases are also expected as the decay rate for different positions and polarizations of the quantum dots will range from the decay rates in a photonic

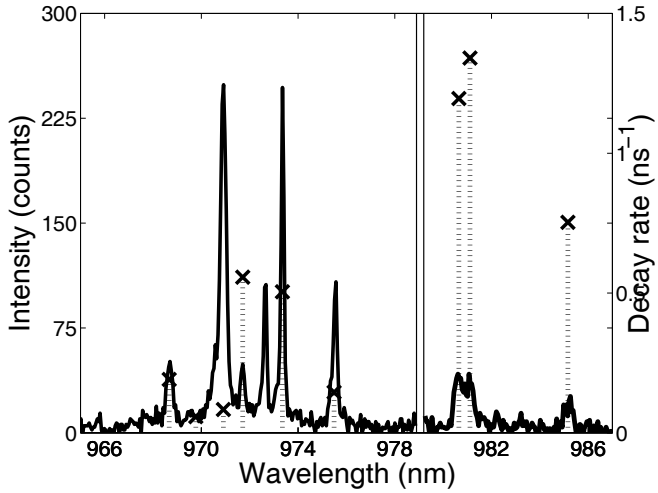

Figure 6.6: A section of photoluminescence emission spectra from figure 6.4 along with the fitted fast decay rates of the quantum dot lines. The crosses indicate the measured decay rates (right axis) of the different quantum dot emission lines.

crystal to perfect coupling to the waveguide. Fitting single exponentially decaying data with a double exponential model has the problem that the fitting routine often finds a minimum where the second decay rate fits to random noise of the data. This can give very large or negative second decay rates which in turn obscures the value of the real fast decay rate. To quantify the selection between single and double exponential decays all of the measured quantum dot decay curves was initially fitted with a single-exponential decay model. For each decay the reduced χ^2 is calculated and curves with a value larger than 1.3 is fitted with a double-exponential decay model instead.

A selection of the fitted decay rates for two positions on the waveguide is shown along with the associated spectrum in figure 6.6. The figure shows the difficulty of finding the quantum dots coupling to the waveguide from

the spectra as there is no obvious correlation between the height and the decay rate. However, the highest peaks are always found to decay slow as will be further discussed below.

6.3.3 Decay rate as a function of emission frequency

The complete set of in total 26 measured decay rates on the sample with $a = 256$ nm is shown in figure 6.7. Here the measured decay rates are plotted as a function of scaled frequency a/λ, where λ is the emission wavelength. When modeling the data, in most cases single-exponential decay curves suffices, while only for the fastest decay curves a bi-exponential model was needed. We observe a range of decay rates since differently positioned and oriented quantum dots couple differently to the waveguide, as discussed above. The data are seen to fall into two groups where the decay rates are above and below ~ 0.3 ns^{-1} corresponding to uncoupled and coupled quantum dots, respectively. Fast decay rates are only observed in a limited range of scaled frequencies (a/λ), which is in very good agreement with expectations from theory where the most efficient coupling to the photonic crystal waveguide is expected when the quantum dot can couple to a slowly propagating mode.

To show that the fast decay rates are due to the coupling to the waveguide the theoretical frequency dependence of the decay rate has been calculated for a quantum dot positioned in the center of the photonic crystal waveguide using eq. 2.19 and the mode calculations described in section 6.2. The parameters of the calculation in figure 6.2 was used and the decay rate of the quantum dots in a homogeneous material (Γ_0) is 1.1 ns^{-1} which has been measured for quantum dots outside the waveguide structures.

In figure 6.7 the resulting calculated decay rates (red line) are plotted assuming no adjustable parameters. A discrepancy of only 1 % is found between the frequency of enhanced decay rates in the measurement and the point of divergence of the calculated decay rate. The main uncertainty in the calculated decay rate originating from the uncertainty in the lattice parameter (a) is illustrated in figure 6.7 by the hatched area. Anticipating the additional uncertainty in hole radius (r) and refractive index (n), and the

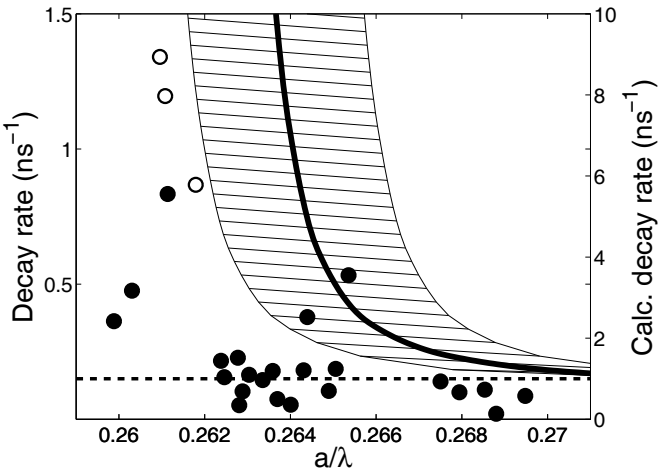

Figure 6.7: Measured quantum dot decay rates on the photonic crystal waveguide sample with $a = 256$ nm as a function of scaled frequency. The excitation power for these measurements was 3 W/cm^2. The data points marked by open circles are modeled using a double exponential decay model and the filled circles are modeled using a single exponential model. The solid line (right axis) are decay rates calculated from numerical simulations with uncertainties in a of ± 2 nm given by the hatched area. The dotted line is the mean decay rate of uncoupled quantum dots used for the estimation of the β-factor.

numerical uncertainty of the calculation, we conclude that there is an excellent match regarding the range of scaled frequencies where enhanced rates are observed. This clearly proves that the enhancement is due to coupling to the photonic crystal waveguide.

The measured decay rates are found to be approximately 8 times smaller than the calculated decay rates. A lower decay rate is expected as the theory assumes a dipole emitter positioned and oriented optimally with respect to the photonic crystal waveguide. In addition the model does not take into account imperfections giving rise to scattering losses. These are known to limit the achievable group velocity slow-down factor and removing the divergence of the decay rate [35].

To ensure that the increase in the decay rates are not due to the edge of the photonic crystal bandgap the decay rates of quantum dots in a photonic crystal membrane with $a = 256$ nm, $r = 0.286a$ and without a photonic crystal waveguide have been measured. The resulting decay rates are shown in figure 6.8. An increase in the decay rate in observed due to the band edge at $a/\lambda = 0.254$, which distinctly differs from the scaled frequency where the photonic crystal waveguide coupling is observed. To illustrate this the scaled frequency where the optimum coupling is observed is shown by the green dashed line in figure 6.8. Furthermore, the position of the band edge matches the value found from the band structure calculation of 0.253, marked by the black line, very well. Below the band edge the quantum dot decay rates are observed to increase to around 1 ns^{-1} while inside the 2D band gap decay rates between 0.05 ns^{-1} and 0.43 ns^{-1} are observed. The observed fluctuations reflect the dependence of the projected local density of optical states on the quantum dot orientation and position. The measurements can be compared to the calculations of Koenderink et al. [96], where inhibition factors between 0.03 and 0.39 are predicted in the respective energy range of the 2D band gap.

Another photonic crystal waveguide with lattice parameter $a = 248$ nm has been investigated to collect further experimental evidence of coupling to the waveguide. For this waveguide the slow light regime, where efficient coupling to the photonic crystal waveguide occurs, matches the excited state of the quantum dots. Consequently these measurements were performed in

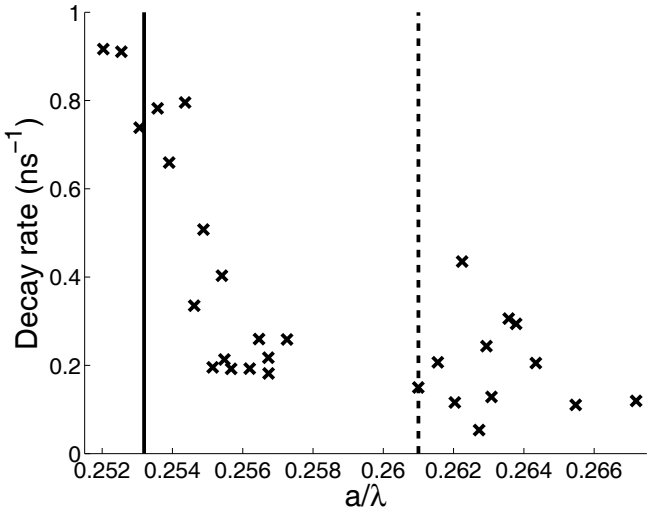

Figure 6.8: Measured decay rates on a photonic crystal sample with $a = 256$ nm, $r = 0.286a$ and without a waveguide. The dashed line is the emission wavelength of the maximum coupling quantum dot from figure 6.7. The solid line at a scaled frequency of 0.253 is the calculated band edge of the photonic crystal.

the highly saturated regime where photoluminescence from the quantum dot excited states is observed. The data are presented in figure 6.9. Once again the data fall into two groups, in this case below and above ~ 0.5 ns^{-1}, of slow and fast rates corresponding to uncoupled and coupled quantum dots, respectively. The rates of the uncoupled quantum dots are relatively fast, since the excited states are known to have increased non-radiative decay compared to the ground state excitons. Strong enhancement is observed in this case for $a/\lambda = 0.263$, which matches theory very well. We observe enhanced rates of up to 3.5 ns^{-1} clearly demonstrating the very pronounced effect of the photonic crystal waveguide.

6.3.4 Coupling efficiency

The figure of merit determining the coupling efficiency into the photonic crystal waveguide is the β-factor defined in eq. 2.22. In case of the photonic crystal waveguide samples it can be written as

$$\beta = \frac{\Gamma_{\mathrm{wg}}}{\Gamma_{\mathrm{wg}} + \gamma_{\mathrm{rad}} + \gamma_{\mathrm{nr}}}, \tag{6.1}$$

where Γ_{wg} is the decay rate of the quantum dot to the photonic crystal waveguide mode, γ_{rad} is the radiative decay rate to non-guided modes, and γ_{nr} is the intrinsic quantum dot non-radiative decay rate [23]. The total decay rate of the uncoupled dots $\Gamma_{\mathrm{tot}} \equiv \gamma_{\mathrm{rad}} + \gamma_{\mathrm{nr}}$ can be extracted from the measurements on quantum dots that do not couple to the photonic crystal waveguide. The decay rate to non-guided modes will depend on position and orientation of the individual quantum dot [17, 96], which is reflected in the variations in the decay rates of the uncoupled quantum dots in figure 6.7 and 6.9. To accommodate this the average total decay rate of the uncoupled quantum dots is extracted, which is $\Gamma_{\mathrm{tot}}(a = 248\ \mathrm{nm}) = 0.4$ ns^{-1} and $\Gamma_{\mathrm{tot}}(a = 256\ \mathrm{nm}) = 0.15$ ns^{-1} for the two data sets, respectively. These values are marked by the green dotted line in figure 6.7 and 6.9.

In figure 6.10 the calculated β-factor is plotted versus scaled frequency. β-factors of up to 0.89 are observed, demonstrating the excellent photon

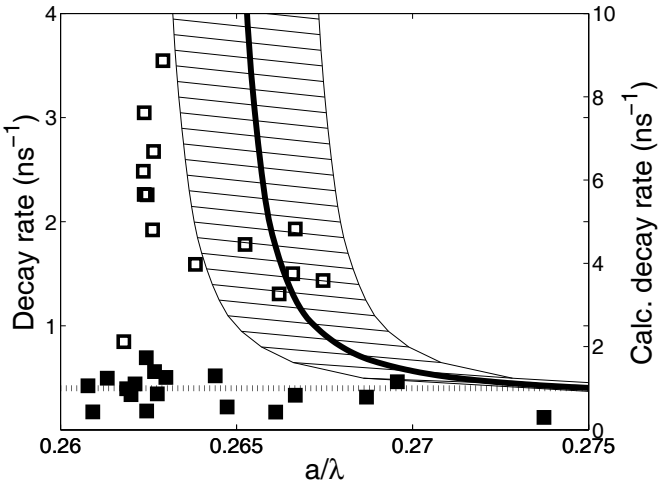

Figure 6.9: Measured decay rates for quantum dots in a photonic crystal waveguide sample with $a = 248$ nm and $r = 0.292a$. The excitation power was 1.5 kW/cm^2. The data points marked by open (filled) squares are modeled using a double (single) exponential decay model. The solid line (right axis) are decay rates calculated from numerical simulations with uncertainties in a of ± 2 nm given by the hatched area. The dotted line is the mean decay rate of uncoupled quantum dots used for the estimation of β in section 6.3.4.

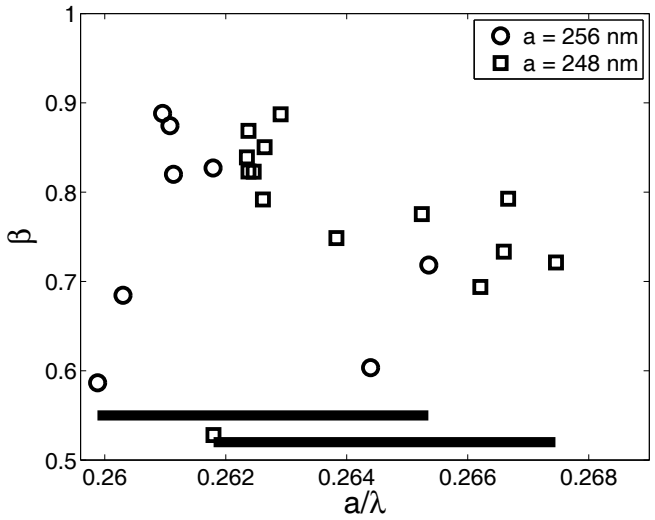

Figure 6.10: The β-factors above 0.5 calculated from the data in figure 6.7 (circles) and figure 6.9 (squares) as described in the text. The bars shows the coupling bandwidth of the photonic crystal waveguide sample with $a = 256$ nm (left) and $a = 248$ nm (right).

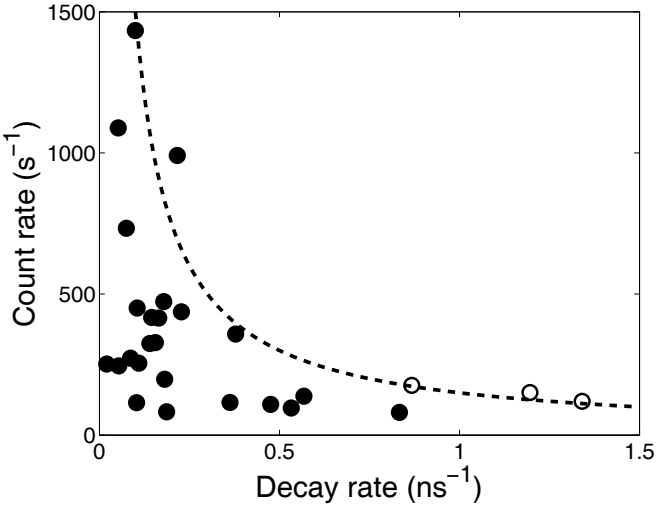

Figure 6.11: The count rate on the APD of the quantum dot lines as function of the measured decay rate of the photonic crystal waveguide with $a = 256$ nm. The dashed line is described in the main text.

collection efficiency of photonic crystal waveguides. Even more spectacularly, a β-factor above 0.5 is observed in a relative bandwidth as large as 2 % corresponding to 20 nm for both photonic crystal waveguide samples. This superior bandwidth is unique for a photonic crystal waveguide. For comparison a β-factor of 0.92 limited to a relative bandwidth of 0.3 % has been demonstrated in photonic crystal cavities [88] and a β-factor of 0.9 in a relative bandwidth less than $\cdot 10^{-4}$ was found for the micropillars in chapter 4. This demonstrates the important advantage of photonic crystal waveguides for high-efficiency large bandwidth single-photon sources.

The light emitted into the waveguides used in this work will be guided in two directions effectively reducing the β-factor by 2, this can, however, easily be solved by terminating one end of the waveguide [35].

The better the quantum dots couple to the waveguide the more of the

emission is channeled into the waveguide mode due to the increase in β-factor. This will result in a decrease of the measured signal. To quantify this a simple model can be constructed where the detected emission out of plane is proportional to the total emission not going into the waveguide mode. The count rate (CR) as a function of decay rate is then given by

$$CR = N\eta(1-\beta) = N\eta(1-\frac{\Gamma_{\text{tot}}-\Gamma_{\text{uc}}}{\Gamma_{\text{tot}}}) = N\eta\frac{\Gamma_{\text{uc}}}{\Gamma_{\text{tot}}}, \tag{6.2}$$

where Γ_{uc} is the total decay rate of the uncoupled quantum dot in the photonic crystal. The count rate on the detector is then inversely proportional to the decay rate. To explore this the count rate as a function of the decay rate for the measurements on the photonic crystal waveguide with $a = 256$ nm is shown in figure 6.11. The plot clearly shows that the slow quantum dot lines are the ones with the largest count rate and the opposite. The model of eq. 6.2 is plotted as the dashed line in the figure for a value of $N\eta\Gamma_{\text{uc}} = 150$ ns^{-1}. The data follow this trend further supporting that the quantum dots couple to the waveguide mode. The model does not take into account the complex emission pattern of the photonic crystal waveguide and the proportionality constant is difficult to interpret.

To prove that the quantum dots in the waveguides are indeed single-photon sources the HBT signal should be measured. This has been done on a line coupling to a waveguide but no reduction of the central peak was seen. This is not unexpected as the emission perpendicular to the wafer is small due to the coupling of the quantum dots to the waveguide mode. This results in a large background relative to the emission from the quantum dot. Another problem is that the excitation is done above the GaAs bandgap as 800 nm which was shown to obscure the single-photon emission of the micropillars in chapter 5.

6.4 Conclusion and outlook

It was experimentally demonstrated for the first time that spontaneous emission from single quantum dots can be coupled very efficiently to a photonic

crystal waveguide. Quantum dots that couple to a photonic crystal waveguide was found to decay up to 27 times faster than uncoupled quantum dots and the scaled frequency range over which the enhancement was observed is in excellent agreement with the calculated value using recent theoretical proposals taking into account that the light-matter coupling is strongly enhanced due to the significant slow-down of light in the photonic crystal waveguides.

A β-factor as high as 0.89 and an unprecedented large bandwidth of 20 nm has been obtained, in this respect outperforming the traditional quantum dot single-photon source approach based on narrow bandwidth cavities. This shows the promising potential of photonic crystal waveguides for efficient single-photon sources.

This work is an important step toward using single-photon sources based on photonic crystal waveguides. The next mayor challenge for using photonic crystal waveguide based single-photon sources is the output coupling of the photon. This could be done by expanding the waveguide mode to match the mode of a single mode fiber which has a mode diameter that is more than a factor of 10 larger than the mode of the waveguides investigated here. This could either be done in the photonic crystal or by a regular dielectric waveguide.

The slow down factor is mediated by the dispersion control provided by the photonic crystal waveguide and further work should be done to design waveguides where the coupling is optimized. Another interesting aspect is the limitation on the coupling due to the fabrication imperfections of the photonic crystal waveguide.

Recently the coupling has also been demonstrated by tuning a single quantum dot across the photonic crystal waveguide mode utilizing the same technique of temperature tuning as used with the micropillar cavities in chapter 4 [98]. This makes it possible to do a more careful comparison to theory and get a better understanding of the possibilities of single-photon sources based on quantum dots in photonic crystal waveguides.

Chapter 7

Conclusion

Two candidates for an efficient single-photon source based on quantum dots in nanophotonic structures were investigated using time-resolved photoluminescence spectroscopy.

The first approach was a quantum dot in a micropillar cavity. The spectra and decay rate of the quantum dot was measured as a function of the detuning to the cavity mode and an enhancement factor of 10 was seen for the the decay rate when tuned into resonance with the cavity. To interpret the data a model describing the interaction of a two-level system with a cavity, which includes dephasing was derived. Using this model a coherent understanding of the interaction of the quantum dot in the micropillar was achieved and the coupling strength and limits on the dephasing rate were derived.

The single-photon emission was further investigated by measuring the single-photon statistics and the photon indistinguishable of the emission from the micropillar cavities. A multi-photon contribution of only 13% was found and this residual emission was investigated for various detunings and pump powers. A photon indistinguishability of 61% was measured from the micropillar cavities and the value was found to be compatible with the dephasing from the measurements of the decay rate.

The comparison of the theoretical model with the measurements of the

spectra, decay rates, single-photon emission, and indistinguishability gives for the first time a consistent picture of the interaction and single-photon emission of quantum dots in micropillar cavities.

The potential of using a quantum dot in a photonic crystal waveguide as an efficient single-photon source was also investigated and it was found that a high coupling efficiency could be achieved in a very large bandwidth compared to other efficient single-photon sources. This coupling was demonstrated for the first time and illustrates the the potential of photonic crystal waveguide based single-photon sources. The coupling was also compared to theoretical calculations and the frequency dependence was found to be in excellent agreement with theory.

Bibliography

[1] Brahim Lounis and Michel Orrit. Single-photon sources. *Reports on Progress in Physics*, 68(5):1129–1179, 2005.

[2] E. Knill, R. Laflamme, and G. J. Milburn. A scheme for efficient quantum computation with linear optics. *Nature*, 409:46–52, 2001.

[3] C. H. Bennet and G. Brassard. Quantum cryptography: Public key distribution and coin tossing. In *Proceedings of the IEEE International Conference on Computers, Systems, and Signal Processing, Bangalore*, page 175, 1984.

[4] Edo Waks, Kyo Inoue, Charles Santori, David Fattal, Jelena Vuckovic, Glenn S. Solomon, and Yoshihisa Yamamoto. Secure communication: Quantum cryptography with a photon turnstile. *Nature*, 420:762, 2002.

[5] Alan Migdall and Jonathan Dowling, editors. *Single-photon: detectors, applications, and measurement methods Proceedings of the NIST-ARDA Workshop on Single-photon: detectors, applications and measurement methods NIST, Gaithersburg, MD*, volume 51 of *Journal of Modern Optics*, 2003.

[6] P. Michler, A. Kiraz, C. Becher, W. V. Schoenfeld, P. M. Petroff, L. Zhang, E. Hu, and A. Imamoğlu. A quantum dot single-photon turnstile device. *Science*, 290:2282–2285, December 2000.

[7] Charles Santori, Matthew Pelton, Glenn Solomon, Yseulte Dale, and Yoshihisa Yamamoto. Triggered single photons from a quantum dot. *Physical Review Letters*, 86(8):1502–1505, Feb 2001.

[8] C. Santori, D. Fattal, J. Vučković, G. S. Solomon, and Y. Yamamoto. Indistinguishable photons from a single-photon device. *Nature*, 419:594–597, October 2002.

[9] Stefan Strauf, Nick G. Stoltz, Matthew T. Rakher, Larry A. Coldren, Pierre M. Petroff, and Dirk Bouwmeester. High-frequency single-photon source with polarization control. *Nature Photonics*, 1:704–708, 2007.

[10] G. S. Solomon, M. Pelton, and Y. Yamamoto. Single-mode spontaneous emission from a single quantum dot in a three-dimensional microcavity. *Physical Review Letters*, 86(17):3903–3906, Apr 2001.

[11] A. Kress, F. Hofbauer, N. Reinelt, M. Kaniber, H. J. Krenner, R. Meyer, G. Bohm, and J. J. Finley. Manipulation of the spontaneous emission dynamics of quantum dots in two-dimensional photonic crystals. *Physical Review B*, 71(24):241304, 2005.

[12] Dirk Englund, David Fattal, Edo Waks, Glenn Solomon, Bingyang Zhang, Toshihiro Nakaoka, Yasuhiko Arakawa, Yoshihisa Yamamoto, and Jelena Vuckovic. Controlling the spontaneous emission rate of single quantum dots in a two-dimensional photonic crystal. *Physical Review Letters*, 95(1):013904, 2005.

[13] K. Hennessy, A. Badolato, M. Winger, D. Gerace, M. Atatüre, S. Gulde, S. Fält, E. L. Hu, and A. Imamoğlu. Quantum nature of a strongly coupled single quantum dot-cavity system. *Nature*, 445(7130):896–899, Feb 2007.

[14] S. Hughes. Enhanced single-photon emission from quantum dots in photonic crystalwaveguides and nanocavities. *Optics Letters*, 29(22):2659–2661, 2004.

[15] V. S. C. Manga Rao and S. Hughes. Single quantum-dot purcell factor and beta factor in a photonic crystal waveguide. *Physical Review B*, 75(20):205437, 2007.

[16] V. S. C. Manga Rao and S. Hughes. Single quantum dot spontaneous emission in a finite-size photonic crystal waveguide: Proposal for an efficient "on chip" single photon gun. *Physical Review Letters*, 99(19):193901, 2007.

[17] G. Lecamp, P. Lalanne, and J. P. Hugonin. Very large spontaneous-emission beta factors in photonic-crystal waveguides. *Physical Review Letters*, 99(2):023902, 2007.

[18] I. Friedler, C. Sauvan, J. P. Hugonin, P. Lalanne, J. Claudon, and J. M. Gérard. Solid-state single photon sources: the nanowire antenna. *Optics Express*, 17(4):2095–2110, 2009.

[19] J. Johansen. *Decay dynamics of quantum dots in nanophotonic structures*. PhD thesis, DTU Fotonik, Technical University of Denmark, 2008.

[20] Manfred Bayer. *Single Quantum Dot, Fundamentals, Applications and New Concepts*, chapter Exciton Complexes in Sel-Assembled In(Ga)As/GaAs Quantum Dots, pages 93–146. Springer, 2003.

[21] D. Schuh, J. Bauer, E. Uccelli, R. Schulz, A.Kress, F. Hofbauer, J.J. Finley, and G. Abstreiter. Controlled positioning of self-assembled InAs quantum dots on (110) GaAs. *Physica E*, 26:72–76, 2005.

[22] C. Schneider, M. Strauss, T. Sunner, A. Huggenberger, D. Wiener, S. Reitzenstein, M. Kamp, S. Hofling, and A. Forchel. Lithographic alignment to site-controlled quantum dots for device integration. *Applied Physics Letters*, 92(18):183101, 2008.

[23] Jeppe Johansen, Søren Stobbe, Ivan S. Nikolaev, Toke Lund-Hansen, Philip T. Kristensen, Jørn M. Hvam, Willem L. Vos, and Peter Lodahl. Size dependence of the wavefunction of self-assembled inas quan-

tum dots from time-resolved optical measurements. *Physical Review B*, 77:073303, 2008.

[24] K. L. Silverman, R. P. Mirin, S. T. Cundiff, and A. G. Norman. Direct measurement of polarization resolved transition dipole moment in InGaAs/GaAs quantum dots. *Applied Physics Letters*, 82(25):4552–4554, 2003.

[25] P. Borri, W. Langbein, S. Schneider, U. Woggon, R. L. Sellin, D. Ouyang, and D. Bimberg. Ultralong dephasing time in ingaas quantum dots. *Physical Review Letters*, 87(15):157401, Sep 2001.

[26] M. Bayer and A. Forchel. Temperature dependence of the exciton homogeneous linewidth in $In_{0.60}Ga_{0.40}As/GaAs$ self-assembled quantum dots. *Physical Review B*, 65(4):041308, Jan 2002.

[27] C. Kammerer, C. Voisin, G. Cassabois, C. Delalande, Ph. Roussignol, F. Klopf, J. P. Reithmaier, A. Forchel, and J. M. Gérard. Line narrowing in single semiconductor quantum dots: Toward the control of environment effects. *Physical Review B*, 66(4):041306, Jul 2002.

[28] B. Urbaszek, E. J. McGhee, M. Krüger, R. J. Warburton, K. Karrai, T. Amand, B. D. Gerardot, P. M. Petroff, and J. M. Garcia. Temperature-dependent linewidth of charged excitons in semiconductor quantum dots: Strongly broadened ground state transitions due to acoustic phonon scattering. *Physical Review B*, 69(3):035304, Jan 2004.

[29] Marlan O. Scully and M. Suhail Zubairy. *Quantum Optics*. Cambridge University Press, 1997.

[30] Kwang Jun Ahn and Andreas Knorr. Radiative lifetime of quantum confined excitons near interfaces. *Physical Review B*, 68(16):161307, Oct 2003.

[31] Søren Stobbe, Jeppe Johansen, Philip Trøst Kristensen, Jørn M. Hvam, and Peter Lodahl. Frequency dependence of the radiative decay rate

of excitons in self-assembled quantum dots: experiment and theory. *arXiv:0902.0344v1*.

[32] E. M. Purcell. *Physical Review*, 69:681, 1946.

[33] Susumu Noda, Masayuki Fujita, and Takashi Asano. Spontaneous-emission control by photonic crystals and nanocavities. *Nature Photonics*, 1:449 – 458, 2007.

[34] Daniel Kleppner. Inhibited spontaneous emission. *Physical Review Letters*, 47(4):233–236, 1981.

[35] S. Hughes, L. Ramunno, Jeff F. Young, and J. E. Sipe. Extrinsic optical scattering loss in photonic crystal waveguides: Role of fabrication disorder and photon group velocity. *Physical Review Letters*, 94(3):033903, Jan 2005.

[36] Eli Yablonovitch. Inhibited spontaneous emission in solid-state physics and electronics. *Physical Review Letters*, 58(20):2059–2062, May 1987.

[37] Eli Yablonovitch. Inhibited spontaneous emission in solid-state physics and electronics. *Physical Review Letters*, 58:2059–2062, 1987.

[38] Judith E.G.J. Wijnhoven and Willem L. Vos. Preparation of Photonic Crystals Made of Air Spheres in Titania. *Science*, 281(5378):802–804, 1998.

[39] K.M. Ho, C.T. Chan, C.M. Soukoulis, R. Biswas, and M. Sigalas. Photonic band gaps in three dimensions: New layer-by-layer periodic structures. *Solid State Communications*, 89(5):413 – 416, 1994.

[40] Minghao Qi, Elefterios Lidorikis, Peter T. Rakich, Steven G. Johnson, J. D. Joannopoulos, Erich P. Ippen, and Henry I. Smith. A three-dimensional optical photonic crystal with designed point defects. *Nature*, 429:538, 2004.

[41] Peter Lodahl, A. Floris van Driel, Ivan S. Nikolaev, Arie Irman, Karin Overgaag, Daniel Vanmaekelbergh, and Willem L. Vos. Controlling the dynamics of spontaneous emission from quantum dots by photonic crystals. *Nature*, 430(7000):654–657, 2004.

[42] R. J. Thompson, G. Rempe, and H. J. Kimble. Observation of normal-mode splitting for an atom in an optical cavity. *Physical Review Letters*, 68(8):1132–1135, Feb 1992.

[43] C. Weisbuch, M. Nishioka, A. Ishikawa, and Y. Arakawa. Observation of the coupled exciton-photon mode splitting in a semiconductor quantum microcavity. *Physical Review Letters*, 69(23):3314–3317, Dec 1992.

[44] J. P. Reithmaier, G. Sek, A. Löffler, C. Hofmann, S. Kuhn, S. Reitzenstein, L. V. Keldysh, V. D. Kulakovskii, T. L. Reinecke, and A. Forchel. Strong coupling in a single quantum dot-semiconductor microcavity system. *Nature*, 432(7014):197–200, Nov 2004.

[45] T. Yoshie, A. Scherer, J. Hendrickson, G. Khitrova, H. M. Gibbs, C. Ell G. Rupper, O. B. Shchekin, and D. G. Deppe. Vacuum rabi splitting with a single quantum dot in a photonic crystal nanocavity. *Nature*, 432:200, 2004.

[46] E. Peter, P. Senellart, D. Martrou, A. Lemaître, J. Hours, J. M. Gérard, and J. Bloch. Exciton-photon strong-coupling regime for a single quantum dot embedded in a microcavity. *Physical Review Letters*, 95(6):067401, Aug 2005.

[47] Guoqiang Cui and M. G. Raymer. Emission spectra and quantum efficiency of single-photon sources in the cavity-qed strong-coupling regime. *Physical Review A*, 73(5):053807, 2006.

[48] H. J. Carmichael, R. J. Brecha, M. G. Raizen, H. J. Kimble, and P. R. Rice. Subnatural linewidth averaging for coupled atomic and cavity-mode oscillators. *Physical Review A*, 40(10):5516–5519, Nov 1989.

[49] R. Hanbury-Brown and R. Q. Twiss. A test of a new type of stellar interferometer on sirius. *Nature*, 178:1046–1048, 1956.

[50] H. J. Kimble, M. Dagenais, and L. Mandel. Photon antibunching in resonance fluorescence. *Physical Review Letters*, 39(11):691–695, Sep 1977.

[51] P. Michler, A. Imamoglu, M. D. Mason, P. J. Carson, G. F. Strouse, and S. K. Buratto. Quantum correlation among photons from a single quantum dot at room temperature. *Nature*, 406:968 – 970, 2000.

[52] R. Loudon. *The Quantum Theory of Light*. Oxford University Press, 3rd edition, 2000.

[53] C. K. Hong, Z. Y. Ou, and L. Mandel. Measurement of subpicosecond time intervals between two photons by interference. *Physical Review Letters*, 59(18):2044–2046, Nov 1987.

[54] J. Bylander, I. Robert-Philip, and I. Abram. Interference and correlation of two independent photon. *European Physical Journal D*, 22:295–301, 2003.

[55] C. J. R. Sheppard and C. J. Cogswell. Effects oo aberrating layers and tube length on confocal imaging properties. *Optik*, 87:34–38, 1991.

[56] A. N. Vamivakas, S. B. Ippolito, A. K. Swan, M. S. Ünlü, M. Dogan, E. R. Behringer, and B. B. Goldberg. Phase-sensitive detection of dipole radiation in a fiber-based high numerical aperture optical system. *Optics Letters*, 32(8):970–972, 2007.

[57] E. Moreau, I. Robert, L. Manin, V. Thierry-Mieg, J. M. Gérard, and I. Abram. Quantum cascade of photons in semiconductor quantum dots. *Physical Review Letters*, 87(18):183601, Oct 2001.

[58] M. Kaniber, A. Laucht, A. Neumann, J. M. Villas-Bôas, M. Bichler, M.-C. Amann, and J. J. Finley. Investigation of the nonresonant dot-cavity coupling in two-dimensional photonic crystal nanocavities. *Physical Review B*, 77(16):161303, 2008.

[59] V. Sandoghdar, F. Treussart, J. Hare, V. Lefèvre-Seguin, J. M. Raimond, and S. Haroche. Very low threshold whispering-gallery-mode microsphere laser. *Physical Review A*, 54(3):R1777–R1780, Sep 1996.

[60] V. B. Braginsky, M. L. Gorodetsky, and V. S. Ilchenko. Quality-factor and nonlinear properties of optical whispering-gallery modes. *Physics Letters A*, 137(7-8):393 – 397, 1989.

[61] N. Le Thomas, U. Woggon, O. Schops, M. V. Artemyev, M. Kazes, and U. Banin. Cavity qed with semiconductor nanocrystals. *Nano Letters*, 6(3):557–561, 2006.

[62] D. K. Armani, T. J. Kippenberg, S. M. Spillane, and K. J. Vahala. Ultra-high-Q toroid microcavity on a chip. *Nature*, 412:925–928, 2003.

[63] B. Gayral, J. M. Gérard, A. Lemaitre, C. Dupuis, L. Manin, and J. L. Pelouard. High-Q wet-etched GaAs microdisks containing inas quantum boxes. *Applied Physics Letters*, 75(13):1908–1910, 1999.

[64] Bumki Min, Eric Ostby, Volker Sorger, Erick Ulin-Avila, Lan Yang, Xiang Zhang, and Kerry Vahala. High-Q surface-plasmon-polariton whispering-gallery microcavity. *Nature*, 457:455–458, 2009.

[65] Gunnar Björk, Susumu Machida, Yoshihisa Yamamoto, and Kazuhiro Igeta. Modification of spontaneous emission rate in planar dielectric microcavity structures. *Physical Review A*, 44(1):669–681, Jul 1991.

[66] D. G. Gevaux, A. J. Bennett, R. M. Stevenson, A. J. Shields, P. Atkinson, J. Griffiths, D. Anderson, G. A. C. Jones, and D. A. Ritchie. Enhancement and suppression of spontaneous emission by temperature tuning inas quantum dots to photonic crystal cavities. *Applied Physics Letters*, 88(13):131101, 2006.

[67] Sylvain Combrié, Alfredo De Rossi, Quynh Vy Tran, and Henri Benisty. GaAs photonic crystal cavity with ultrahigh Q: microwatt nonlinearity at 1.55 μm. *Optics Letters*, 33(16):1908–1910, 2008.

[68] Nguyen-Vi-Quynh Tran, Sylvain Combrie, and Alfredo De Rossi. Directive emission from high-q photonic crystal cavities through band folding. *Physical Review B*, 79(4):041101, 2009.

[69] J. M. Gérard, B. Sermage, B. Gayral, B. Legrand, E. Costard, and V. Thierry-Mieg. Enhanced spontaneous emission by quantum boxes in a monolithic optical microcavity. *Physical Review Letters*, 81(5):1110–1113, Aug 1998.

[70] E. Moreau, I. Robert, J. M. Gerard, I. Abram, L. Manin, and V. Thierry-Mieg. Single-mode solid-state single photon source based on isolated quantum dots in pillar microcavities. *Applied Physics Letters*, 79(18):2865–2867, 2001.

[71] Jelena Vŭcković, David Fattal, Charles Santori, Glenn S. Solomon, and Yoshihisa Yamamoto. Enhanced single-photon emission from a quantum dot in a micropost microcavity. *Applied Physics Letters*, 82(21):3596–3598, 2003.

[72] A. Löffler, J. P. Reithmaier, G. Sęk, C. Hofmann, S. Reitzenstein, M. Kamp, and A. Forchel. Semiconductor quantum dot microcavity pillars with high-quality factors and enlarged dot dimensions. *Applied Physics Letters*, 86(11):111105, 2005.

[73] S. Reitzenstein, N. Gregersen, C. Kistner, M. Strauss, C. Schneider, L. Pan, T. R. Nielsen, S. Höfling, J. Mørk, and A. Forchel. Oscillatory variations in the Q factors of high quality micropillar cavities. *Submitted to Appl. Phys. Lett.*, 2009.

[74] Lucio Claudio Andreani, Giovanna Panzarini, and Jean-Michel Gérard. Strong-coupling regime for quantum boxes in pillar microcavities: Theory. *Physical Review B*, 60(19):13276–13279, Nov 1999.

[75] C. Kistner and S. Reitzenstein. University of würzburg. Personal communication.

[76] W.L. Barnes, G. Björk, J.M. Gérard, P. Jonsson, J.A.E. Wasey, P.T. Worthing, and V. Zwiller. Solid-state single photon sources: light collection strategies. *The European Physical Journal D*, 18:197, 2002.

[77] C. Kistner, T. Heindel, C. Schneider, A. Rahimi-Iman, S. Reitzenstein, S. Höfling, and A. Forchel. Demonstration of strong coupling via electro-optical tuning in high-qualityqd-micropillar systems. *Optics Express*, 16(19):15006–15012, 2008.

[78] I. Vurgaftman, J. R. Meyer, and L. R. Ram-Mohan. Band parameters for iii–v compound semiconductors and their alloys. *Journal of Applied Physics*, 89(11):5815–5875, 2001.

[79] B. Gayral and J. M. Gérard. Photoluminescence experiment on quantum dots embedded in a large purcell-factor microcavity. *Physical Review B*, 78(23):235306, 2008.

[80] D. Sanvitto, A. Daraei, A. Tahraoui, M. Hopkinson, P. W. Fry, D. M. Whittaker, and M. S. Skolnick. Observation of ultrahigh quality factor in a semiconductor microcavity. *Applied Physics Letters*, 86(19):191109, 2005.

[81] S. Ates, C. Gies, S. M. Ulrich, J. Wiersig, S. Reitzenstein, A. Loffler, A. Forchel, F. Jahnke, and P. Michler. Influence of the spontaneous optical emission factor beta on the first-order coherence of a semiconductor microcavity laser. *Physical Review B*, 78(15):155319, 2008.

[82] H. Nakamura, S. Nishikawa, S. Kohmoto, K. Kanamoto, and K. Asakawa. Optical nonlinear properties of inas quantum dots by means of transient absorption measurements. *Journal of Applied Physics*, 94(2):1184–1189, 2003.

[83] David Press, Stephan Götzinger, Stephan Reitzenstein, Carolin Hofmann, Andreas Löffler, Martin Kamp, Alfred Forchel, and Yoshihisa Yamamoto. Photon antibunching from a single quantum-dot-microcavity system in the strong coupling regime. *Physical Review Letters*, 98(11):117402, 2007.

[84] A. Laucht, F. Hofbauer, N. Hauke, J. Angele, S. Stobbe, M. Kaniber, G. Böhm, P. Lodahl, M. C. Amann, and J. J. Finley. Electrical control of spontaneous emission and strong coupling for a single quantum dot. *arXiv:0810.3010v2*, 2008.

[85] A. Naesby, T. Suhr, P. T. Kristensen, and J. Mørk. Influence of pure dephasing on emission spectra from single photon sources. *Physical Review A*, 78(4):045802, 2008.

[86] A. Auffèves, J.-M. Gérard, and J.-P. Poizat. Pure emitter dephasing : a ressource for advanced solid-state single photon sources. *arXiv:0808.0820v2*, 2008.

[87] D. C. Reynolds, K. K. Bajaj, C. W. Litton, G. Peters, P. W. Yu, and J. D. Parsons. Refractive index, n, and dispersion, -dn/d lambda, of GaAs at 2 K determined from Fabry–Perot cavity oscillations. *Journal of Applied Physics*, 61(1):342–345, 1987.

[88] Wen-Hao Chang, Wen-Yen Chen, Hsiang-Szu Chang, Tung-Po Hsieh, Jen-Inn Chyi, and Tzu-Min Hsu. Efficient single-photon sources based on low-density quantum dots in photonic-crystal nanocavities. *Physical Review Letters*, 96(11):117401, 2006.

[89] S. Varoutsis, S. Laurent, P. Kramper, A. Lemaître, I. Sagnes, I. Robert-Philip, and I. Abram. Restoration of photon indistinguishability in the emission of a semiconductor quantum dot. *Physical Review B*, 72(4):041303, Jul 2005.

[90] Serkan Ates, Sven Markus Ulrich, Stephan Reitzenstein, Andreas Löffler, Alfred Forchel, and Peter Michler. Indistinguishable photons from the resonance fluorescence of a single quantum dot in a microcavity. *arXiv:0902.3612v1*, Feb 2009.

[91] Thomas Legero, Tatjana Wilk, Markus Hennrich, Gerhard Rempe, and Axel Kuhn. Quantum beat of two single photons. *Physical Review Letters*, 93(7):070503, Aug 2004.

[92] YA Vlasov, M O'Boyle, HF Hamann, and SJ McNab. Active control of slow light on a chip with photonic crystal waveguides. *Nature*, 438:65–69, 2005.

[93] Steven G. Johnson and J. D. Joannopoulos. Block-iterative frequency-domain methods for maxwell's equations in a planewave basis. *Optics Express*, 8(3):173–190, 2001.

[94] M. Kaniber, A. Laucht, T. Hurlimann, M. Bichler, R. Meyer, M.-C. Amann, and J. J. Finley. Highly efficient single-photon emission from single quantum dots within a two-dimensional photonic band-gap. *Physical Review B*, 77(7):073312, 2008.

[95] E. Viasnoff-Schwoob, C. Weisbuch, H. Benisty, S. Olivier, R. Houdre, and C. J M Smith. Spontaneous emission enhancement at a photonic wire miniband edge. *Optics Letters*, 30(16):2113–2115, Aug 2005.

[96] A. F. Koenderink, M. Kafesaki, C. M. Soukoulis, and V. Sandoghdar. Spontaneous emission rates of dipoles in photonic crystal membranes. *Journal of the Optical Society of America B*, 23:1196–1206, 2006.

[97] J. M. Smith, P. A. Dalgarno, R. J. Warburton, A. O. Govorov, K. Karrai, B. D. Gerardot, and P. M. Petroff. Voltage control of the spin dynamics of an exciton in a semiconductor quantum dot. *Physical Review Letters*, 94(19):197402, 2005.

[98] Henri Nielsen et al. *Unpublished results.*